INFORMATION TO USERS

This manuscript has been reproduced from the microfilm master. UMI films the text directly from the original or copy submitted. Thus, some thesis and dissertation copies are in typewriter face, while others may be from any type of computer printer.

The quality of this reproduction is dependent upon the quality of the copy submitted. Broken or indistinct print, colored or poor quality illustrations and photographs, print bleedthrough, substandard margins, and improper alignment can adversely affect reproduction.

In the unlikely event that the author did not send UMI a complete manuscript and there are missing pages, these will be noted. Also, if unauthorized copyright material had to be removed, a note will indicate the deletion.

Oversize materials (e.g., maps, drawings, charts) are reproduced by sectioning the original, beginning at the upper left-hand corner and continuing from left to right in equal sections with small overlaps.

Photographs included in the original manuscript have been reproduced xerographically in this copy. Higher quality 6" x 9" black and white photographic prints are available for any photographs or illustrations appearing in this copy for an additional charge. Contact UMI directly to order.

ProQuest Information and Learning
300 North Zeeb Road, Ann Arbor, MI 48106-1346 USA
800-521-0600

UMI®

DISSERTATION

CLIMATIC IMPACT OF LOWLAND DEFORESTATION ON TROPICAL MONTANE CLOUD FORESTS IN COSTA RICA

Submitted by

Udaysankar S. Nair

Department of Atmospheric Science

In partial fulfillment of the requirements

for the degree of Doctor of Philosophy

Colorado State University

Fort Collins, Colorado

Spring 2002

COLORADO STATE UNIVERSITY

November 29, 2001

WE HEREBY RECOMMEND THAT THE DISSERTATION PREPARED UNDER OUR SUPERVISION BY UDAYSANKAR S. NAIR ENTITLED CLIMATIC IMPACT OF LOWLAND DEFORESTATION ON TROPICAL MONTANE CLOUD FORESTS IN COSTA RICA BE ACCEPTED AS FULFILLING IN PART REQUIREMENTS FOR THE DEGREE OF DOCTOR OF PHILOSOPHY.

Committee on Graduate Work

Committee Member

Committee Member

Committee Member

Co-Adviser

Co-Adviser

Department Head

ABSTRACT

CLIMATIC IMPACT OF LOWLAND DEFORESTATION ON TROPICAL MONTANE CLOUD FORESTS IN COSTA RICA

Tropical montane cloud forests depend on predictable, frequent, and prolonged immersion in clouds. Recent studies have shown that there has been a reduction in dry season moisture input from direct interception of cloud water and wind blown mist at the lee edge of the Monteverde cloud forest, Costa Rica, since the mid 1970s. This reduction of moisture could be responsible for the population crashes of anurans observed in the region. It has been hypothesized that this behavior is a result of increases in cloud base height, linked to increased sea surface temperatures. This study presents a complementary hypothesis, that deforestation upstream of the Monteverde cloud forest preserve is responsible for the observed changes in cloud base height.

An automated cumulus cloud classification scheme is used to extract monthly spatial maps of the frequency of occurrence of cumulus cloudiness over Costa Rica from GOES-8 visible channel satellite imagery. It is found that cumulus cloud formations in the morning hours over deforested regions are suppressed compared to forested areas. The degree of suppression appears to be associated with the extent of deforestation. This

difference in cloud formation between forested and deforested areas is a clear signal of land-use change influencing the regional climate.

The Regional Atmospheric Modeling System (RAMS) numerical modeling simulations are used to explore the differences in cloud field characteristics over the lowland pasture and forest surfaces. Statistically significant differences in cloud base height and cloud thickness are found between the forest and pasture simulations, clouds having higher base heights and being thinner over pasture surfaces compared to forest surfaces. There are enhanced sensible heat fluxes over pasture surfaces compared to forest surfaces, while forest surfaces have higher latent heat fluxes.

RAMS is also used to examine the impact of lowland deforestation on orographic cloud formation. Numerical modeling simulations of orographic cloud formation is examined for three types of deforestation scenarios, namely forested, completely deforested, and partially deforested where the most recent estimate of forest cover for the Costa Rican region is used. Numerical modeling suggests that deforestation shrinks the areal extent of the orographic cloud banks and elevates its base to higher altitudes. The increase in cloud base height is on the order of 200 m for complete deforestation and 100 m for partial deforestation. Increases in cloud base height of this magnitude may significantly impact the hydrology of the cloud forest regions. Deforestation results in a decrease of the orographic cloud cover, with the decrease being proportional to the amount of deforestation.

The results from this study suggest that land use in tropical lowlands has serious impacts on ecosystems in adjacent mountains. Deforestation in the Costa Rican lowlands

may have a detrimental effect of increased frequency of mist free days upstream at Monteverde cloud forest preserve.

Udaysankar S. Nair
Department of Atmospheric Science
Colorado State University
Fort Collins, Colorado 80523
Spring 2002

ACKNOWLEDGEMENTS

This study was partially supported by the National Aeronautics and Space Administration (NASA) Earth Observing System Clouds (EOS) and Earth's Radiant Energy System (CERES; NAS1-98131) and Advanced Spaceborne Thermal Emission and Reflection Radiometer (ASTER; NAS5-31718) projects. I would also like to acknowledge support from Roger A. Pielke Sr. under National Science Foundation (NSF) Grant Nos. DEB-9632852, DEB-9977066, ATM-9910857 and United States Geological Survey (USGS) Grant No. 99CRAG005 SA 9005CS0014. The Geostationary Operational Environmental Satellite 8 (GOES 8) data used in this research was acquired by the GOES 8 ground station at the Global Hydrology and Climate Center, Huntsville, AL.

I am thankful for the support, guidance, inspiration and encouragement provided by my co-advisors Ronald Welch and Roger Pielke Sr. I thank my committee members, David Randall, Thomas Vonder Haar, Thomas McKee, and Roger Culver for their helpful suggestions. I am thankful to Robert Lawton whom along with Ronald Welch introduced me to this research area. I thank Kevin Doty for his help with assimilation of National Center for Environmental Prediction (NCEP) reanalysis data into Regional Atmospheric Modeling System (RAMS) used in this study. I am thankful to Dallas Staley

for her help in preparing this dissertation and also for numerous other occasions she extended her help without any reservation.

I am thankful to my wife for her support, patience, and constant encouragement, without which this endeavor would have been extremely difficult. I am thankful to my parents who nourished my interest in science and encouraged me to pursue graduate studies. I am thankful to my in-laws for their encouragement and support.

TABLE OF CONTENTS

LIST OF TABLES

LIST OF FIGURES

Chapter 1

Introduction

Tropical montane cloud forests (TMFC) are biologically rich and diverse as well as one of the most threatened ecosystems in the world (Hamilton et al., 1993). TMCFs are ecosystems characterized by predictable, frequent and prolonged immersion in orographic clouds. TMCFs occupy approximately 0.3% of Earth's surface (Long, 1994), and are typically found between altitudes ranging from 1500 – 3500 m (Bruijnzeel and Proctor, 1993). However in coastal regions TMCFs are found at lower altitudes. The tropical montane cloud forests are ecologically very valuable due to the high biodiversity found within these ecosystems, and the percentage of endemics within TMFCs is high (Hamilton et al., 1993; Doumenge et al., 1993). For example 32% of the Peruvian endemics are found in TMFC (Hamilton et al., 1993). While the cloud forests provide habitats for some of the endangered species in the world, many of the TMFCs are situated in regions (Myers et al., 2000) where large stocks of diverse endemic species are rapidly losing their habitats. These biodiversity hotspots occupying approximately 0.4% of Earth's land-surface support but about 20% and 16% of Earth's plants and vertebrates respectively. Of primary concern is that most of these hotspots retain less than 25% of their original primary vegetation covers (Myers et al., 2000).

1.1 Hydrological Importance of Tropical Montane Cloud Forests

In addition to the ecologically important function of supporting biodiversity, cloud forests also play important roles in the local hydrology, by providing additional input of water to the hydrologic cycle from direct interception of cloud water by the vegetation (Hamilton et al., 1993). The vegetation in tropical montane cloud forests collects a significant amount of moisture by direct interception of liquid water from orographic clouds, advected clouds and wind blown mist. The process of direct moisture interception by vegetation is usually termed as horizontal precipitation in the literature. Horizontal precipitation can account for a significant portion of the total precipitation in cloud forests. Data collected from various cloud forest locations around the world show that horizontal precipitation can account for up to 14 – 18% and 15% - 100% of total precipitation during wet and dry season, respectively (Bruijnzeel and Proctor, 1993). Cloud forests play important role in the local hydrology through enhanced moisture input from horizontal precipitation. Therefore, destruction of cloud forests could result in decreased stream flows and ground water fluxes (Meher-Homji, 1991). For example, stream flow measurements from areas in Sri Lanka, where cloud forests have been converted to tea estates, show decreases in stream flow without accompanied decline in precipitation (Doumenge et al., 1993). Also epiphytes such as moss and ferns within the cloud forests act like sponges soaking up precipitation during rainy season and slowly releasing it during the dry season (Still et al., 1999). This process provides a measure of protection against flooding and soil erosion.

1.2 The Monteverde Cloud Forest Preserve

The Monteverde cloud forest preserve in Costa Rica has been a subject of extensive research in the recent years. The Monteverde forest preserve is located on the crest of continental divide in the northwest region of Costa Rica. The forest preserve, which is about 150 km from the Caribbean coast, extends down to elevations of 700 m on both Caribbean and Pacific slopes. The cloud forests in Monteverde occur at elevations of approximately 1300 – 1400 m on the Caribbean slope and slightly higher elevations of 1500 – 1850 m on the drier Pacific slopes. The Monteverde forest preserve hosts a very diverse population of flora and fauna. More than 100 species of mammals, 400 species of birds, and 2500 species of plants are found in the Monteverde forest preserve.

Similar to other cloud forests, horizontal precipitation accounts for a significant amount of the total precipitation in Monteverde region. On average, horizontal precipitation contributes about 22% of the total annual precipitation. The percentage contribution from the horizontal precipitation is significantly higher during the dry season, which extends from February through April. During the dry season, input of moisture from the horizontal precipitation process is critical, since the ecosystem is under higher stress compared to the wet season.

In the Cordillera, anuran population crashes, an increase in the upper elevation of bird ranges on the Pacific slope, and longer mist-free intervals in the dry season at the lee edge of the Monteverde cloud forest have been attributed to an increase in the base height of the orographic cloud bank (Pounds et al., 1999). The frequency of long (>=5 day) mist-free periods in the dry season is related to Pacific sea surface temperatures, and thus El Niño events, but a trend remains after these are considered (Pounds et al., 1999).

From a global climate model under 2 x CO_2 conditions Still et al. (1999) suggest that sea surface warming results in intensification of tropical hydrological cycling, with release of latent heat upon condensation warming the atmosphere. From this Still et al. (1999) and Pounds et al. (1999) infer an increase in the lifting condensation level and the height of orographic cloud banks. Global climate models, however, have coarse spatial resolution (~400 km horizontally, and several hundred meters vertically in that of Still et al. 1999), and are incapable of resolving subgrid-scale features such as clouds, or terrain and land-use features known to have important influences on cloud formation. Still et al. (1999) suggested using mesoscale regional models that better resolve the topography and local land-use changes to further explore impact of climate change on TMCFs.

1.3 Influence of Land Use on Regional Climate

It has been long recognized that through modulation of surface energy budgets, land use can have significant influence on the regional climate. It has been observed that land-use changes are usually accompanied by variations in surface properties such as albedo, temperature, roughness length, and soil moisture distribution. Satellite observations show albedo differences of up to 0.2 resulting from overgrazing in the Sinai-Negev region (Otterman, 1981). Sagan et al. (1979) reviewed the probable albedo differences caused by land-use changes originating from human activities. They reported albedo differences ranging from 0.02 for land-use change from pasture to city, to extreme values of 0.4 for land-use change from pasture to slat flats. Differences in land use can cause surface temperature differences ranging from a couple of degrees to up to 10 degrees (Otterman, 1974; Segal et al., 1988). Land-use change also can alter the surface roughness significantly. For example the roughness length for a forest is about 2.3 m compared to

0.05 m for pasture (Gash and Nobre, 1997). Finally, deforestation can reduce the water storage capacity of the surface soil (Anthes, 1984; Meher-Homji, 1991; Shukla et al., 1990).

The variations in surface properties also can cause changes boundary layer air temperature and moisture, the depth of boundary layer, local rainfall and cloudiness. Removal of vegetation usually results in an increase of surface air temperature (Bryant et al., 1990; Schwartz and Karl, 1990; Bastable et al., 1993) unless the albedo of underlying surface is significantly higher. The higher air temperature over denuded and drier surfaces is due to the enhancement of sensible heat fluxes over such areas. For example, along the United States – Mexican border, surface air temperatures were observed to be 4^0C higher on the overgrazed Mexican side (Bryant et al., 1990). The boundary layer air is moister over forested areas compared to deforested areas. An average difference in specific humidity deficit of 1 g kg^{-1} was observed for forested versus deforested areas in Amazon (Bastable et al., 1993). However in arid or semiarid regions, the boundary layer moisture content is enhanced over irrigated cropland regions (Segal et al., 1989).

Observations show differences in the heights of the convective boundary layers, depending on the nature of land use in the underlying area (Gash and Nobre, 1997; Lyons et al., 1993). In the Amazonian region, the boundary layer depth was observed to be higher by 700-1000 m over deforested areas compared to forested areas (Gash and Nobre, 1997). In semiarid southwestern Australia, replacement of the native vegetation by agriculture resulted in lowering of boundary layer depth (Lyons et al., 1993). Christopher Columbus made the observation of diminished mist and rain in the Canary, Madeira and Azore Islands since the removal of forests (Shukla and Mintz, 1982). Studies show that

deforestation leads to a decrease in rainfall (Brooks, 1928; Meher-Homji, 1991; Otterman, 1990; Sud et al., 1993; Pielke et al., 1998), although irrigation of croplands in semi arid and arid regions can augment precipitation. Indeed, Schickendanz (1976) reports significant augmentation of summer rainfall in Kansas, Nebraska, and Texas, resulting from irrigation of croplands.

The nature of land use and surface heterogeneity can have a significant influence on the formation and development of the convective clouds. Pielke (2001) provides a detailed review of influence of vegetation and soil properties on cumulus cloudiness and rainfall. The majority of the modeling and theoretical studies show that differential heating over contrasting surface types results in generation of mesoscale circulations that enhance cloudiness (Anthes, 1984; Ookouchi et al., 1984; Segal et al., 1988; Chen and Avissar, 1994; Avissar and Liu, 1996; Emori, 1998; Avissar and Schmidt 1998). Differing vegetation over adjacent surfaces also can induce sea breeze like circulations (Segal et al., 1988). Avissar and Liu (1996) note that updrafts produced by surface heterogeneity are usually stronger than those resulting from turbulence. Over regions where convective rainfall creates a heterogeneous soil moisture distribution, Emori (1998) found that convergence of air over drier soil initiates convective clouds. The rain from these convective clouds makes the soil wet compared to the surroundings thereby maintaining the heterogeneity of the soil moisture distribution.

Suppression of cumulus cloudiness over water bodies has been observed since the early days of satellite imagery. Segal et al. (1997) showed suppression of cumulus downwind of lakes. Using satellite imagery over the Oklahoma region, Rabin et al. (1990) showed that cumulus clouds formed earlier over areas with large sensible heat

fluxes such as harvested wheat fields. Such preferential formation of cumulus clouds was also observed over deforested regions in Amazonia (Cutrim et al., 1995) and areas of relatively sparse vegetation cover in central United States (Rabin and Martin, 1996). In southwestern Australia, there is higher incidence of cumulus cloudiness over regions with native vegetation cover compared to adjacent areas covered by agricultural species (Lyons et al., 1993). The sensible heat fluxes over regions covered by native vegetation are higher compared to croplands. However, increased soil moisture caused by irrigation, can enhance the convective available potential energy (CAPE), thereby increasing the probability of convection (Pielke and Zeng, 1989). The influence of land surface on cumulus cloud formation also is dependent on the stability of the overlying atmosphere. Under stable atmospheric conditions clouds may develop earlier over moist surfaces, while for weakly stable conditions clouds form earlier over drier surfaces (Wetzel et al., 1996).

1.4 Deforestation of Costa Rican Lowlands

Trade winds flow from the Caribbean 100 km across lowlands of the Rio San Juan basin to the Monteverde TCMF. Moving at 3-5 m sec^{-1}, the lower atmosphere has 5 - 10 hours during which it can be influenced by the land below. The original tropical forests in the Costa Rican lowlands are being rapidly replaced by pastures and agricultural landscapes. By 1940 a 600 km^2 area at the Caribbean foot of the Cordillera de Tilarán had been cleared (Vaughan, 1983). Agricultural colonization has since then spread and by 1992 only about 1200 km^2 (18% of the area) of intact natural vegetation remain in the Costa Rican part of the Rio San Juan basin lowlands (Sader and Joyce, 1988). Since deforestation in the Caribbean lowlands can modify the nature of the air masses

responsible for cloud formation, land-use changes cannot be ruled out as a causative factor for the observed climate change in the Monteverde region.

1.5 Outline of This Study

In this dissertation the effect of Costa Rican lowland deforestation on cumulus and orographic cloud formation is explored using numerical cloud model and satellite data. The development of the satellite cloud detection scheme used in this study is described in Chapter 2. The satellite observations of cloudiness in the Costa Rican region are examined in Chapter 3. The sensitivity of cumulus cloudiness to deforestation is also examined in Chapter 3. The impact of Costa Rican lowland deforestation to orographic cloud formation in Costa Rican region is reported in Chapter 4. The findings of the study and recommendations for future work are presented in Chapter 5.

Chapter 2

Detection of Boundary Layer Cumulus Cloud Fields in GOES Satellite Imagery

2.1 Introduction

Since shallow convection is strongly influenced by surface characteristics, areas of significant land-use change are expected to show indications of local climate modification (Nair et al., 2000). The nature of the underlying surface and the vegetation type influence the radiation budget and the heat and moisture fluxes into the atmosphere. Thus the nature of boundary layer cumulus cloudiness can be expected to vary depending on the nature of vegetation cover.

The suppression of cumulus cloudiness over inland water bodies has been observed from the early days of operational use of meteorological satellites. Using satellite imagery, Rabin et al. (1990) showed preferential formation of cumulus clouds over harvested wheat fields. Cutrim et al. (1995) compared differences in cumulus cloudiness between forested and deforested areas over Amazonia. They found enhanced cumulus cloudiness over deforested areas. Another study of cumulus cloudiness over the central United Sates by Rabin and Martin (1996) also showed similar results. They observed shallow cumulus clouds more frequently over sparsely vegetated compared to densely vegetated surface. Some of the results from the 2D model simulations from the study conducted by Chen and Avissar (1994) agree with these observations. They found enhanced shallow cumulus cloudiness over dry surface compared to wet surface. However there are other studies that indicate the effects of vegetation on cumulus cloudiness contrary to that suggested by the above mentioned studies. For example Pielke

and Zeng (1989) used sounding data to demonstrate the larger energy for cumulus convection over wetter surfaces. Nair et al. (2000) examined the sensitivity of Convective Available Potential Energy (CAPE) climatology to perturbations in surface temperature and dewpoint. They showed that small dewpoint perturbations cause large variations in the value of CAPE. The CAPE is significantly less sensitive to variations in surface temperature. Increased moisture flux over densely vegetated surfaces may spur the development of cumulus cloudiness compared to increased sensible heat flux over a sparsely vegetated surface. Observations of cumulus cloud fields over areas of varied land use are thus expected to show signals of local climate modification resulting from differences in surface properties.

Satellite data are ideal to further our understanding of the issues related to boundary layer cumulus cloud field characteristics and its relationship to land use. In particular Landsat, ASTER and IKONOS imagery can be used to resolve high resolution features, and geostationary data is required to study the temporal variations. Note that the analysis of large volumes of data is necessary, which requires the use of automated methods for identifying cumulus cloud fields in satellite imagery.

Most current existing cloud masks either do not detect specific cloud types or have problems identifying small cumulus especially at higher spatial resolution data. There are currently two main operational global cloud classification schemes, the International Satellite Cloud Climatology Project (ISCCP) and the National Oceanic and Atmospheric Administration (NOAA) Cloud and Advanced Very High Resolution Radiometer (AVHRR) algorithm (CLAVR). These algorithms do not identify cloud fields as entities,

the areal extent of the cloud fields, or the individual clouds that are members of a particular cloud field.

This chapter presents several new techniques for detection of boundary layer cumulus cloud fields in satellite imagery. In the present study, cloud field detection techniques are developed for Geostationary Operational Environmental Satellite 8 (GOES-8) data. Different methods are intercompared for accuracy and also for computation efficiency. Section 2.2 describes the data used in this study, and Section 2.3.2 describes the methodology. Section 2.4 discusses the results, and Section 2.5 concludes.

2.2 Data

The data used in this study are from GOES-8, which has one visible (0.52 – 0.72 μm) and four infrared channels (3.78 – 4.03 μm, 6.47 – 7.02 μm, 10.2 – 11.2 μm, 11.5 – 12.5 μm). Spatial resolution at the ground for channel 1 is 1 km, channel 2, 4 and 5 have a ground resolution of 4 km, while channel 3 has a ground resolution of 8 km. Channel 1 (visible channel) data is used in this study. Channel 1 data are calibrated and normalized by the cosine of solar zenith angle to yield reflectance values. A total of forty-two scenes, each of size 512 x 512 pixels, are used in this study. The location, date and time of acquisition of the forty-two scenes are given in Table 2.1. The first twelve are used for training the different techniques used in this study, and the other thirty independent scenes are then used to evaluate the accuracy of the various techniques. Twelve representative scenes are shown in Figure 2.1. Notice that the scenes include a wide variety of cumulus cloudiness, including cloud streets, free convection, and cloud fields over both land and ocean. Also note that, as shown in Table 2.1, scenes are chosen to be

Scene	Date	Time (UTC)	Coordinates	Location
1	1 August 1998	1630	34.49N,77.88W	Virginia
2	1 October 1998	2030	47.48N,87.45W	Canada
3	22 December 1998	1931	26.94N, 81.19W	Florida
4	25 March 1999	1615	20.36N, 87.81W	Yucatan
5	9 May 1999	1530	21.78N, 78.97W	Cuba
6	5 July 1998	1630	49.84N, 83.71W	Canada
7	15 October 1430	1430	27.05N, 88.68W	Gulf of Mexico
8	3 June 1999	2000	29.60N, 97.85W	Texas
9	26 January 1999	1815	17.63N, 92.89W	Mexico
10	10 November 1999	1545	14.08N, 83.94W	Nicaragua
11	18 April 1999	2131	30.64N, 75.08W	Atlantic
12	13 October 1999	1701	29.25N, 82.18W	Florida
13	22 April 1999	1815	13.04N, 85.42W	Nicaragua
14	2 July 1998	1930	29.01N, 97.56W	Texas
15	9 July 1998	1930	45.26N, 84.93W	Michigan
16	28 June 1998	1531	30.01N, 97.47W	Texas
17	12 April 1998	1631	31.51N, 76.76W	Atlantic
18	7 April 1998	1601	27.09N, 81.16W	Florida
19	19 August 1998	1730	31.75N, 88.99W	Mississippi
20	31 August 31 1998	1731	43.95N, 87.47W	Lake Michigan
21	23 September 1999	2031	24.40N, 103.47W	Mexico
22	10 November 2000	2031	26.01N, 92.65W	Gulf of Mexico
23	20 November 2000	2031	26.79N, 87.75W	Gulf of Mexico
24	4 February 2000	1615	9.81N, 65.74W	Venezuela
25	12 February 2000	1615	21.34N, 88.24W	Yucatan
26	16 February 2000	1615	21.14N, 76.53W	Cuba
27	2 April 1999	1815	18.59N, 89.18W	Yucatan
28	16 April 1999	1815	21.2N, 80.92W	Cuba
29	5 July 1998	1930	42.30N, 84.51W	Michigan
30	16 July 1998	1931	37.04N, 98.32W	Kansas
31	17 July 1998	1930	51.06N, 90.23W	Canada
32	7 June 1998	1531	20.10N, -89.18W	Yucatan
33	11 April 1998	1601	23.07N, 83.21W	Cuba
34	28 April 1998	1601	16.44N, 84.70W	Honduras
35	1 August 1998	1730	41.38N, 85.02W	Michigan
36	1 August 1998	1731	39.51N, 88.33W	Illinois
37	23 August 1998	1731	36.13N, 85.55W	Tennessee
38	6 January 2001	1701	33.13N, 76.34W	Atlantic
39	7 January 2001	1701	28.48N, 76.05W	Atlantic
40	1 March 2000	2131	19.97N, 90.01W	Yucatan
41	19 March 2000	2131	19.66N, 89.35W	Yucatan
42	1 November 2000	2031	22.52N, 80.08W	Cuba

Table 2.1: Description of the GOES scenes used in the study.

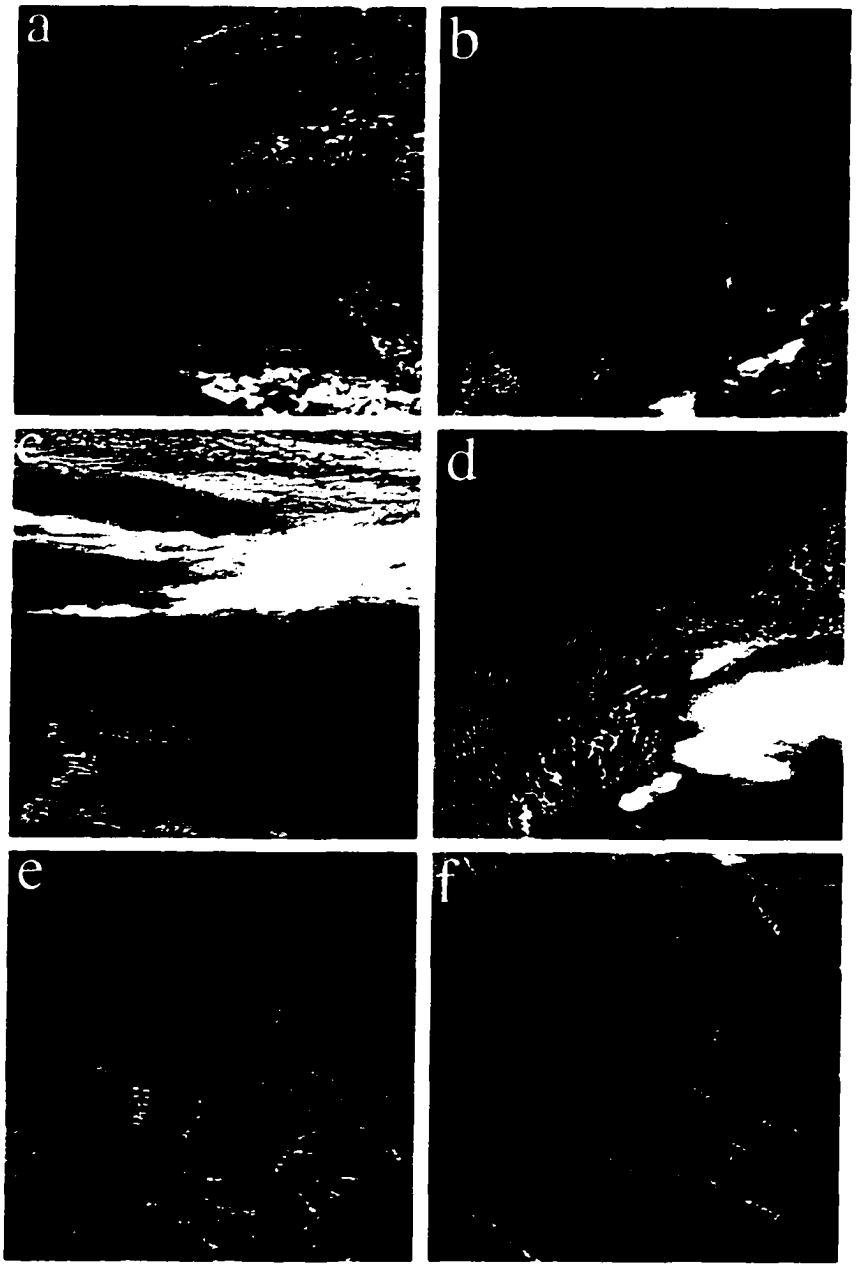

Figure 2.1: The visible channel imagery of the six representative 512 x 512 km GOES scenes used in this study.

representative for convection at different times of the day and season and also varied geographic locations.

2.3 Methodology

Boundary layer cumulus clouds have low contrast in both visible and infrared channels. This low contrast makes the automatic detection of cumulus clouds in satellite imagery very difficult. For GOES-8 satellite data this problem becomes even more severe, since the infrared channel resolution is 4 km, compared to 1 km in visible channel. Small boundary layer cumulus clouds are sub-resolution in the infrared channels. In addition cumulus cloud top temperatures generally have poor contrast with the surface. Thus, cloud detection algorithms relying on spectral information alone have difficulty in detecting small cumulus clouds in GOES satellite imagery. Therefore, alternative methods for the detection of cumulus cloud fields are explored in this investigation.

This study intercompares several types of methods for detecting cumulus cloud fields in GOES satellite imagery. The approach consists of the Structural Thresholding Algorithm, which is based on the analysis of the overall structure of the cumulus cloud fields. This technique crudely mimics the logic used by a human analyst to identify cumulus cloud fields in satellite imagery. Other approaches use the Maximum Likelihood classifier based on various textural and edge detection features for identifying cumulus cloud fields. A data mining system (Hinke et al., 2001) developed by the Information Technology and System Center at University of Alabama in Huntsville was used to implement the Maximum Likelihood classifiers based on texture and edge detection features. Note that the Structural Thresholding algorithm identifies both the cumulus cloud fields and also the individual clouds within the fields. The texture and edge

detection feature based Maximum Likelihood classifiers, however, detect only the areal extent of cumulus cloud fields.

2.3.1 Structural Thresholding Method

The spatial structure of cumulus cloud fields is characterized by grouping small clouds into regions. Then the cloud number density, or number of clouds per unit area, is used for discriminating cumulus cloud fields. However, typical values associated with cumulus cloud fields first must be known before cloud number density can be used as a discriminant. A sensitivity analysis of the classification as a function of cloud number density determines this threshold value.

The Structural Thresholding algorithm involves three steps: 1) enhance the contrast between clouds and background by subtraction of the background albedo, 2) create a cloud mask using a region-growing algorithm for localized thresholding of clouds, and 3) segment the cloud mask to calculate the cloud number density at each pixel location and flag the pixel as cloud field if the calculated value is greater than the threshold. These steps are detailed as follows.

2.3.1.1 Contrast Enhancement

Clouds are relatively easy to detect over uniform dark surfaces such as the ocean. However, the contrast between the clouds and background is diminished over heterogeneous regions of higher albedo, making the cloud detection problematic. One solution is to enhance the contrast between clouds and background over such areas by subtraction of the cloud free background albedo. The background albedo can be derived from a time series of visible imagery over the same geographic location and same time of day. The basic assumption is that clouds and optically thick aerosols are brighter than the

background. The minimum albedo value is chosen as the background albedo for each pixel. The background albedo for each pixel then is subtracted from the visible image albedo of the scene being analyzed to yield the contrast enhanced visible channel data.

Figure 2.2a shows a 250 x 250 km subregion of Figure 2.1a, taken on 22 April 1999 and Figure 2.2b shows the derived background albedo determined from a series of ten scenes all taken at 1815 UTC from 18 to 27 April 1999. Finally Figure 2.2c shows the resulting image with the background largely removed. Notice the substantial increase in contrast between the clouds and the background in Figure 2.2c compared to Figure 2.2a.

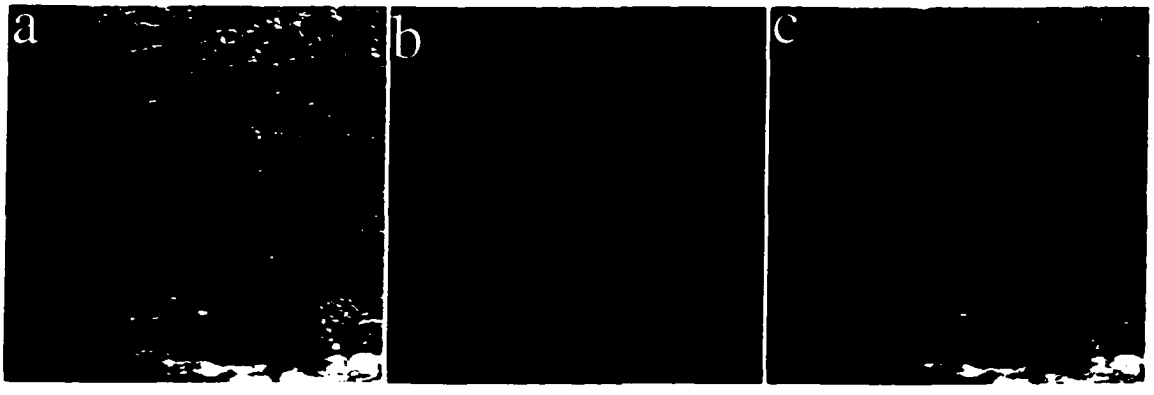

Figure 2.2 a) 250 x 250 km subregion of scene shown in Figure 1a; b) background albedo for the region derived from a time series of 10 scenes; c) contrast enhanced image of the subregion.

2.3.1.2 The All-Cloud Mask

Clouds are further separated from the background by applying a region growing algorithm as a localized thresholding mechanism to the contrast-enhanced visible channel data. The basic assumption used is that the means of the pixels associated with clouds are significantly different than those of pixels associated with the background or surface. Given groups of statistically similar pixels and their associated mean contrast enhanced

albedo values, a threshold value can be defined to differentiate between pixels associated with clouds from those associated with the background.

In the present study the Levine and Shaheen (1978) region growing algorithm is used as an unsupervised classifier, identifying statistically similar groups of pixels. This approach has been applied by Chou et al. (1994) to identify different scenes in Landsat Thematic Mapper polar scenes. The region growing algorithm identifies statistically distinct clusters of pixels within the contrast-enhanced visible channel data and assigns the pixels membership to groups or regions. Membership is decided depending on how the addition of a pixel to a particular group alters its mean and standard deviation. The general procedure used can be described as follows. From q spectral channels (in the present study $q = 1$) it is desired to grow regions or groups by merging as many adjacent pixels as possible, based on a specified threshold. A region or group G is defined as a collection of n pixels that are statistically similar. If there are k groups, with each group G_k constituted of n_k pixels with mean $\mu_k(q)$ and standard deviation $\sigma_k(q)$, then

$$\mu_k(q)=\frac{1}{n_k}\sum X_q(i,j) \quad i,j \in G_k \tag{2.1}$$

$$\sigma_k(q) = \left[\frac{1}{n_k-1}\sum (X_q(i,j)-\mu_k(q))\right]^{\frac{1}{2}} \quad i,j \in G_k \tag{2.2}$$

where $X_q(i,j)$ is the contrast enhanced brightness value at pixel location (i,j) for spectral channel q. Initially the pixels do not belong to any group. Starting at the upper left corner location, the q spectral channel values for the first pixel location are used as the seed for first group. The initial mean and standard deviation for the first group is set to be:

$$\mu_1(q) = X_q(0,0) \tag{2.3}$$

$$\sigma_1(q) = 0 \tag{2.4}$$

Adjacent pixels then are examined. For each following pixel (i^*,j^*), its membership to a group is determined using the following procedure:

a) The updated mean $\mu_k^*(q)$, and standard deviation $\sigma_k^*(q)$ for every group G_k is calculated as if pixel (i^*,j^*) were merged to that group using the following expressions:

$$\mu_k^*(q) = \frac{1}{n_k+1}\left[X_q(i^*,j^*)+n_k\mu_k(q)\right] \tag{2.5}$$

$$\sigma_k^*(q) = \frac{1}{n_k-1}\left[n_k\sigma_k^2 + \frac{n_k}{n_k+1}(X_q(i^*,j^*)-\mu_k(q))^2\right]^{\frac{1}{2}} \tag{2.6}$$

b) Determine the adaptive threshold $\theta_k(q)$ for every possible merging using the expression:

$$\theta_k(q) = \left[1 - \frac{\sigma_k^*(q)}{\mu_k^*(q)}\right]\theta, \tag{2.7}$$

where θ is the absolute threshold, a constant selected by the user. Smaller values of θ result in more groups, while larger values of θ make merging more probable, thus causing the formation of fewer groups.

c) For each group G_k, calculate the absolute difference between the spectral channel value at pixel location (i^*,j^*) and the mean for the group $\Delta\mu_k(q)$, for all the spectral channels, where

$$\Delta\mu_k(q) = \left|X_q(i^*,j^*) - \mu_k(q)\right| \tag{2.8}$$

If the absolute difference $\Delta\mu_k(q)$ is less than or equal to the adaptive threshold $\theta_k(q)$ for each spectral channel, then pixel $X_q(i^*,j^*)$ is merged with group G_k. If there is more than one possible merging, the pixel is merged with the group for which $\Sigma[\Delta\mu_k(q)]^2$ is a minimum.

d) If none of the groups meet the criterion of absolute difference $\Delta\mu_k(q)$ being less than or equal to adaptive threshold $\theta_k(q)$, then a new group is started with pixel $X_q(i^*,j^*)$ being the seed for the new group.

e) Steps (a) – (d) are repeated until all the pixels in the image are members of some group.

The contrast enhanced visible channel image is divided into subregions, and the region growing technique is applied to each of the subregions. The reason for applying the region growing procedure to subregions is that the spread or standard deviation of the groups increases as the total number of pixel increases. If the total number of pixels is high, some of the background pixels may be incorrectly added to groups associated with cloud pixels. In the present study the value of absolute threshold θ is set such that the region growing procedure identifies approximately seven groups (water, two land-surface types, four cloud types). For albedo values scaled from 0 to 255, the value needed to identify about seven groups is $\theta = 30$. Once the various groups within a subregion are identified, the mean albedo value for each group is examined to determine if the pixels belonging to that group are background or cloud. A threshold of cluster mean gray level, A_t, is used to distinguish cloud groups from background groups. The pixels belonging to groups with mean gray level value greater than A_t are identified as clouds and the others

as background. The value of A_t is determined from analysis of the sensitivity of the cloud mask to A_t. The details of this procedure are discussed in Section 2.4.

2.3.1.3 Detection of Cumulus Cloud Fields

For the detection of cumulus cloud fields, cloud number density (number of clouds per unit area) is used as a discriminant. This involves segmentation of the cloud mask derived from the procedure described in the previous section. The segmentation procedure distinguishes between the background and clouds, and it labels clouds as unique entities. The segmentation technique of Kuo et al. (1993) is used in this study. In this technique the cloud mask is scanned line by line and, once a cloudy pixel is encountered (seed pixel), the pixel is marked by assignment of a unique number to it. The eight neighboring pixels of the marked pixel are then examined. Any of the neighboring cloudy and unmarked pixels are assigned the same number given to the seed pixel. The neighbors of each of the newly marked pixels are then examined and the procedure is repeated until no more unmarked cloudy pixels are found. The zero, first and second moments of pixel coordinates that are being marked are also kept from which the coordinates of cloud centroids are determined.

To determine if a pixel is a part of a cloud field, a square region measuring L km on a side and centered on the pixel is examined. The number of clouds within a specified region is determined by identifying those clouds whose centeroids lie within that region. If the number of clouds within the region N_r is greater than or equal a specified number threshold N_t, then the pixel is labeled as being a part of the cloud field.

Using the above-described procedure, a cumulus cloud field mask is created. The cumulus cloud field mask at this point may have a number of small regions mislabeled as

cloud fields. These regions tend be along the perimeter of large cloud systems, where there is broken cloudiness. However, cumulus cloud fields in general tend to have large areal extent, and this property can be used to eliminate these smaller mislabeled regions. The cumulus cloud field mask is segmented, and the extents of individual cloud fields within the scene are determined. Cloud fields composed of less than 1000 pixels (1000 km^2, square region approximately 32 km on a side) are eliminated as being too small to be considered as viable cumulus cloud fields. This size threshold was arrived at after examining a number of cumulus cloud fields.

2.3.1.4 Selection of Number Threshold

The cloud size distribution associated with cumulus cloud fields $n(d)$, is the number of clouds of effective diameter d per unit area per unit diameter. The cloud size distribution generally is found to be best represented by a power law of the form (Wielicki and Welch, 1986, Kuo et al., 1993)

$$n(d) = n_0 d^{-\alpha} \tag{2.9}$$

where n_0 and α are constants. By integrating the above expression between the upper and lower limits of d, the number of clouds expected within a square region of L km on a side is given by:

$$N(L) = \sigma L^2 \tag{2.10}$$

where $\sigma = f(\alpha, n_0)$. Ideally the value of N_t is given by expression (2.10). However in reality the value of N_t is less than that given by equation (2.10). This is because large clouds reduce the probability of other clouds occupying the region. Also the value of N_t given by (2.10) is not applicable for regions along the edges of cloud field, as the region might lie partially outside the cloud field. However, the functional relationship between L

and N_t that is applicable for the purposes of cumulus cloud field identification is expected to be similar to (2.10) with an added correction factor involving L.

The selection of values of L and N_t is determined by analyzing how the classification accuracy varies for differing values of L and N_t. Twelve scenes chosen from different locations and for varying seasons and times of day are used for this purpose. For the twelve selected scenes, the cumulus cloud field mask is created using the Structural Thresholding algorithm for varying values of L and N_t. These cloud field masks are then compared against cloud field masks labeled by three experts, to determine the percentage of agreement between the algorithm and human analysts. Only the pixels labeled by all the three analysts as cloud fields are used in the comparison. Analyzing the percentage of agreement as a function L and N_t, the lower limit for L and also the relationship between L and N_t is determined. For each value of L, the value of N_t for which the mean percentage of agreement is the highest is determined. A second degree polynomial that best describes the relationship between pairs of L and N_t values that yield the highest classification accuracy is determined. After identifying the appropriate values of parameters associated with Structural Thresholding algorithm, the technique is applied to thirty independent scenes, and the average classification accuracy is determined. The details are discussed in Section 2.4.

The computational time for the Structural Thresholding algorithm is $O(L)$, but it is weakly dependent on the value of N_t. The optimal value of L that provides good accuracy of detection with least computation time is determined.

2.3.2 Maximum Likelihood Classifier

The Maximum Likelihood classifier (Duda and Hart, 1973) uses statistics derived from sample feature vectors of known classes (cumulus, stratus, land etc.) to determine the membership of an unknown class. Features are properties or patterns associated with classes that are be used to distinguish between the classes. Often these features are spectral properties such as albedo or infrared brightness temperatures. Thus for GOES-8 data, five channel values at a given pixel location may constitute a feature vector. However, spectral values alone often do not provide the maximum classification accuracy. Features may also be patterns of gray level variation in the locality of a pixel location. For example the GOES-8 visible channel gray level variations over land are much higher than that over ocean. Textures features are very commonly used to capture such gray level variations.

The Maximum Likelihood classifiers use probability density functions to determine class membership. The density functions are used to derive estimates for the a posteriori probabilities $P(\omega_i|\boldsymbol{x})$, the probability that a vector $\boldsymbol{x}$ belongs to class ω_i. Vectors are classified using this information by assigning them to the class which has the largest value of $P(\omega_i|\boldsymbol{x})$. Thus x is assigned to class ω_i if

$$P(\omega_i|\boldsymbol{x}) > P(\omega_j|\boldsymbol{x}) \quad \text{for all } j \neq i \tag{2.11}$$

The a posteriori probability $P(\omega_i|\boldsymbol{x})$ is given by Bayes' rule:

$$P(\omega_i|\boldsymbol{x}) = \frac{P(\boldsymbol{x}|\omega_i)\cdot P(\omega_i)}{P(\boldsymbol{x})}, \qquad P(x) = \sum_{1}^{m} P(\boldsymbol{x}|\omega_i)\cdot P(\omega_i) \tag{2.12}$$

Where $P(\boldsymbol{x}|\omega_i)$ is the probability that a vector associated with pixel from class ω_i has same values as vector $\boldsymbol{x}$, $P(\omega_i)$ is the aprior probability or relative occurrence of each

class, and $P(x)$ is the probability of occurrence of x. The conditional probability density function $P(x|\omega_i)$ is modeled as a Gaussian distribution. The parameters related to the Gaussian distribution can be estimated from sample feature vectors associated with each class. The process of estimating the distribution parameters is usually termed training of the classifier. The functional form of $P(x|\omega_i)$ is given by

$$P(x|\omega_i) = \frac{1}{(2\pi)^{\frac{d}{2}}|\Sigma|^{\frac{1}{2}}} \cdot e^{-\frac{1}{2}(x-\mu_i)^T \Sigma_i^{-1}(x-\mu_i)} \tag{2.13}$$

Where μ_i and Σ_i are calculated from sample feature vectors for each class. For each class i with $n_s(i)$ samples of feature vectors, the values of μ_i and Σ_i are:

$$\mu_i = \frac{1}{n_s(i)} \sum_{1}^{n_s(i)} x_i \tag{2.14}$$

$$\Sigma_i = \frac{1}{n_s(i)} \sum_{1}^{n_s(i)} (x_i - \mu_i)^T (x_i - \mu_i) \tag{2.15}$$

In this study the a priori probability $P(\omega_i)$ is assumed to be equal for all classes. A feature vector x of unknown membership is assigned to class ω_i if:

$$x \in \omega_i, \text{ if } P(x|\omega_i) > P(x|\omega_j) \quad \text{for all } j \neq i \tag{2.16}$$

2.3.3 Classifier Features

Since the spatial resolution of the infrared channels is too large to resolve small cumulus, textural features and features based on edge detection filters are used in this study. The classification accuracy for classifiers based on texture features, and edge detection features are examined.

2.3.3.1 Texture Features

Texture often is interpreted in the literature as a set of statistical measures of spatial distribution of gray level in an image. One aggregates the data to find suitable features of a region of the image and then uses those features as a basis for classification. In the alternative approach, texture is described by means of set of "primitives" and "production rules" analogous to symbols and associated rules of grammar in a formal language.

In this study, texture features are derived from two different types of approaches: 1) Gray Level Run Length (GLRL); and 2) Association Rules (AR). Note that there are a large number of textural measures that have been reported in the literature, many of which may be more effective than the ones utilized here. No attempt was made to find the "best" textural measures or to intercompare the vast number of possibilities. Rather, the intent here simply is to examine two simple approaches. The texture features computed using these two approaches then are used to develop classifiers for detecting cumulus cloud fields. All of the texture features used are derived from the visible channel imagery, since the visible channel has the highest spatial resolution.

2.3.3.1.1 Gray Level Run Length Features

Gray level run length (GLRL) features are based on homogeneous gray level runs. Any gray level image can be decomposed into a series of gray level runs in some predefined orientation, where each run is a series of consecutive pixels of the same intensity. Run lengths are often defined in raster images at orientations in increments of 45 degrees, starting at 0 degrees. For an image with M gray levels and a maximum run length of N, the gray level run length matrix is M by N. The i,j^{th} element of the matrix denoted by Φ_{ij} is the number of runs with intensity i and length j. For a given pixel

location, the pixels within a specified region centered on the given location are used to compute the matrix Φ_{ij}. Functions computed based on the matrix serve as the features. A series of such features have been defined for GLRL matrices by Galloway (1975), and later by Chu et al. (1990). The seven features based on GRGL, f_1 through f_7 used in this study are

Short Run Emphasis

$$f_1 = \frac{1}{s}\sum_{j=1}^{N}\frac{r_j}{j^2} \tag{2.17}$$

Long Run Emphasis

$$f_2 = \frac{1}{s}\sum_{j=1}^{N} r_j j^2 \tag{2.18}$$

Gray Level Nonuniformity

$$f_3 = \frac{1}{s}\sum_{i=1}^{M} g_i^2 \tag{2.19}$$

Run Length Nonuniformity

$$f_4 = \frac{1}{s}\sum_{j=1}^{N} r_j^2 \tag{2.20}$$

Run Percentage

$$f_5 = \frac{1}{n_p}\sum_{j=1}^{N} r_j = \frac{s}{n} \tag{2.21}$$

Low Gray Level Run Emphasis

$$f_6 = \frac{1}{s}\sum_{i=1}^{M}\frac{g_i}{i^2} \tag{2.22}$$

High Gray Level Run Emphasis

$$f_7 = \frac{1}{s}\sum_{i=1}^{M} g_i i^2 \tag{2.23}$$

Where the quantities r_j, g_i, s, and n are defined as follows:

$r_j = \sum_{i=1}^{M} \Phi_{ij}$, number of runs of length j

$g_i = \sum_{j=1}^{N} \Phi_{ij}$, number of runs of intensity i

$s = \sum_{i=1}^{M}\sum_{j=1}^{N} \Phi_{ij}$, total number of runs in image

n_p , number of pixels in image

2.3.3.1.2 Association Rules

Association rule texture features are based on frequently occurring local image structures. Association rules are often used in business applications to identify relationships in large databases. For example, in market basket analysis applications association rules describe which items are typically purchased together. Assume that there are two sets of distinct items $S_1 = \{A_1, A_2, \ldots A_m\}$, and $S_2 = \{A_{m+1}, A_{m+2} \ldots A_{m+n}\}$ such that whenever all the items in S_1 occur in a transaction, it is likely that all of the items in S_2 occur in the same transaction. This information is represented in the form of an association rule as follows:

$$(A_1 \wedge A_2 \wedge \ldots\ldots A_m) \Rightarrow (A_{m+1} \wedge A_{m+2} \wedge \ldots\ldots \wedge A_{m+n}) \tag{2.24}$$

where the "^" symbol represents the logical AND operator, and the "⇒" symbol represents implication. What exactly constitutes an item or a transaction depends on the application. In the case of market basket analysis, the items are the articles that a customer buys, and a transaction is the set of all items purchased together.

The left hand side of the rule consists of the items in set S_1, and is known as the antecedent. The right hand side of the rule consists of the items in set S_2, and is known as the consequent. Each association rule has a support value and a confidence value associated with it. The support for a rule is defined as the percentage of transactions for which all the items in both the antecedent and the consequent of the rule are present. The confidence value for a rule is defined as the conditional probability of all the items in set S_2 occurring in a transaction given that the items in set S_1 occur in the same transaction.

In order to use association rules for texture analysis it is necessary to define analogs for items, rules, support and confidence that capture the desired information from images. Association rules have been extended to capture local image statistics based on complex structuring elements. This was done by treating the pixels in the neighborhood of a given root pixel as the items occurring in a transaction, and treating the items as triples consisting of x offset, y offset, and pixel value. The offsets are specified relative to the root pixel for the transaction. This results in association rules of the form:

$$(X_1, Y_1, I_1) \wedge \ldots\ldots \wedge (X_m, Y_m, I_m) \wedge \ldots\ldots \wedge (X_{m+n}, Y_{m+n}, I_{m+n}) \tag{2.25}$$

For a given image, the support for a rule was defined as the percentage of root pixels for which both the antecedent and the consequent of the rule matched the image pixels. Similarly, the confidence value for a rule was defined as the percentage of root pixels for which the consequent matched given that the antecedent matched. For example, consider

the image shown in Figure 2.3. Since the x and y offsets of the rule range from 0 to1, the rule specified in Figure 2.3 can only be applied to this image at 9 of the 16 pixel locations. Of these 9 locations, the antecedent matches at 5 locations, and both the antecedent and consequent match at 3 locations. Therefore the support for the rule is 3/9 or 33.33% and the confidence of the rule is 3/5 or 60%.

	X=0	X=1	X=2	X=3
Y=0	2	0	2	1
Y=1	1	2	0	2
Y=2	2	0	2	1
Y=3	0	2	1	2

(0,0,2) ^ (1,1,2) => (1,0,0)

Support: 3/9 = 33.33%

Confidence: 3/5 = 60%

Figure 2.3 Association rules for a sample image.

Each association rule represents a particular local image structure, and its support value represents the frequency of occurrence of that structure. The confidence represents the conditional probability for one substructure given the presence of another substructure. These values are used as the texture features. An algorithm has been developed to mine images for association rules based on user specified constraints, including cardinality of the rules, pixel offsets, pixel values, and minimum support and confidence levels. The algorithm is similar to many traditional rule mining algorithms such as that described in Hinke et al. (2001). The result of the mining process is a list of association rules with support and confidence values for each texture of interest. While rule mining algorithms identify all of the rules that meet the user-defined criteria, it is generally the case that only a few of the rules are actually required to distinguish the textures of interest. Using the estimates of the distribution of support and confidence

values for each association rule and each texture class, it is possible to determine how well a given rule separates any two texture classes. This information is used to select a small subset of the rules that may be used as features (f_8) for texture classification and segmentation. Details on the operation of the rule mining and selection algorithms are found in Hinke et al. (2001).

2.3.3.2 Edge Detection Features

Edge detection techniques are frequently used for detecting discontinuities in an image. These filters work on the premise that the regions under scrutiny are sufficiently homogenous, allowing the transition between two regions to be determined by the basis of gray level discontinuities alone. These techniques apply a local derivative operator on the image. The sign of the second derivative is used to determine whether an edge pixel lies on the dark or light side of an image.

For cumulus cloud fields, one would expect the number of edges detected to be higher compared to other cloud types or background. Thus, output from edge detection filters can be used as features for discrimination of cloud fields. In this study, outputs from the Sobel filter, the Laplacian filter and a combination of outputs from both the filters are used as features.

2.3.3.2.1 Sobel Filter

The Sobel filter calculates the magnitude of the maximum rate of change (∇g) of gray level and the direction $\beta(x,y)$ of this change vector which are used as features (f_9-f_{10}). Since computations of gradients and their directions are based on partial derivatives, these derivatives are implemented in digital form using a mask (Figure 2.4). For pixel location Z_5, the surrounding 8 pixels are used to compute f_9 and f_{10}.

$$f_9 = \nabla g = |G_x| + |G_y| \tag{2.26}$$

$$f_{10} = \beta(x, y) = \tan^{-1}\left(\frac{G_x}{G_y}\right) \tag{2.27}$$

Where G_x and G_y are dependent on the surrounding eight pixels as follows:

$$G_x = (z_7 + 2z_8 + z_9) - (z_1 + 2z_2 + z_3) \tag{2.28}$$

$$G_y = (z_3 + 2z_6 + z_9) - (z_1 + 2z_4 + z_7) \tag{2.29}$$

Z_1	Z_2	Z_3
Z_4	Z_5	Z_6
Z_7	Z_8	Z_9

Figure 2.4. The 3 x 3 mask configuration used for Sobel and Laplacian edge detection.

2.3.3.2.2 Laplacian Filter

The Laplacian of a 2-D gray level function *g(x,y)* is a second order derivative defined as:

$$\nabla^2 g = \frac{\partial^2 f}{\partial x^2} + \frac{\partial^2 f}{\partial y^2} \tag{2.30}$$

Similar to the Sobel filter a 3 x 3 mask (Figure 2.4) is used for the computation of the Laplacian. The commonly used implementation for Laplacian filter based on the mask is:

$$f_{12} = \nabla^2 g = 4z_5 - (z_2 + z_4 + z_6 + z_8) \tag{2.31}$$

2.3.3.3 Training of the Maximum Likelihood Classifier

For the training of the classifier, a set of samples (50) was selected from twelve different GOES scenes and labeled by experts. Images belonging to the training set were labeled by assigning each pixel to one of the three possible classes: cumulus cloud field, other types of clouds, or background. Each scene was labeled by at least two experts, and

only those pixels for which there was agreement among the experts were used for training. From the five sets of features (GLRL, AR, Laplacian, Sobel, and Sobel-Laplacian), six classifiers (C_1 –C_5) were developed using the different types of feature vectors for training. The feature vectors corresponding to each of these classifiers are shown in Table 2.2. For training the classifiers, associated feature vectors are calculated for all pixels belonging to a particular class with the aid of expert labeled images. Then using equations (2.14) and (2.15) the parameters of the probability density function are determined. The process is repeated for all of the classes. Once the parameters for all of the classes are determined, any feature vector of unknown membership can be classified using (2.13) and (2.16).

Classifier	Feature vector (x)
C_1	$[f_1, f_2, f_3, f_4, f_5, f_6, f_7]$
C_2	$[f_8]$
C_2	$[f_9, f_{10}]$
C_4	$[f_{11}]$
C_5	$[f_9, f_{10}, f_{11}]$

Table 2.2: Feature vectors used in training and classification of different maximum likelihood classifiers.

The trained classifiers are used to classify the thirty independent scenes used in this study. The classified output for the thirty scenes is compared against the expert labeling to determine the classification accuracy. The classification accuracy then is examined as a function of template size used for computing the texture features. The computational requirement for various classifiers as a function of template size also is examined.

2.4 Results

The scenes used in the study are classified using the various algorithms, and the resulting outputs are compared against the expert labeling for the scenes. The comparisons are conducted for estimating optimal values of parameters associated with the algorithms and also for evaluating and intercomparing the performances of the various algorithms. In order to compare the labeling of a given algorithm against the corresponding expert labeling, the following quantities are determined: 1) λ_c, the percentage of pixels both the algorithm and expert labels as belonging to class C; 2) λ_{m+}, the percentage pixels labeled by the algorithm as a member of class C, but labeled by the experts as a nonmember; 3) λ_{m-}, the percentage of pixels labeled by algorithm as not belonging class C, but labeled by the expert as class C. The values of λ_c, λ_{m+} and λ_{m-} are calculated using the following expressions:

$$\lambda_c = \frac{p_c}{p_c + p_{m+} + p_{m-}} \cdot 100 \tag{2.32}$$

$$\lambda_{m+} = \frac{p_{m+}}{p_c + p_{m+} + p_{m-}} \cdot 100 \tag{2.33}$$

$$\lambda_{m-} = \frac{p_{m-}}{p_c + p_{m+} + p_{m-}} \cdot 100 \tag{2.34}$$

where p_c is the number of pixels labeled by both the algorithm and the expert as belonging to class C, p_{m+} is the number of pixels labeled by algorithm as belonging to class C but not by the expert, and p_{m-} is the number of pixels labeled by the expert as belonging to class C but not by the algorithm.

The λ_c is the percentage classification accuracy, λ_{m+} is percentage contamination of class C by pixels of other classes and λ_{m-} is the percentage of class C pixels that were not detected.

2.4.1 Structural Thresholding Algorithm

The experts labeled cloud masks for twelve selected training scenes. These were used to determine appropriate values for the parameters A_t, L, and N_t. The appropriate value for A_t was deduced by comparing the cloud mask created by the region growing procedure using varying values of A_t to the expert labeled cloud mask. The value of A_t was varied from 10 to 60 in increments of unity. For each scene, the labeling of every pixel by the expert was compared against that created by the algorithm with that particular value A_t. From these comparisons the values of λ_c, λ_{m+}, and λ_{m-} were calculated using expressions (2.32) - (2.34). The values of λ_c, λ_{m+}, and λ_{m-} were averaged, shown in Figure 2.5 as a function of A_t. The standard deviation of classification accuracy λ_c is also shown in Figure 2.5. Notice that the cloud classification accuracy is highest (~92%) and the standard deviation is smallest for group mean gray level threshold of about 30. The mislabeling of clouds as background and background as clouds is also lowest when the group mean gray level threshold is about 30. Also note that the results are relatively insensitive to a range of A_t values between 27 and 33. Thus a value of 30 for A_t is used in this study.

The optimal values for L and N_t are determined by analyzing the accuracy of cumulus cloud field labeling by the Structural Thresholding algorithm for varying values of L and N_t. The Structural Thresholding algorithm is applied to the 12 training scenes, with values of L varying from 12 to 52 pixels in increments of 4, and N_t varying from 2 to 36

in increments of unity. For each scene the expert labeling at every pixel location is compared against the labeling by the algorithm with a particular value of L and N_t. Then using expression (2.32) – (2.34), values of λ_c, λ_{m+}, and λ_{m-} are determined for each scene. The λ_c, λ_{m+}, and λ_{m-} values for the twelve scenes then are averaged.

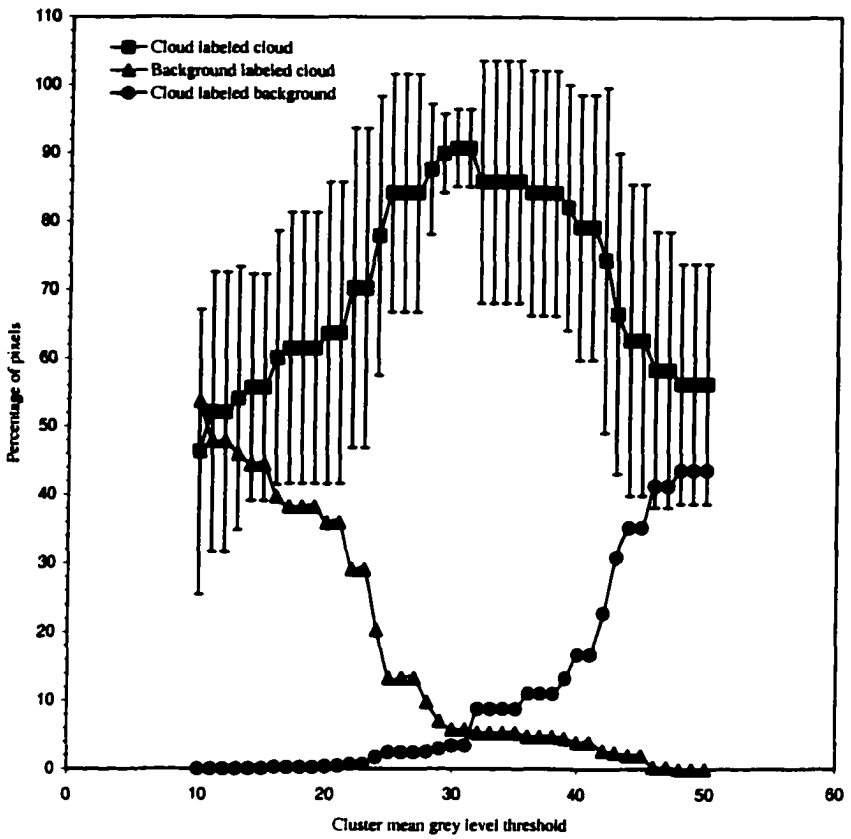

Figure 2.5: Sensitivity of detection of all cloud mask to cluster mean gray level threshold.

The contour plot of classification accuracy, λ_c averaged for the twelve scenes, as function of template size L and number threshold N_t, is shown in Figure 2.6. The analysis also shows template size L must be greater than 20 for mean λ_c to be greater than 85%. Notice that for template size greater than 20 km, for a constant value of L, classification accuracy initially increases with increasing values of N_t. The classification accuracy reaches a maximum value at some N_t and then decreases with further increase in N_t. For

example at L = 28 km, classification accuracy increases from about 80% at N_t = 2 to a maximum of about 87.4% at N_t = 6. Further increase in N_t result in decrease of classification accuracy reaching values of about 60% at N_t = 14. The maximum mean value λ_c (87.4%) corresponds to L of 28 and N_t of 6.

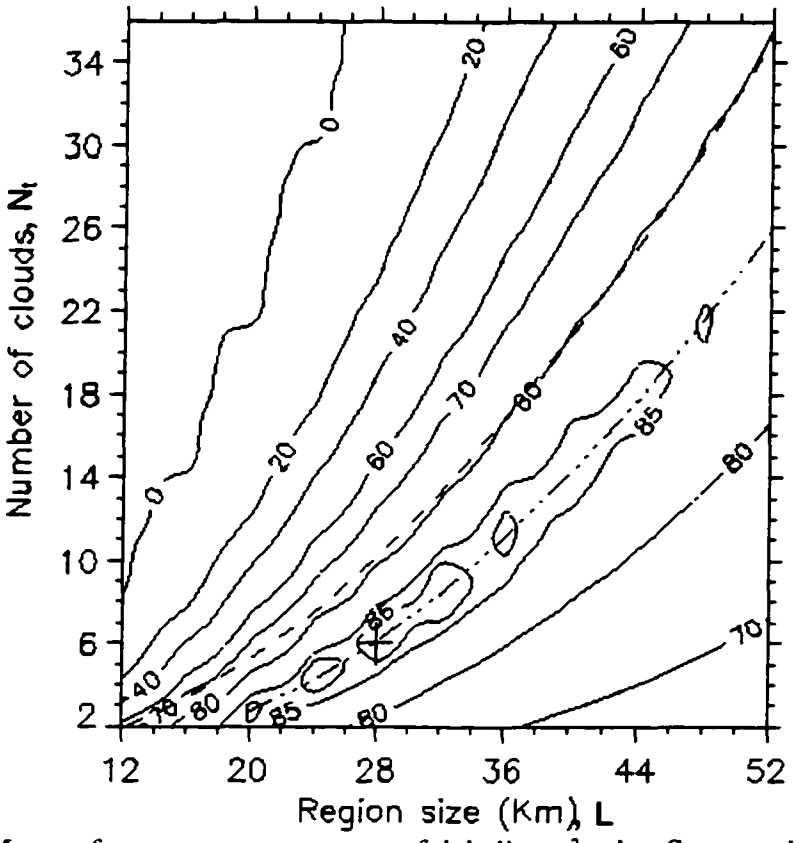

Figure 2.6: Mean of percentage accuracy of labeling λ_c, by Structural Thresholding algorithm as a function of L and N_t for the 12 training scenes used in this study. The dot dashed line is the second order polynomial fit to values of L >= 20 and corresponding values of N_t that yields the highest accuracy of labeling. Cross hair in the plot marks the L and N_t values that yield the highest average percentage accuracy.

For each of the values of L > 20, the N_t value that yields the maximum average classification accuracy is determined. A second degree polynomial is fit to the (N_t,L) value pairs, that maximizing λ_c for each L. The functional relationship between L and N_t that maximizes λ_c is:

$$N_t(L) = 0.01123L^2 - 0.0584L - 0.8679, \text{ for } L >= 20 \quad (2.35)$$

The expected number of clouds as function of L, $N(L)$ derived from observations of cumulus cloud field size distribution and given by expression (2.10), is also shown in the same Figure 2.6 as a dashed line. Notice that if equation (2.10) is used to specify N_t, the classification accuracy obtained is about 80%, which is less than the classification accuracy achieved using equation (2.35).

In this study the values of N_t and L were fixed at 6 and 28 respectively, with these values maximizing the mean value λ_c. However for values of N_t and L that satisfy (2.35), the mean classification accuracy is very close to the maximum value (to within ± 1%). Thus in practice any pair of N_t, L values satisfying (2.42) may be used without significant loss of classification accuracy. Lower values of L may be chosen for increased computational efficiency with a small penalty in classification accuracy.

The Structural Thresholding algorithm was applied to thirty independent scenes. The λ_c, λ_{m+} and λ_{m-} values and their means and standard deviations were derived from comparisons between cumulus cloud field masks labeled by the experts and the algorithm. The means and standard deviations are shown in Table 2.3. For cumulus cloud field detection, the Structural Thresholding algorithm classification accuracy λ_c has a mean value of 87.5% and standard deviation of 6.2% for the thirty scenes used in this study. The percentage of cloud field pixels that are not detected by the algorithm, λ_{m-}, has a mean value of 10.0%. The percentage of pixels mislabeled as cumulus cloud field by the algorithm, λ_{m+}, has a mean value of 2.5% for the thirty scenes. The percentage of cumulus cloud field pixels that are not detected by the algorithm is greater than the

percentage of pixels erroneously labeled as cumulus cloud field. Overall, the Structural Thresholding algorithm thus underestimates regions of cumulus cloud fields.

	λ_c (%)	λ_{c-} (%)	λ_{c+} (%)
Mean	87.5	10.0	2.5
Standard Deviation	6.2	6.2	2.3

Table 2.3. The λ_c, λ_{m+}, and λ_{m-} values derived from a) comparison between cumulus cloud field masks labeled by the expert and the Structural Thresholding algorithm.

Once the cumulus cloud field mask for a scene is created, the individual cumulus clouds within the scene are identified. The cloud elements in the "all-cloud mask" that lie within the detected cloud fields are labeled as cumulus clouds. Similarly, using the expert labeled cloud field and the all-cloud mask, an expert labeled cumulus cloud mask is created. The λ_c, λ_{m+}, and λ_{m-} values derived from comparing the cumulus cloud masks labeled by experts and the Structural Thresholding algorithm are shown in Table 2.4. The average λ_c, λ_{m+}, and λ_{m-} values are 93.3%, 5.4%, and 1.3% respectively. The Structural Thresholding algorithm slightly underestimates the cumulus cloudiness.

	λ_c (%)	λ_{c-} (%)	λ_{c+} (%)
Mean	93.3	5.4	1.3
Standard Deviation	5.1	4.6	3.3

Table 2.4: The λ_c, λ_{m+}, and λ_{m-} values derived from comparison between cumulus cloud masks labeled by the expert and the Structural Thresholding algorithm.

The average computation time taken by the Structural Thresholding algorithm to classify the thirty scenes used in this study as a function of template size L is shown in Figure 2.7. The computation time shows an approximate linear increase with increasing

L. The average computation time for L =28 km is approximately 4 seconds on a 450 Mhz Intel Pentium processor. Note that lower values of L can be used without significant loss of classification accuracy, thus increasing the computational efficiency.

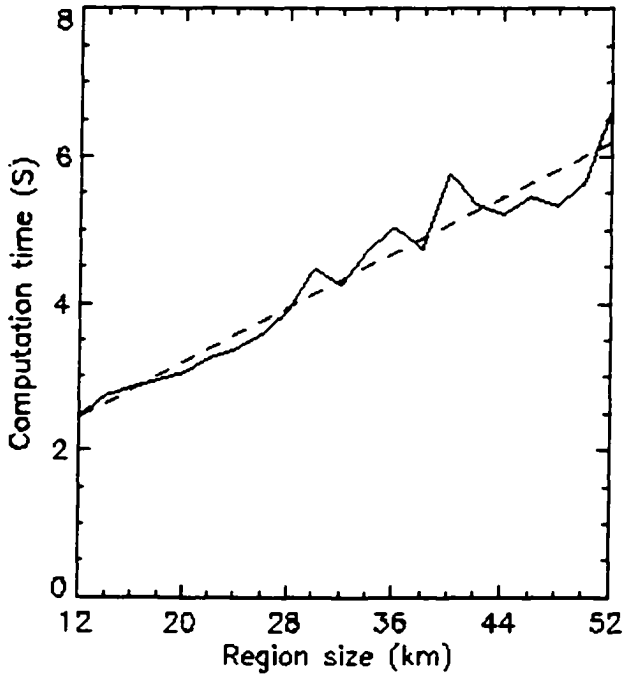

Figure 2.7: The average computation time (solid line) for structural thresholding algorithm as a function of region size for the scenes used in this study. The linear fit to the data is shown using the dashed line.

2.4.2 Maximum Likelihood Classifier

The cumulus cloud field masks generated using the Maximum Likelihood classifier based on various features are compared against expert-labeled cumulus cloud field masks. The mean cumulus cloud field classification accuracies (λ_c) as a function of template size, for Maximum Likelihood classifier utilizing various texture and edge detection features are shown in Figure 2.8. For all texture and edge detection features, the Maximum Likelihood classifier shows accuracies asymptotically increasing with increasing template size. The Maximum Likelihood classifier using Laplacian-Sobel features has the highest accuracy of 83.8% at template size of 11, followed by the AR

features with 83.2% accuracy. The Maximum Likelihood classifier with Laplacian edge detection features ranks next with accuracy of 82.8%, slightly higher than the 82% classification accuracy for Sobel edge detection features. Of all the approaches studied, the GLRL features result in the lowest classification accuracy of 78.2%.

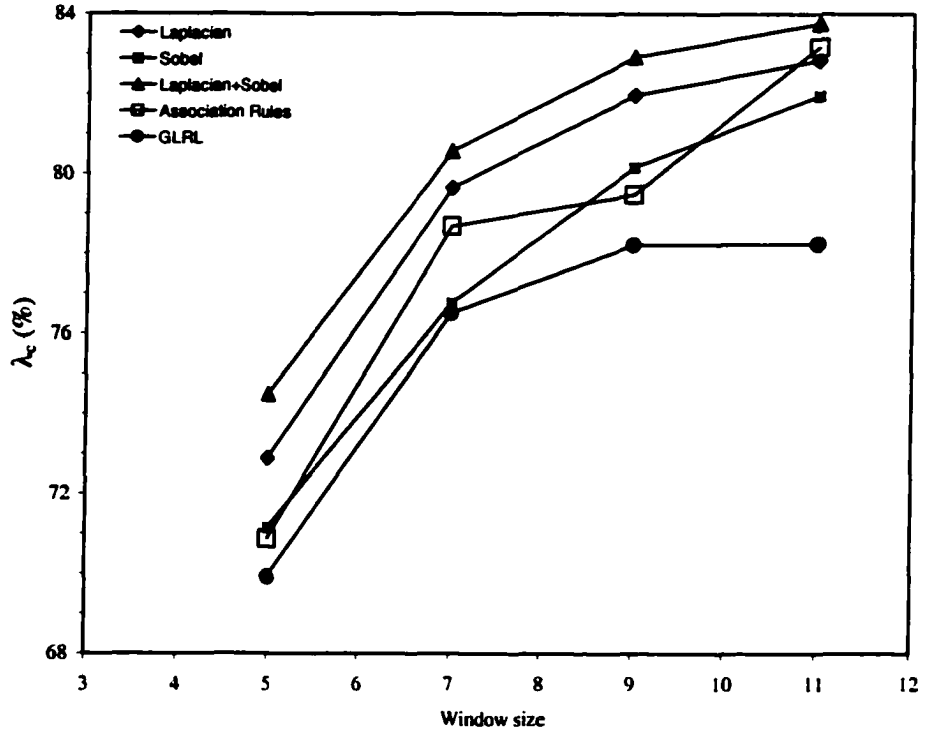

Figure 2.8: The percentage of pixels that are correctly classified as cumulus cloud fields by the various classifiers, as a function of template size.

The variation in mean percentage of cumulus cloud field pixels that are labeled as background or other cloud type ($\lambda_{m\text{-}}$) by the Maximum Likelihood classifiers as a function of template size is shown in Figure 2.9. For all the features, with the exception of the GLRL, the percentage of cumulus cloud field pixels erroneously labeled by the Maximum Likelihood classifier as other classes ($\lambda_{m\text{-}}$), decreases with increasing template size. The $\lambda_{m\text{-}}$ values vary from 14.9 to 3.4%, 15.9 to 3.6%, and 19.9 to 8.5% as the template size varies from 5 to 11 for Laplacian-Sobel, Laplacian, and Sobel features,

respectively. For a template size variation of 5 to 11, the Maximum Likelihood classifier using AR features shows λ_{m-} values changing from 22.5 to 4.9%. The λ_{m-} values for GLRL decreases from 24.2 to 15.8% as the template size increases from 5 to 9. However, the λ_{m-} value for Maximum Likelihood classifier utilizing GLRL features increases to 16.6% when the template size is increased to 11.

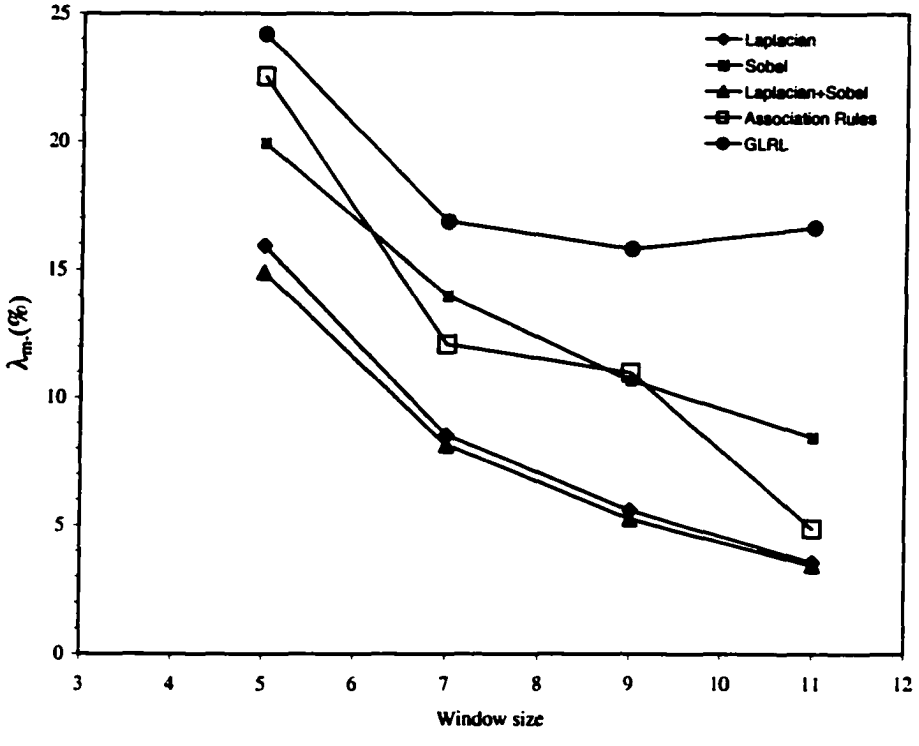

Figure 2.9: The percentage of cumulus cloud field pixels incorrectly labeled as others pixels for the various classifiers given as a function of template size.

The variation of λ_{m+}, the percentage of background and other cloud types labeled as cumulus cloud fields for the Maximum Likelihood classifier as a function of template size used for computing the various features is shown in Figure 2.10. With the exception of GLRL features, the λ_{m+} value for the Maximum Likelihood classifier increases weakly as the template size increases. As the template size varies from 5 to 11, λ_{m+} values increase from 10.6 to 12.8%, 11.2 to 13.6%, and 8.9% to 9.5% for the Maximum

Likelihood classifier using Laplacian-Sobel, Laplacian, and Sobel features, respectively. For the AR feature, λ_{m+} values increase from 6.6% to 11.9% for template size varying from 9 to 11. The Maximum Likelihood classifier using GLRL features shows the λ_{m+} value initially increasing from 5.9% to 6.6% as template size vary from 5 to 7. However, further increases in template size shows a reduction in λ_{m+}, with a value of 5.2% at template size of 11.

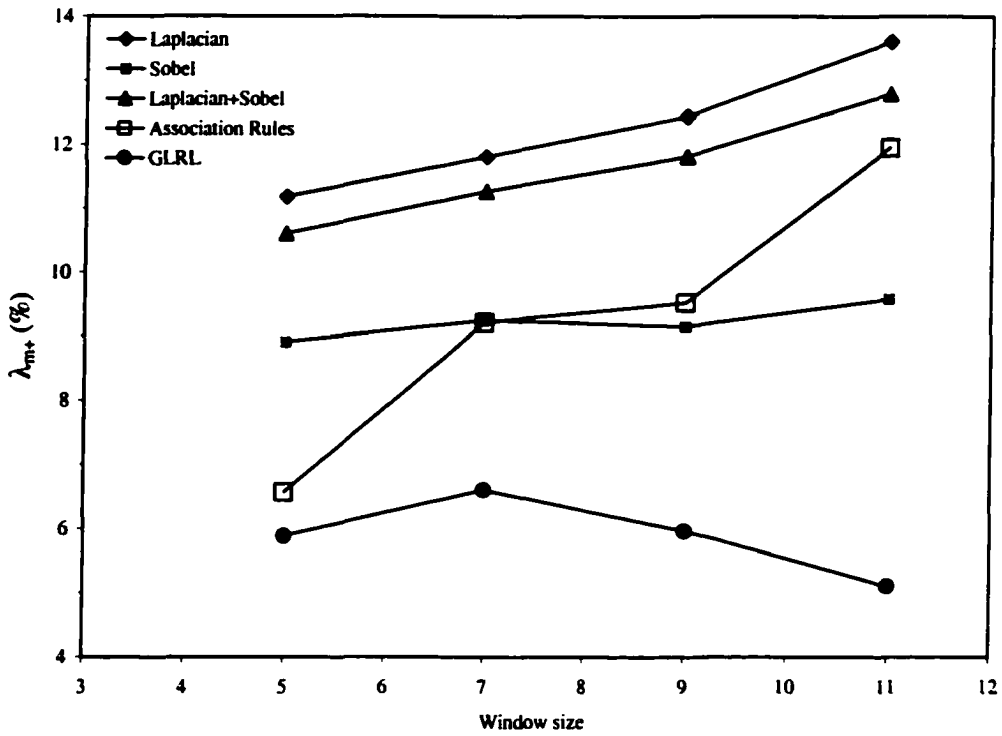

Figure 2.10: The percentage of pixels from other classes incorrectly labeled as cumulus cloud field by various classifiers, as a function of template size.

For the Maximum Likelihood classifiers utilizing Laplacian-Sobel, Laplacian, Sobel and AR features, the main source of classification error is from non-cumulus cloud field pixels being erroneously labeled as cumulus cloud field pixels. The classifiers thus overestimate the amount of cumulus cloudiness. However, for the Maximum Likelihood classifier using GLRL features, the main source of classification error is from undetected

cumulus cloud field pixels. The Maximum Likelihood classifier using GLRL thus underestimates the amount of cumulus cloudiness.

The average computation times for the Maximum Likelihood classifier using various types of features to process the 30 scenes used in this study, as a function of template size, are shown in Figure 2.11. The results shown are for a 450 Mhz Intel processor. For the edge detection filter features, the Maximum Likelihood classification times vary

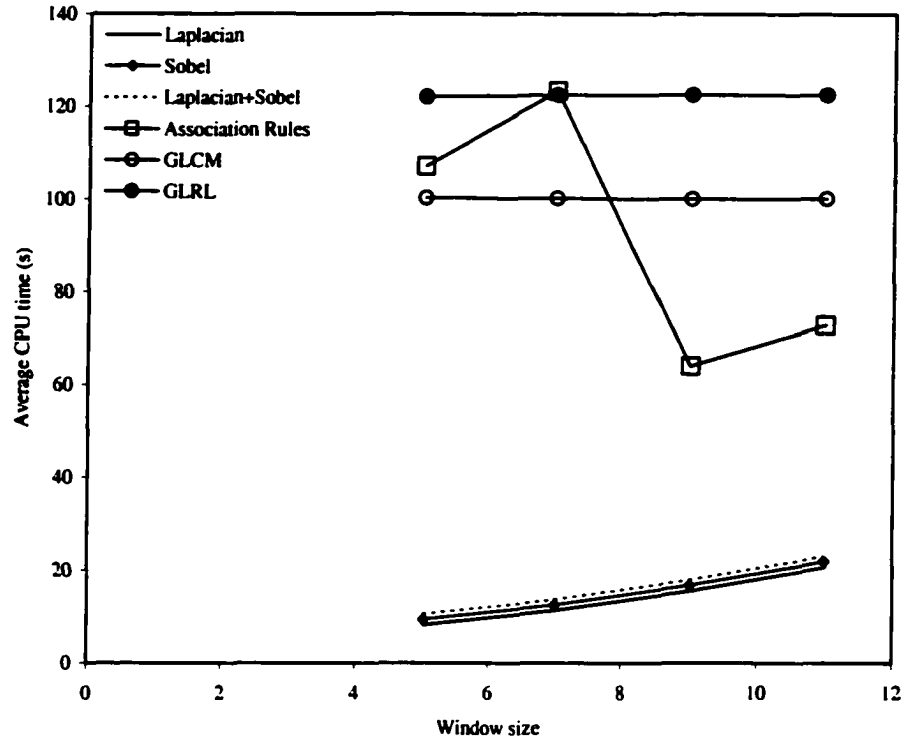

Figure 2.11: Average computation time for various classifiers as a function of template size.

exponentially with template size, with values of 8 - 11 seconds and 20 - 23 seconds for template sizes 5 and 11, respectively. The Maximum Likelihood classifier using Laplacian features has the lowest computational requirement, followed by the Sobel and the Laplacian-Sobel classifiers. Of the texture-based features, the Maximum Likelihood classifier using AR features has the highest computational requirement, followed by the

GLRL classifier. The computation time for the GLRL Maximum Likelihood classifier shows negligible change with varying template sizes, with approximate values of 122 s. The computation time for the Maximum Likelihood classifier using AR features varies significantly with template size, with values of 107, 123, 64, and 72 seconds at template sizes of 5, 7, 9, and 11, respectively.

2.4.3 Discussion

The boundary layer cumulus cloud fields identified by the different techniques for one selected scene (Figure 2.1c), are shown in Figure 2.12. The outline of regions identified by experts as the cumulus cloud fields is shown in Figure 2.12a. The outline of the cumulus cloud field identified by the Structural Thresholding algorithm is shown in Figure 2.12b. The Structural Thresholding algorithm does not classify pixels in the region 14 pixels wide along the lateral boundaries of the scene. But in the other regions, the boundaries of cumulus cloud fields labeled by the algorithm (Figure 2.12b) are in close agreement with those chosen by the expert (Figure 2.12a). However, the algorithm misses some clouds at the boundaries as the number density of clouds decreases below the threshold and as the cloud field edges become irregular. The algorithm detects holes (small clear areas) within cloud fields were not identified by the experts, as shown in the lower left corner of Figure 2.12b. Indeed, the experts broadly identified the prominent boundaries of the cloud fields. Since the experts did not identify some of the holes within the cloud fields, and if this is taken into account in calculating the classification accuracy, the average classification accuracy for the Structural Thresholding algorithm will be slightly higher than the 87.5% cited.

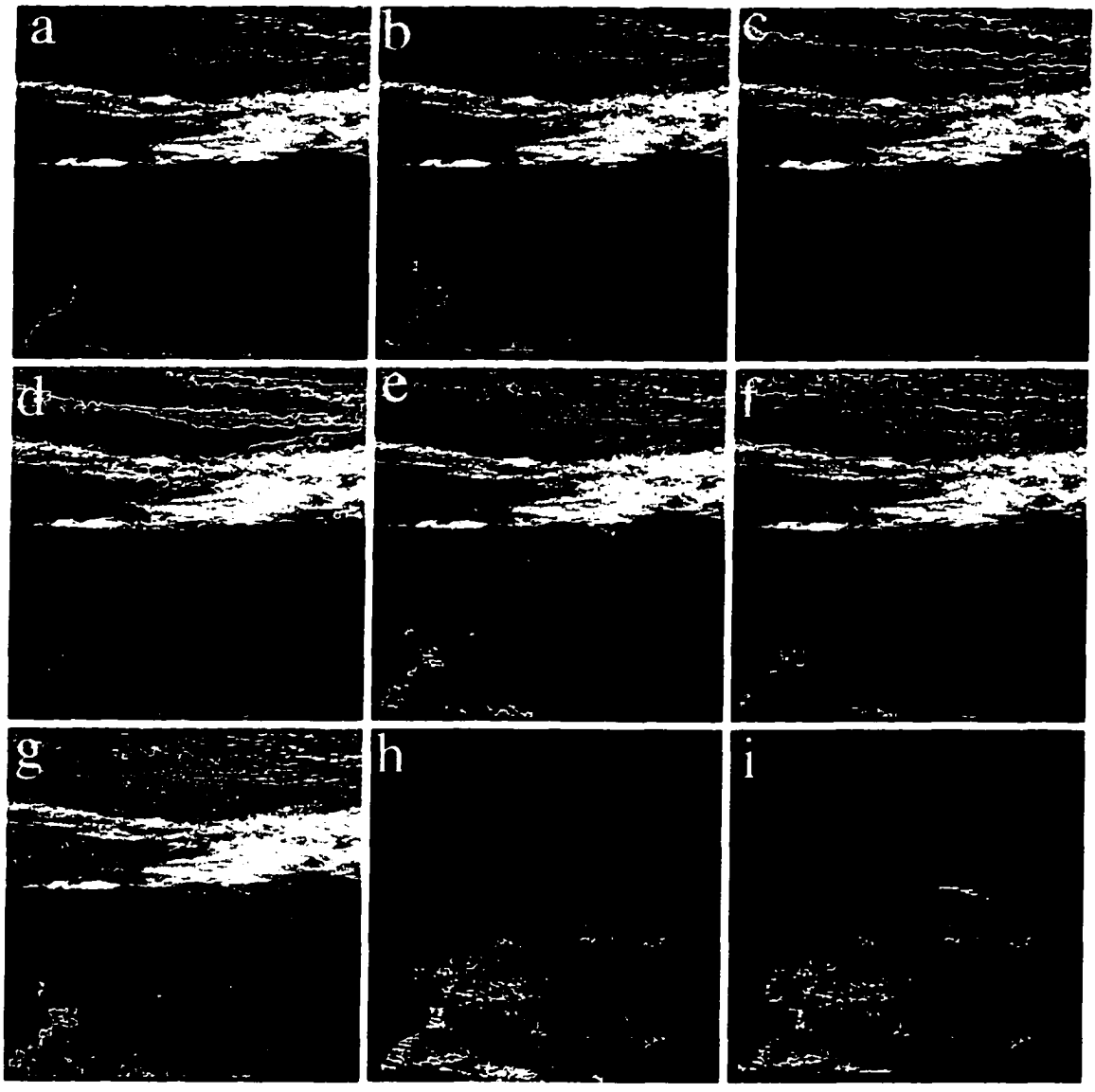

Figure 2.12: The cumulus cloud field outline for scene 2.1c, derived from labeling by: a) expert; b) Structural Thresholding; c) Laplacian-Sobel; d) Laplacian; e) Sobel; f) Association Rules classifier; and g) Gray Level Run Length classifier. Cumulus cloud mask labeled by: h) expert; i) Structural Thresholding algorithm.

The cumulus cloud field masks generated for by the Maximum Likelihood classifier based on the Laplacian-Sobel, Laplacian and Sobel features, for template size of 11 are shown in Figures 2.10c, 2.10d, and 2.10e, respectively. Notice that the Maximum Likelihood classifiers based on the edge detection features classifiers misclassify some of

the cirrus clouds (top of the image) and also the edges of other cloud systems as cumulus cloud fields. The cumulus cloud field mask for the Maximum Likelihood classifier utilizing the AR features at template size of 11 (Figure 2.12f) also misclassifies along the edges of other cloud systems. Finally, the Maximum Likelihood classifier using GLRL features has marginally better performance along boundaries of other cloud systems (Figure 2.12g). However, the Maximum Likelihood classifier based on GLRL features mislabels some of the regions within the cloud fields as background. Notice that all of the classifiers identify the prominent hole in the cloud field as shown in the lower left region in Figures 2.10c – 2.10g. For the various Maximum Likelihood classifiers, accuracy values may be higher than those, if the presence of these small holes within the cloud fields is better represented in expert labeling.

Comparison between cumulus cloud field masks created by the various techniques shows that the lower performance of the Maximum Likelihood classifier, compared to Structural Thresholding algorithm, is mainly due to misclassification along the edges of other cloud systems. Undulating structures along the lateral boundaries of some cloud systems leads to the presence of a large number of edges. The Maximum Likelihood classifier based on edge detection features tend to misclassify these areas as cumulus cloud fields, since high gradient edges are characteristic of cumulus cloud fields. The Maximum Likelihood classifier using AR and GLRL features also has difficulty distinguishing such regions from cumulus cloud fields. Along such regions the Structural Thresholding algorithm has the advantage since it uses the count of clouds per unit area rather than quantities derived from gray level variations. Under certain situations, small areas of cloud debris along the edges of larger-scale cloud systems could result in cloud

number density consistent with those for cumulus cloud fields. However, the filtering of the small-scale features detected by the Structural Thresholding algorithm reduces misclassification of this nature. If the small-scale features detected by the Maximum Likelihood classifiers are filtered, the classification accuracy may improve, but with added computational overhead.

Beyond a template size of 11 the Maximum Likelihood classifiers based on various feature sets do show marginal increases with increasing template size. However for the best performing Laplacian-Sobel edge detection based classifier increasing template size beyond 11 is not practical, because marginal increase in accuracy is accompanied by exponential increase in computation time with increasing template size.

In addition to cumulus cloud fields, the Structural Thresholding algorithm also detects individual cumulus clouds within the cloud fields. Figure 2.12 shows the comparison between a cumulus cloud mask labeled by the experts (Figure 2.12h) and by the Structural Thresholding algorithm (Figure 2.12i). Notice the close agreement between the masks. The differences in labeling between the experts and the algorithm are mainly along the boundaries of the cloud field and also in regions where cumulus clouds are very clustered. In general, however, there is very good agreement.

2.5 Conclusions

Boundary layer cumulus cloud fields, persistent features in many parts of the world, are strongly influenced by the surface conditions. Monitoring of boundary layer cumulus cloud fields over areas of varied land use is expected show indications of surface influencing the local climate. This requires processing of large volumes of satellite data. Automatic boundary layer cumulus cloud field detection schemes are needed for this

purpose. Currently such techniques are not available. The current study investigates and intercompares accuracy and computational requirements for several automated boundary layer cumulus cloud field detection techniques. The methods used in this study are the Structural Thresholding algorithm, Maximum Likelihood classifier based on Laplacian, Sobel, Sobel-Laplacian edge detection features, as well as GLRL and AR texture features.

The Structural Thresholding algorithm uses the number of clouds per unit area as a discriminant for detecting boundary layer cumulus cloud fields. A simple statistical thresholding method is used to create an all-cloud mask, which is then segmented to identify the number of clouds per unit area. Once the cloud field areal extent is identified, the clouds within the field are labeled as cumulus clouds. Sensitivity analysis is used to derive a second degree polynomial relating the expected number of clouds within a specified region to template size. Of all the schemes examined in this study, the Structural Thresholding algorithm has the highest average classification accuracy. The best performance is obtained when the threshold for labeling a pixel as cumulus cloud field is set to be the occurrence of at least 6 clouds within a region of 28 x 28 pixels. The average classification accuracy of Structural Thresholding algorithm under these conditions is 87.5% for cumulus cloud fields and 93.25% for cumulus clouds. The percentage of cumulus cloud field pixels labeled as other classes is 10% while other classes labeled as cumulus cloud fields is 2.5%. The average computation time required by Intel 450 Mhz Pentium processor for classification of a 512 x 512 scene is approximately 4 seconds.

Of all the Maximum Likelihood classifiers used in this study, the one based on Laplacian-Sobel has the highest classification accuracy. At a template size of 11 pixels, the average accuracy of detection for cloud fields for Laplacian-Sobel based Maximum Likelihood classifier is 83.8%. On average, cumulus cloud field pixels are mislabeled 12.8% of the time as other classes, while pixels belonging to other classes but erroneously labeled as cumulus cloud fields occur 3.4% of the time. The Maximum Likelihood classifier using the AR feature has the next best performance (83.2%), followed by the Laplacian (82.8%), Sobel (82%), and GLRL (78.2%) classifiers. The classification time requirements are significantly higher for the Maximum Likelihood classifiers based on texture features compared to those using edge detection features. Note that, even though the classification accuracy for the AR classifier is very close to that achieved by the Lapacian-Sobel classifier, the computational requirements for Laplacian-Sobel classifier (23 seconds) is significantly lower than that for AR classifier (72 seconds). The lower computational requirement and higher classification accuracy makes the Maximum Likelihood classifier based on Laplacian-Sobel features more attractive compared to ones based on the other features studied. The cause for significant differences in accuracy between the Maximum Likelihood classifiers and Structural Thresholding algorithm is because the later does not utilize quantities derived from gray level variations for discrimination of cumulus cloud fields, and also due to the filtering of detected smaller-scale features by the later technique. A similar procedure could be used with the classifiers to increase the detection accuracy of the classifiers. However, this would create additional computational overhead for these techniques.

Based on the analysis presented in this study, the Structural Thersholding algorithm and the Laplacian-Sobel classifier appear to perform best for the detection of boundary layer cumulus cloud fields in satellite imagery. The necessity of the segmentation procedure associated with Structural Thresholding approach makes the computer memory requirements for this method significantly higher compared to Sobel classifier. For an $n \times n$ pixel scene, the memory requirements for Structural Thresholding approach is approximately O ($5n^2$) compared to O (mn) for the Laplacian-Sobel classifier, where m is the mask size used for evaluating the Sobel and Laplacian filter. Thus in situations where computer memory is a limiting factor, the Sobel classifier may be more attractive despite the lower performance. Note that both the cloud fields and the individual clouds within the field are identified by Structural Thresholding technique. However, the classifiers require an externally created all-cloud mask to identify the member clouds within the cloud field. Although the methods described here are tailored for GOES data (e.g., Lawton et al., 2001), they are applicable to other types of data with slight modifications. Indeed, this approach has been used successfully on Moderate Resolution Imaging Spectroradiometer (MODIS) data in Southwestern Australia (Ray et al., 2002) to identify boundary layer cumulus cloud fields.

The detection techniques developed in this study are currently being used to study boundary cumulus cloud field structure and characteristics. This study also illustrates the significant amount of information associated with cloud morphology that is potentially useful for cloud classification. Such information is currently not being used to its fullest potential (Pankiewicz, 1995), and we hope results from this study may provide motivation for its fuller utilization in cloud classification schemes.

Chapter 3

Impact of Land Use on Costa Rican Tropical Montane Cloud Forests: Sensitivity of Cumulus Cloud Field Characteristics to Lowland Deforestation

3.1 Introduction

Tropical montane cloud forests (TMCFs) depend upon predictable, frequent and prolonged immersion in cloud (Bruinjzeel and Proctor, 1995; Pounds et al., 1999). In the Cordillera de Tilarán of Costa Rica, anuran population crashes, increases in the upper elevation of bird ranges on the Pacific slope, and longer mist-free intervals in the dry season at the lee edge of the Monteverde TMCF have been attributed to an increase in the orographic cloud base due to changes in sea surface temperature (Pounds et al., 1999; Still et al., 1999). This study proposes an alternate hypothesis: that upwind lowland deforestation alters surface energy budgets in ways that reduce the development of tropical dry season cumulus cloud fields and raise cloud base heights. In this paper corroborating evidence is offered from remote sensing of clouds in northern Costa Rica and southern Nicaragua, and from regional atmospheric simulations of idealized simple lowland tropical forest and pasture landscapes. Since TMCFs are crucial components of most tropical biodiversity "hotspots", and play important roles in local and regional hydrological management, factors which influence TMCF distribution and water budget are a matter of considerable interest.

In the Caribbean basin, as in much of the tropics, TMCFs occur where mountains force trade winds to rise past the point at which adiabatic cooling results in cloud formation. In such settings, upwind regional landscape characteristics can influence the overlying atmosphere in ways that may have important consequences for cloud formation, and consequently for TMCFs.

It has been long recognized that through modulation of surface energy budgets, land use can have significant influence on the regional climate. Land-use changes are usually accompanied by variations in surface properties such as albedo, temperature, roughness length, water storage capacity of surface soil and soil moisture distribution (Otterman, 1974; Sagan et al., 1979; Anthes, 1984; Segal et al., 1988; Shukla et al., 1990; Meher-Homji, 1991; Gash and Nobre, 1997; Pielke 2001). Variations in surface properties also can cause changes in boundary layer air temperature, moisture, and depth, local rainfall and cloudiness (Segal et al., 1989; Bryant et al., 1990; Otterman, 1990; Schwartz and Karl, 1990; Meher-Homji, 1991; Bastable et al., 1993; Sud et al., 1993; Lyons et al., 1993; Gash and Nobre, 1997; Pielke et al., 1998; Pielke, 2001). Especially cumulus clouds are strongly influenced by the surface, since they form from thermals induced in the boundary layer.

The Costa Rican lowlands are an environmentally complex region in which the original tropical forests are being rapidly replaced by pastures and agricultural landscapes. Sader and Joyce (1988) estimate that the primary forest in Costa Rica decreased from 67% in 1940 to 17% in 1983. Land-use changes in the Caribbean lowlands can alter the nature of the air masses responsible for the formation of cumulus clouds in the lowlands as well as orographic clouds on the Caribbean slopes. In view of

the large-scale deforestation in the Caribbean lowland region east of Monteverde and the significant influence it may exert on cloud formation, land-use changes cannot be ruled out as a causative factor for the observed climate change in the Monteverde region. In this chapter the effects of lowland deforestation on cumulus cloud formation and development are examined using satellite data and a mesoscale numerical model.

The two main objectives of this study are to:

I. Use satellite imagery to examine the effect of deforestation on cloud formation.

II. Use numerical models to investigate the effects of deforestation on cloud characteristics, especially cloud base heights.

In this study Goestationary Operational Environmental Satellite 8 (GOES-8) data is used to examine differences in the nature of cumulus cloudiness between deforested and forested regions, which is a signal of land-use change influencing the regional climate. The Regional Atmospheric Modeling System (RAMS), a mesoscale numerical model, is used to investigate the effect of land-use change on lowland cumulus cloud characteristics. Section 3.2 describes the data, and Section 3.3 discusses the methodology used in this study. The results from both the analysis of satellite data and RAMS simulations are presented in Section 3.4, and Section 3.5 concludes.

3.2 Data

The GOES-8 satellite imagery is used to analyze patterns of cumulus cloudiness over the Costa Rican region. GOES-8 imagery has 5 spectral channels, one in the visible (0.52 – 0.72 μm) and four in the infrared region (3.78-4.03 μm, 6.47-7.02 μm, 10.2-11.2 μm, 11.5-12.5 μm). Spatial resolution at nadir for channel 1 is 1 km, 4 km for channels 2, 4, and 5, and channel 3 has nadir resolution of 8 km. The visible channel is used for the mapping of cumulus clouds in the present study. Daytime GOES-8 imagery over the Central American region is taken at 30 minute temporal resolution for the months of February, March and April, 1999. The GOES-8 visible channel data are calibrated and normalized by the cosine of solar zenith angle to yield the albedo values.

Landsat Multi Spectral Scanner (MSS) data is also used to examine the cloudiness in the Costa Rican region. Landsat MSS has four spectral bands in the range 0.5 to 0.6 μm, 0.6 to 0.7 μm, 0.7 to 0.8 μm, and 0.8 to 1.1 μm with spatial resolution of 57 m nadir. False color composite MSS scenes are used in this study to investigate deforestation and cloudiness patterns.

The 1200 UTC atmospheric soundings are used for initializing the mesoscale model simulations. The radiosonde data from the coastal plains of Costa Rica would be the ideal profiles for simulating the lowland cumulus cloud fields. However, since radiosonde data from the coastal planes are not available, six soundings from San Andres island (to the east, and upwind of Costa Rica) are used. These soundings are chosen for days characterized by relatively calm synoptic conditions and by the observed presence of fair weather cumulus clouds in Costa Rica. A typical example of the soundings used in this study is shown in Figure 3.1. Notice the well mixed boundary layer indicated by

approximately constant potential temperature and mixing ratio values at lower levels. The sounding also shows relatively gentle flow in the boundary layer. The convective available potential energy (CAPE), convective inhibition (CIN), and lifting condensation level (LCL) associated with these soundings are given in Table 3.1. The values of CAPE,

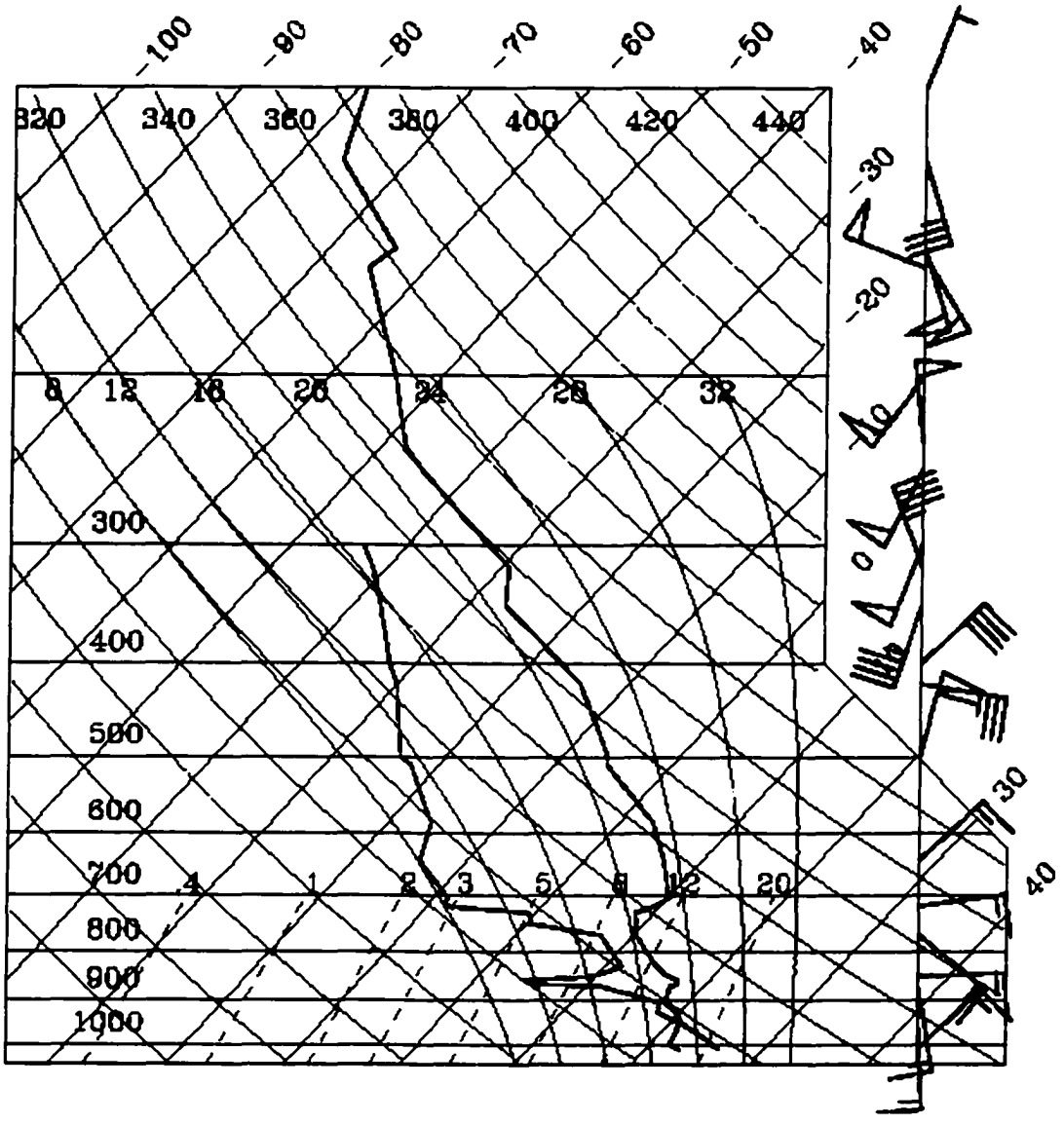

Figure 3.1: Skew-T plot of radiosonde data from San Andres for 12 UTC, 24 March 1999. The profile shown is representative of conditions used for initialization in numerical modeling experiments.

which indicates the energy available for convection, varying between 248 and 1404 J kg^{-1} are suitable for formation of fair weather cumulus. Low CIN values ranging between 1 and 3 J kg^{-1} implies an environment where convection can be easily initiated. Lifting condensation level values, which provide an estimate of cloud base during early hours of cloud formation, are within the range of cloud base heights estimated from Landsat data.

Sounding	Date	CAPE (J kg^{-1})	CIN (J kg^{-1})	LCL (m)
S1	3/01/1999	576	1	506
S2	3/03/1999	680	3	537
S3	3/11/1999	971	1	523
S4	3/19/1999	248	1	605
S5	3/24/1999	947	1	565
S6	3/27/1999	1404	1	411

Table 3.1: The date of acquisition and characteristics of the six 1200 UTC radiosonde observations, from San Andres island in the Caribbean, used in this study. The sounding characteristics listed are Convective Available Potential Energy (CAPE), Convective Inhibition (CIN), Lifting Condensation Level (LCL) and Level of Free Convection (LFC).

3.3 Methodology

3.3.1 Analysis of Satellite Data

The GOES-8 visible imagery is used to derive the frequency of occurrence of cumulus cloudiness in Costa Rica for the dry season months of February, March, and April 1999. Structural Thresholding, an automated cumulus cloud detection algorithm (Nair et al., 1999; 2001), described in Chapter 2, is used for detection of cumulus clouds.

The Structural Thresholding algorithm is used to derive the cumulus cloud mask daily at 1415 UTC, 1615 UTC, 1815 UTC, and 2015 UTC for the months of February, March, and April 1999. These months define the dry season for the Caribbean region of Costa Rica. It is expected that the influence of surface characteristics on cloud formation is most significant during the dry season, due to relatively calmer synoptic situations at this time. Also, the surface fluxes in forested and deforested regions are expected to be higher in the dry season due to a minima of precipitation. Once the daily cumulus cloud masks are extracted, the monthly maps of frequency of occurrence of cumulus clouds for 1415 UTC, 1615 UTC, 1815 UTC, and 2015 UTC over the Costa Rican region are derived. Frequency of cumulus cloud occurrence is expressed as a percentage, indicating the percentage of observations in a month for which cumulus clouds are present over a particular location. Once the monthly maps of frequency of occurrence of cumulus clouds are derived, digitized maps of deforestation for Costa Rican region are used to analyze cloudiness patterns as a function of deforestation.

3.3.2 Numerical Modeling Experiments

The Colorado State University Regional Atmospheric Modeling System (CSU RAMS) is utilized for the simulation of cumulus cloud fields. The RAMS model is nonhydrostatic and is used for the simulation of atmospheric phenomenon ranging from cloud scale to mesoscale (Pielke et al., 1992). The RAMS uses finite difference methods for solving the various conservation equations governing the atmospheric flow. Cloud microphysics is represented in RAMS using bulk water parameterization which includes cloud water, rain, pristine ice, snow aggregates, graupel and hail categories. At the lower boundary, RAMS uses a multilayer soil model (Tremback and Kessler, 1985) and a

vegetation model (Avissar and Pielke, 1989) to represent the land-surface processes. Various options are available for representation of radiative transfer, turbulence and lateral boundary conditions.

The effect of varied surface conditions on cloud formation was examined using a coupled design in which each of six sounding (*S1*-*S6*) was used for initialization of both forest and pasture atmospheric conditions. The impact of deforestation and conversion to pasture was examined by comparing diurnally developing conditions between simulations. It was assumed that the vegetation in the forest simulations had transfer characteristics of evergreen broadleaf forest, with initial volumetric soil moisture set to 0.4, while pasture simulations had transfer characteristics of short grass, with initial volumetric soil moisture set to 0.25. These forest volumetric soil moisture values are appropriate to tropical evergreen forest dry season values for the region (Dietrich et al., 1982), and the pasture volumetric soil moisture yields latent and sensible heat fluxes consistent with empirical micrometeorological studies over Amazonian pasture (Bastable et al., 1993).

The cloud field simulations were performed over a domain of 100 km x 100 km represented by 100 x 100 horizontal grid points at uniform horizontal grid spacing of 1 km. In the vertical, a stretched grid with a stretch ratio of 1.08 was used, providing vertical spacing ranging from 70 m near the surface to a maximum of 750 m higher up in the atmosphere. The terrain adopted in these model simulations was flat. A periodic boundary condition was assumed at the lateral boundaries, and a rigid top boundary was adopted. The Chen and Cotton (1983) radiative transfer scheme was used to account for the effect of clouds. Cloud formation processes other than those involving ice processes

were activated. Precipitation processes were not activated in these simulations to save computer processing resources since the cloud fields simulated were almost exclusively fair weather cumulus.

For each of the six soundings (*S*1-*S*6), the model was integrated with forest and pasture surface conditions for 12 hours starting at 1200 UTC, approximately local dawn. The cloud field simulations with atmospheric conditions represented by soundings *S*1 through *S*6 and forest surface conditions are referred as *F*1, *F*2, *F*3, *F*4, *F*5, and *F*6. Similarly the coupled simulations with pasture surface conditions are referred to as *P*1, *P*2, *P*3, *P*4, *P*5, and *P*6. For each simulation the atmospheric conditions were set to be horizontally homogenous with the vertical structure prescribed by each atmospheric sounding.

The diurnal variations of domain-averaged cloud base height, cloud top height, cloud thickness, cloud cover, cloud water mixing ratio, liquid water path, sensible heat flux, latent heat flux, surface temperature and surface dewpoint temperature from simulations *F*1 - *F*6 are compared against those from corresponding simulations *P*1 - *P*6. Vertical columns with integrated liquid water path greater than or equal to 0.2 kg m^{-2} were assumed to contain cumulus cloud. Within each column containing cumulus cloud, cloud base height was assumed to be the height of grid point with non-zero liquid water content closest to the surface. The cloud top height is chosen as the height of the topmost grid point of a run of consecutive non-zero liquid water content grid points, starting from the cloud base grid point.

3.4 Results

Both GOES satellite imagery analysis and the results from the CSU RAMS simulations for the coastal regions of Costa Rica are presented. The satellite analysis covers the dry season months of February through April 1999, in which the data has been processed hourly during the daylight hours. Results are generated in two-hour increments, at 1615, 1815, and 2015 UTC, showing the regions with persistent cumulus cloud fields. The results show that deforested regions have a lower incidence of cumulus clouds and that the clouds that do form in these regions are smaller than those in nearby forested regions. The numerical modeling simulations examine the diurnal development of cumulus clouds in both pastures and forests. In particular, it is found that clouds in forested regions have higher base heights, suggesting that the observed lifting of the clouds over Monteverde may be due to deforestation in the coastal lowlands. An assessment is made of the cloud field characteristics in these pasture and forested regions.

3.4.1 GOES-8 Satellite Imagery Analysis

Deforestation and agricultural conversion in Costa Rica has been rapid (estimated at 400-600 km^2/yr in the late 70's and early 80's; Sader and Joyce 1988), with the result that less than 1,000 km^2 of undisturbed forest remained on the Costa Rican portion of the coastal plain in 1993 (J. Mendez, personal communication). In contrast, political conflicts have hindered agricultural development in adjacent Nicaragua, with the result that the original forest there is much more intact. Figure 3.2a,b shows two false color LANDSAT images of Costa Rica on 2 February 1986 and 5 January 1985, respectively. Forested regions are seen as dark red, whereas the large deforested regions of the San Carlos (SC) and Tortuguero (T) plains are seen as pink. Gray areas occur in the deforested lee

(Pacific side) slopes in the Meseta Central (MC) south of Monteverde (M) and the Cordillera Volcanica Central (CC). Broken remnant forest (RF) is found in northern Costa Rica. Satellite imagery often shows that dry season cumulus clouds do not form in the San Carlos and Tortuguero plains. However, when cumulus clouds do form in these regions, as in Figure 3.2b, the clouds generally are smaller and less well developed than clouds just north of the border in the forested Nicaraguan lowlands (N).

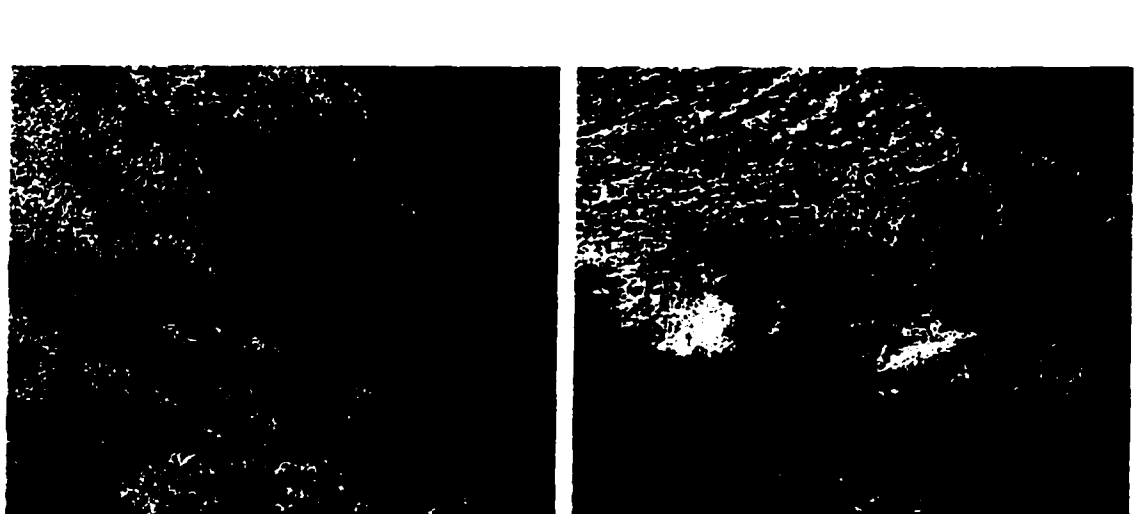

Figure 3.2: Deforestation and dry season cumulus cloud cover in northern Costa Rica and southern Nicaragua. False color Landsat images over Costa Rica for a) 6 February 1986 at 1521 UTC b) 5 January 1986 at 1512 UTC. The labeled areas in the images are San Carlos plains (SC), Tortuguero plains (T), Monteverde (M), Cordillera Volcanica Central (CC), deforested lee in the Meseta Central (MC), Remnant forest (RF) south of the Costa Rica-Nicaragua border and intact lowland forest covers southeastern Nicaragua (N). The color composite is created by combining red, green and blue intensities in proportion to brightness values for band 4, 2, and 1.

Figure 3.3a shows the forest cover in Costa Rica as green (Wheelwright, 2000). In particular, note the two deforested patches denoted as "SC" and "T" to the east of Monteverde in the Muelle San Carlos-Fortuna area in the coastal plains (as seen in Figure 3.2). These regions have been converted to pastures and plantations. The Wheelwright data corresponds well with the LANDSAT imagery, showing that there have been no

major deforestation activities since the mid-1980s in the Costa Rican coastal plains. Rather, there has been a gradual erosion of the forested regions at the boundaries.

Figure 3.3: a) Recent estimates of forest cover in Costa Rican region b) Topography of the Costa Rican region. The labeled areas in the images are San Carlos plains (SC) and Tortuguero plains (T).

Figure 3.3b shows the relief in the region. The Cordillera de Tilarán runs as a single sinuous central ridge (the continental divide) about 70 km from the western margin of Costa Rica's Meseta Central to the southeastern tip of the chain of isolated volcanoes which extends into Nicaragua. The Cordillera rises abruptly from the Pacific coast, reaching peaks of about 1800 m elevation 25 km inland. Furthermore, the Cordillera de Tilarán is downwind of the Nicaraguan/ Costa Rican Caribbean coastal plain study area, so that temporal trends in cloud impact on the Cordillera associated with deforestation can be identified.

Figure 3.4 shows the frequencies of occurrence of total cloud cover and cumulus cloud cover over southern Nicaragua and Costa Rica retrieved at 1615, 1815, and 2015 UTC for March 1999, using the method described in Section 3.3. Note the rapid decrease of cloud cover over Lake Nicaragua, located in the southwestern corner of Nicaragua

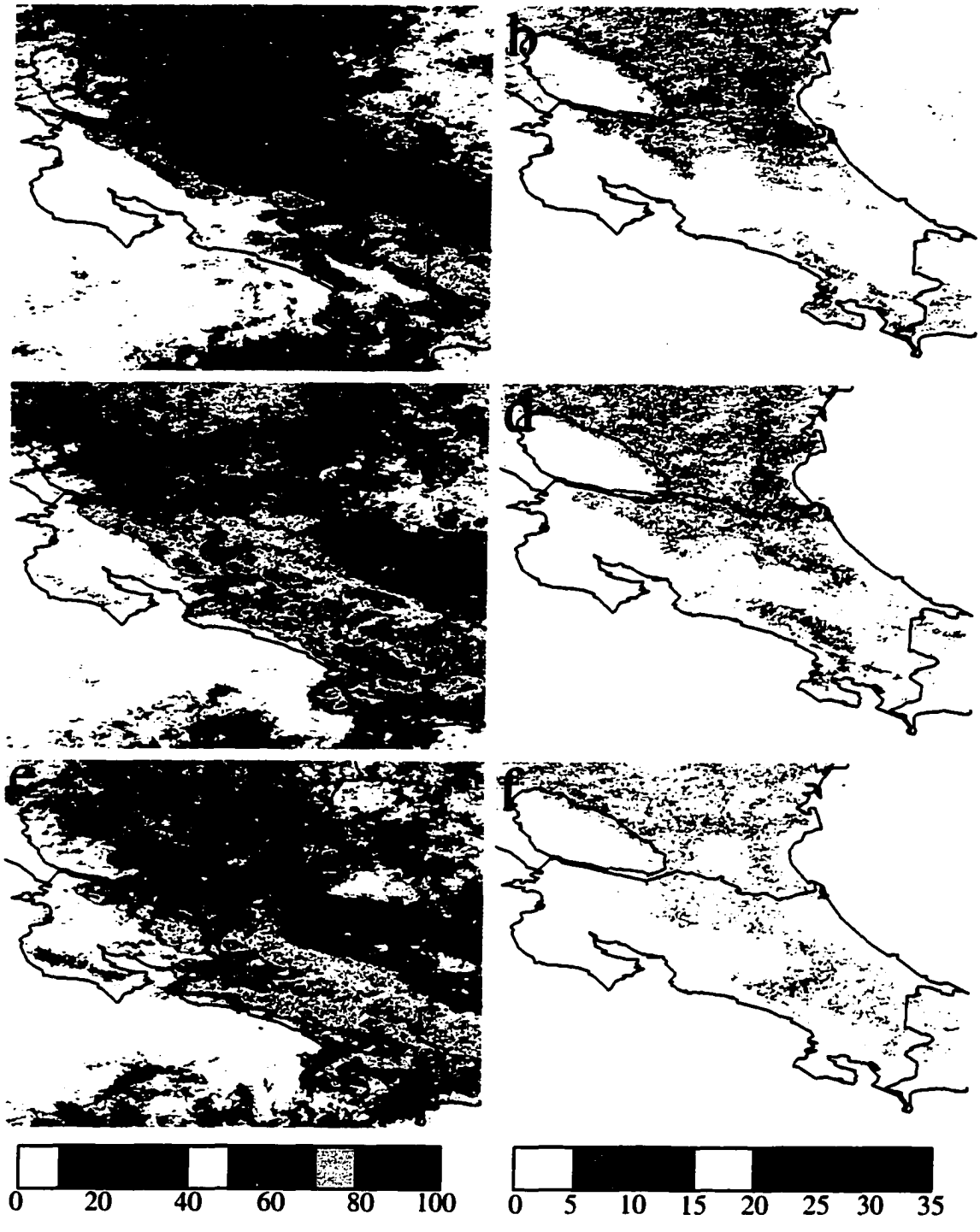

Figure 3.4: Frequency of occurrence of total cloudiness at 1615, 1815, and 2015 UTC are shown in panels a, c, and e. Frequency of occurrence of cumulus clouds at these times are shown in panels b, d, and f.

(upper left corner of each image). This behavior is typical of the cloud clearing that is observed over lakes, bays, and wide rivers (Gibson and Vonder Haar, 1990; Rabin et al, 1990). As seen in Figure 3.4, the area affected is larger than the actual size of the lake, especially in the downwind (left side of the image) direction. This behavior is similar to the flow divergence field downwind of Lake Okeechobee observed by Pielke (1974). Segal et al. (1997) suggested that drying by dynamically induced subsidence and suppression of the convective boundary layer over lakes contribute to the cloud clearing.

Extensive cumulus cloud cover (Figure 3.4, right panels) is found along the Mosquito Coast (in NE Nicaragua, not shown) and extending down to the border with Costa Rica. These regions are predominately forested. Note the rather abrupt decrease in cumulus cloud cover near the Nicaragua-Costa Rica border. The highest frequency of occurrence of cumulus cloudiness occurs at 1615 UTC and then decreases throughout the day. This behavior is due to the fact that moisture is available in the morning hours to initiate cumulus cloud formation. Heating then dries out the boundary layer so that cumulus cloudiness decreases later in the day. Figure 3.4 (left panels) also shows total cloudiness. In southern Nicaragua total cloud cover is maximum about 1815 UTC and then decreases. Heating causes strong convection so that larger clouds form at this time. However, the drying of the atmosphere once again leads to a lower cloud cover later in the day.

Figure 3.4 shows that cumulus cloudiness in Costa Rica is much lower than in neighboring Nicaragua. Furthermore, the cumulus cloudiness is correlated well with the presence of forests, as seen by comparing Figures 3.2, 3.3, and 3.4. Cumulus cloudiness is maximum in the Caribbean lowlands of Costa Rica at about 1815 UTC and then

decreases rapidly. Of particular interest are the two deforested patches (denoted as SC and T in the LANDSAT image, Figure 3.2) to the east of Monteverde in the Muelle San Carlos-Fortuna area. The region T is closer to the ocean and has a higher frequency of occurrence of cumulus clouds. As seen on the LANDSAT imagery (Figure 3.2), cumulus clouds in the deforested regions generally have smaller diameters. The frequency of occurrence of cumulus clouds is higher over forested regions, except in regions of significant topography. On the other hand, total cloud cover in Costa Rica is strongly correlated with topography, as seen by comparing Figure 3.4 with Figure 3.3b. Regions of rapid elevation change cause uplifting which is conducive to total cloudiness but not cumulus cloud development. The maximum total cloud cover occurs at 1815 UTC.

February through April constitutes the height of the dry season in Costa Rica. Therefore, maps of both total cloud cover and cumulus cloud cover for February and April (similar to Figure 3.4) have been developed (not shown). Cumulus cloud fields in February and April are very similar to those in March. Again, there is a strong decrease in cumulus cloudiness near the Nicaragua – Costa Rica border, as well as significant decreases in cumulus cloudiness in the deforested regions. And, the maximum cumulus cloudiness occurs at 1815 UTC for all three months. On the other hand, total cloudiness is larger in both February and April than in March, especially in southern Nicaragua and along the Cordillera de Tilarán mountains. In both February and April, total cloud cover is maximum at 2015 UTC in the Cordillera de Tilarán region.

One other interesting feature is that both the Atlantic and Pacific oceans are nearly free of cumulus clouds during all three months. Total cloud cover over the Caribbean and Pacific oceans is significantly higher in both February and April than in March.

A second question is to what degree are the results for 1999 representative of the region? To answer this question, similar maps of cumulus and total cloudiness have been developed for February through April 2000, and for February 2001. The results show that while there are variations over specific locations, the overall pattern is consistent with the results for 1999. In 2000, the cumulus cloudiness was somewhat higher over Nicaragua for all three months, but total cloudiness is similar. The results for February 2001 are again consistent with those for 1999 and 2000. Therefore, we conclude that the results shown in Figure 3.4 are representative for the region.

3.4.2 Numerical Modeling Experiments

Six soundings are used for initializing the model, as detailed in Section 3.2; a representative sounding is shown in Figure 3.1. In each case the model is initialized at 1200 UTC and run for a total of 12 hours for both forest (designated as *F*1 to *F*6) and pasture (*P*1 to *P*6) simulations. Using these results, the diurnal patterns of cumulus clouds in these two environments are compared in order to assess the effect of deforestation on cumulus cloud formation and development. In the simulations shown below it is assumed that the entire region is either pure forest or pure pasture. The results shown in Figure 3.5 are at 1615 UTC, corresponding to the time of the LANDSAT overpasses (Figure 3.2) and to the top frame of GOES images shown in Figure 3.4. Note that there is a strong tendency to form cloud streets in the forest simulations, similar to that seen in the LANDSAT image (Figure 3.2b). The majority of the simulations show transition from organized cumulus cloud streets to unorganized convection when the surface vegetation type is changed from forest (evergreen broadleaf) to pasture (short

grass). This change in cloud field organization is caused by differences in sensible heat flux. Horizontal convective roll circulations, which are responsible for the formation of cloud streets, are caused by thermal and/or dynamic instabilities (Weckerth et al., 1997).

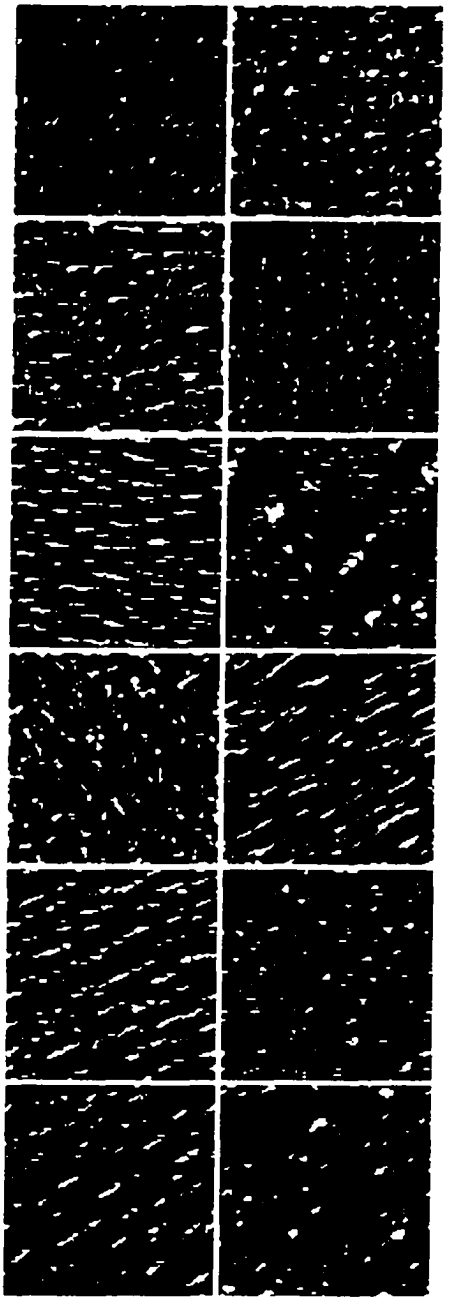

Figure 3.5: Simulated cloud fields at 1615 UTC from simulations *F*1-*F*6 and *P*1-*P*6 are shown in panels a-f and g-l.

Typically, one utilizes non-dimensional numbers that combine the thermal and dynamic instabilities to characterize environments favorable for the formation of horizontal convective roll circulations. One such non-dimensional number is the ratio u_*/w_*. The friction velocity u_* and the free-convection scaling velocity w_* are given by:

$$u^* = [\overline{u'w'}_s^2 + \overline{v'w'}_s^2]^{\frac{1}{4}},$$

$$w^* = \left[\frac{gz_i}{\overline{\theta_v}}\overline{w'\theta'_v}_s\right]^{\frac{1}{3}},$$

where $\overline{u'w'}_s$ and $\overline{v'w'}_s$ are the mean surface momentum fluxes, $\overline{w'\theta'_v}_s$ is the mean surface buoyancy flux, g is the acceleration due to gravity, z_i is the depth of convective boundary layer, and $\overline{\theta_v}$ is the mean virtual potential temperature.

The u_*/w_* ratios for the various simulations in this study are shown in Table 3.2. Note that the u_*/w_* ratio is larger for the forest simulations compared to the pasture simulations. Sykes and Henn (1989) suggested that environments with $u_*/w_* > 0.35$ are favorable for the formation of convective rolls. Notice in Table 3.2 that the u_*/w_* ratio is greater than the threshold value suggested by Sykes and Henn (1989) for the forest simulations, while for pasture simulations this ratio is less than 0.35. The lower surface sensible heat flux for forest allows the existence of two-dimensional laminar flow necessary for the sustenance of cloud streets. However, when the surface is changed to a

pasture, the enhancement in sensible heat flux makes the flow more turbulent, impeding the organization of clouds into streets.

However simulation pairs *F*1, *P*1 and *F*4, *P*4 do not confirm to the cloud organization above pattern followed by the other simulations. The u_*/w_* ratio suggests that *F*1 and *F*4 simulations have environments favorable for the formation of cloud streets while *P*1 and *P*4 should favor unorganized convection. The expected linear organization of clouds is not present for the *F*1 simulation. This could be due to the inability of the model to resolve cloud streets with narrow spacing, since cloud street spacing is dependent upon boundary layer depth, which is relatively shallow for *F*1 simulation. The model simulations *F*4 and *P*4 show different pattern in which cloud organization occurs for the pasture case and not for the forest surface type. Additional study is needed to understand the reasons for this behavior.

n	Simulation *Fn*	Simulation *Pn*
1	0.93	0.26
2	0.41	0.16
3	0.93	0.26
4	0.65	0.25
5	0.83	0.31
6	0.90	0.25

Table 3.2: u_*/w_* values for simulations *F*1-*F*6 and *P*1-*P*6 at 1615 UTC.

Figure 3.6 shows the variation in domain-averaged cloud base height for each of the pasture and forest simulations. In all cases cloud base height shows a tendency to increase throughout the day. At 1600 UTC the average cloud base heights for the pasture simulations (*P*1-*P*6) are consistently higher than those of the forest simulations (*F*1-*F*6). While the different soundings produce different patterns of cloud base height growth

during the day, the pasture simulations typically are several hundred meters higher. Taking the mean of domain-average of cloud base height for the six simulations (Figure 3.7a), cloud base height at 1600 UTC is 776 m for the forest simulations, compared to

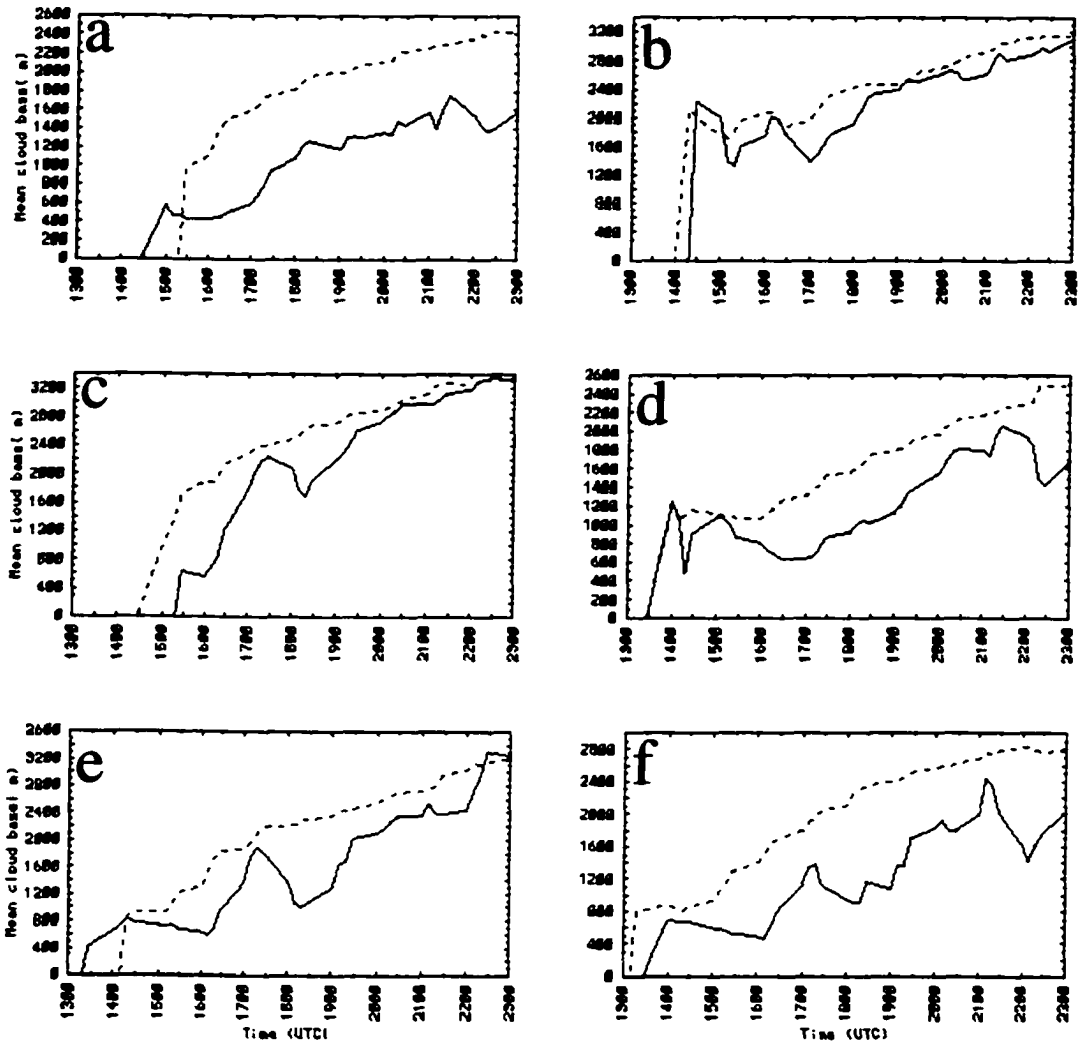

Figure 3.6: Comparison of diurnal variation of domain-averaged cloud base height for simulations: a) *P*1, *F*1 b) *P*2, *F*2 c) *P*3, *F*3 d) *P*4, *F*4 e) *P*5, *F*5 and f) *P*6, *F*6. The cloud base heights from forest simulations are shown as solid lines and those from pasture simulations as dashed lines.

1473 m for pasture simulations. Cloud base height values were estimated from LANDSAT MSS imagery for 23 March 1985 at approximately the same time of day. The results were obtained by matching cloud edges with cloud shadow edges using the

technique of Berendes et al. (1992). Cloud base heights (not shown here) are found to be log normally distributed with a mean cloud base height of 736 m. Values ranged from a low of about 576 m near the coast to values as high as 1099 m along the mountain slopes. A set of four other LANDSAT TM scenes was similarly analyzed, and a similar range of cloud base heights was found. The fact that the LANDSAT results and the simulations

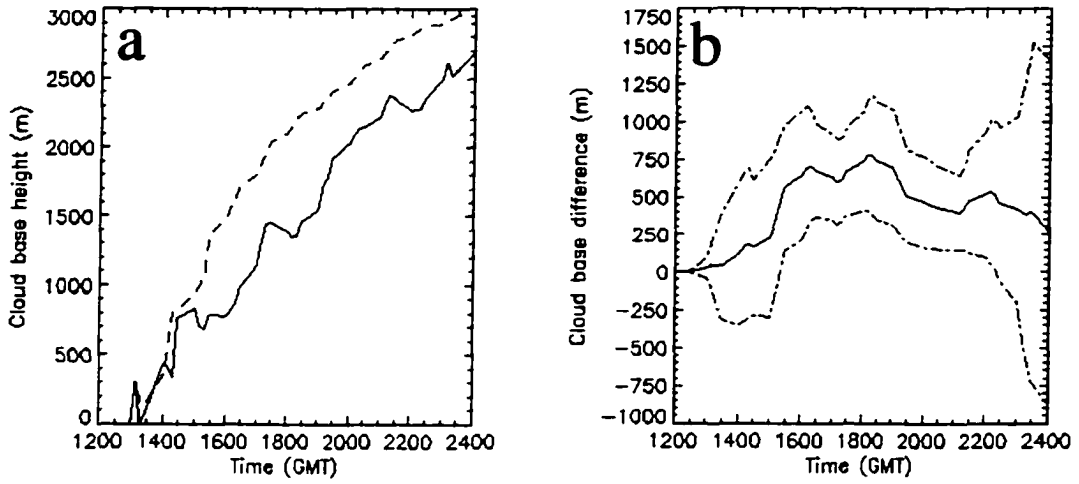

Figure 3.7: a) Mean domain-averaged cloud base height for six pasture and forest simulations. The mean cloud base height for forest simulations is shown using a solid line and for pasture using a dashed line. b) The mean of difference in domain-averaged cloud base height between six pasture and forest simulations. The dash-dot lines show the 95% confidence curves, and the zero difference line is shown using the dashed line.

produce similar results is corroborating evidence that the simulations are realistic.

The mean difference in domain-averaged cloud base height between the six forest and pasture simulations as a function of time is shown in Figure 3.7b. The dashed lines show the 95% confidence intervals. The mean cloud base height differences (pasture – forest) deviate significantly at about 1600 UTC and then persist throughout the day. Maximum differences of about 800 m occur at about 1830 UTC.

There are no significant differences in domain-averaged cloud top height for the forest and pasture simulations (not shown). However, like cloud base height, cloud top

height increases rapidly until about 1800 UTC, reaching mean domain-averaged values of about 2500 m. Then the increase in cloud top height slows and becomes asymptotic at a mean domain-averaged value of about 3200 m at 2000 UTC.

Cloud thickness is derived from the difference between cloud top height and cloud base height. Cloud thickness increases rapidly in both forest and pasture simulations until about 1600 UTC. At this time the mean domain-averaged cloud thickness values for the six forest simulations reach a value of about 750 m and then level off temporarily before decreasing slowly during the remainder of the day. Cloud thickness increases rapidly to mean domain-averaged values of 1500 m for the pasture simulations at 1700 UTC, decreasing to values of about 1100 m at 1800 UTC and then decreasing slowly during the remainder of the day.

There is considerable variation in maximum cloud cover amounts in the various simulations. Maximum cloud cover amounts for the various simulations range from a low of about 6% to a high of about 23%, but there are no consistent patterns. On the other hand, simulations showing high values of cloud cover for the forest cases similarly have high values for the pasture cases, and simulations showing low values of cloud cover for the forest cases have low values for the pasture cases. The mean cloud cover for six forest and pasture simulations show a maximum of approximately 8% in the late afternoon. The mean differences in cloud cover for the forest and pasture simulations are limited to less than 2% until 2000 UTC. Then the mean cloud cover for the pasture simulations becomes about 4% larger than those for the forest simulations. This behavior is due to the fact that the maximum in mean cloud cover for the forest simulations peaks at about 1930

UTC and then decrease rapidly while the pasture simulations peak at about 2100 UTC and then decrease quickly.

The numerical modeling simulations of cloud fields over pasture do not show suppression of cumulus to the same extent as observed over deforested regions in GOES and LANDSAT imagery. The timing of initiation of convection is not significantly different for the pasture and forest simulations. However, note that the same soundings are used to prescribe the atmospheric structure in the simulations, whereas the actual boundary layer profile over forest and pasture will be different, with the boundary layer tending to be drier over pasture. In particular, the Convective Inhibition (CIN) for the atmospheric profile over pasture areas is expected to be higher than over forested regions. In order to resolve issues concerning the timing of convection over forested and deforested areas, specific profiles over these regions are needed.

On average, the cloud liquid water content is slightly higher for the six pasture simulations until 1615 UTC. After this time, the mean domain-averaged cloud liquid water content is slightly lower for the pasture cases. However the magnitude of the mean difference of cloud liquid water content is relatively small. The maximum mean difference during the early stages of cloud field development is about 0.16 g kg^{-2}, whereas the differences between cloud liquid water contents between 1630 UTC and 2215 UTC are less than 0.1 g kg^{-1}. An analysis of the 95% confidence curves indicates that the small differences in mean cloud liquid water contents between the pasture and forest simulations are not statistically significant. This is due to the high variability in the liquid water content difference between forest and pasture simulation pairs. Out of the six pair of simulations, three forest and pasture pairs show extended periods in which the

forest simulations has consistently higher liquid water content. The others show a fluctuating behavior in which at times the forest simulations display higher liquid water content and opposite trend at other times.

The mean domain-averaged liquid water path for the forest simulations is larger than for the pasture cases after about 1600 UTC. But once again, the differences are not statistically significant at the 95% confidence level. At the first glance, the low statistical significance of differences in liquid water path between forest and pasture simulations appears inconsistent with statistically significant differences in cloud thickness. However, unlike cloud thickness, which is consistently higher for forest simulations after about 1600 UTC, the differences in liquid water content between the forest and pasture simulations are very variable. The cloud liquid water path, which is liquid water content integrated as a function of height, also shows a similar behavior. Thus, even though the mean domain-averaged liquid water path for the six forest simulations is higher compared to the pasture simulations, the variances associated with the mean differences in domain-averaged values for the six simulation pairs are also high. Therefore it is the large fluctuations in liquid water content that leads to the fact that the differences in liquid water path between forest and pasture simulations are not statistically significant.

Figure 3.8a shows the mean domain-averaged values of sensible heat flux for the pasture and forest simulations. The maximum mean value of sensible heat flux for the pasture simulations is 173 W m^{-2} at 1730 UTC, compared to a maximum value of 91 W m^{-2} at 1900 UTC for the forest simulations. Note that the mean value of sensible heat flux for the pasture simulations is positive for the time period of 1300 to 2245 UTC,

whereas it is positive for the forest simulations only between 1715 to 2145 UTC.

Figure 3.8b shows the mean differences in sensible heat fluxes as a function of time between the pasture and forest simulations. The maximum mean difference in sensible heat flux is 171 W m^{-2} at 1700 UTC. The 95% confidence levels clearly demonstrate that

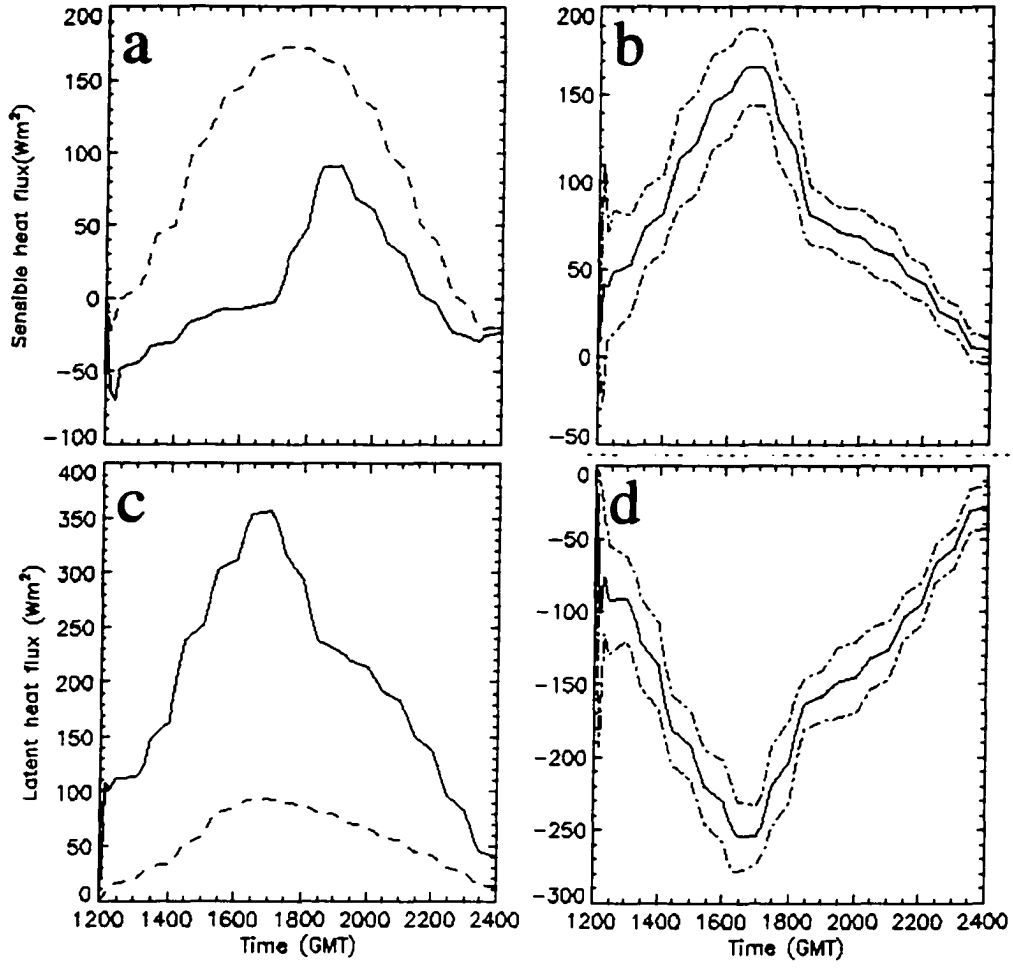

Figure 3.8: a) Mean domain-averaged sensible heat fluxes for six pasture and forest simulations. The sensible heat fluxes for forest simulations are shown as the solid line and for pasture as the dashed line. b) The mean of differences in domain-averaged sensible heat fluxes between six pasture and forest simulations; c) mean domain-averaged latent heat flux for six pasture and forest simulations. The mean latent heat flux for forest simulations is shown as the solid line and for pasture as the dashed line. d) The mean of difference in domain-averaged latent heat flux between six pasture and forest simulations. The dash dot lines in (b) and (d) show the 95% confidence curves, and the zero difference line is shown as the dashed line in (b).

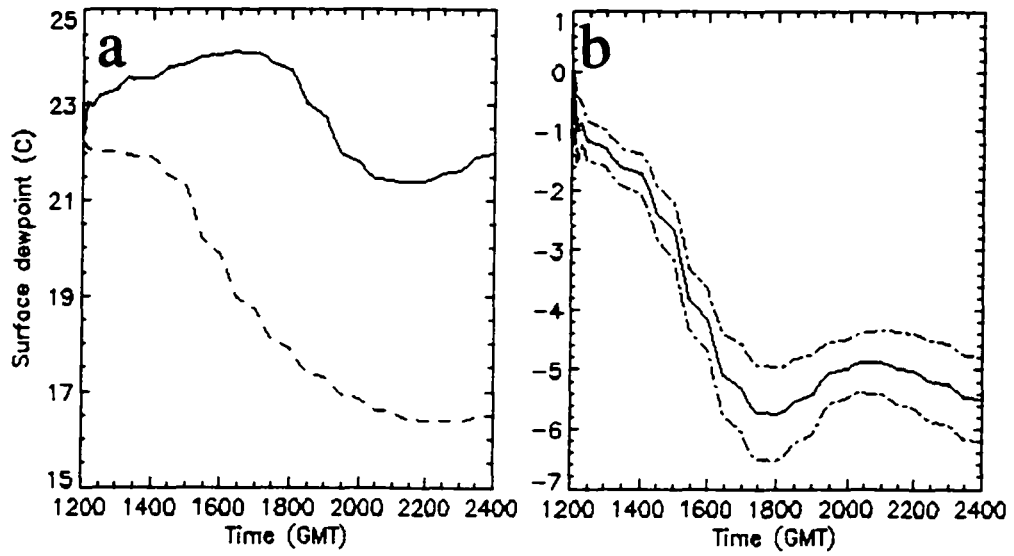

Figure 3.9: a) Mean domain-averaged surface air temperature for six pasture and forest simulations. The mean surface air temperature for forest simulations is shown using solid line and for pasture using dashed line. b) The mean of difference in domain-averaged surface air temperature between six pasture and forest simulations. The dash dot lines in show the 95% confidence curves and the zero difference line is shown using dashed line.

differences in sensible heat flux between pasture and forest simulations are statistically significant.

The mean domain-averaged values of latent heat fluxes for pasture and forest simulations are shown in Figure 3.8c. The mean latent heat fluxes for both sets of simulations peaks at 1700 UTC, with the maximum values being 356 W m^{-2} for the forests and 93 W m^{-2} for the pastures. The mean difference in the simulations is shown in Figure 3.8d. The maximum difference in latent heat fluxes is 263 W m^{-2} at 1700 UTC. Again, the 95% confidence levels show that these differences between the pasture and forest simulations are highly significant.

Figure 3.9a shows mean domain-averaged values of surface temperature as a function of time for the forest and pasture simulations. The pastures are significantly warmer

throughout the entire time of the simulations. The pattern of diurnal variation of surface air temperature is similar for pastures and forests, but the amplitudes are different. The pastures achieve a maximum mean surface air temperature of 31.5°C at 2130 UTC, while the forests achieve a maximum value of 27.9°C at 2100 UTC. Figure 3.9b examines the diurnal variation of the mean of differences in surface air temperature between pastures and forests as a function of time. The mean differences in surface air temperature increase from approximately 1.5°C at 1300 UTC to a maximum of 4.1°C at 1745 UTC. After 1715 UTC the difference in surface air temperature remains relatively constant through the remainder of the simulation period.

The mean domain-averaged surface dewpoint temperatures for pastures and forests is shown in Figure 3.10a. Forests have the mean surface dewpoint temperature increasing early in the day, reaching a maximum value of 24.1°C at 1645 UTC, then decreasing slightly but remaining relatively constant for the remainder of the day. In contrast, the pastures have surface dewpoint temperatures of about 22°C early in the simulations, but then steadily decreasing for most of the remainder of the simulations, with minimum values of about 16.5°C at 2200 UTC. Figure 3.10b examines the diurnal variation of the mean differences in surface air temperature for the forest and pasture simulations. The mean difference in surface dewpoint temperature decreases steadily from a value of about −1°C (i.e., pasture − forest) at 1200 UTC to a value of −5.8°C at 1815 UTC, and then increasing slightly. The 95% confidence levels indicate that these differences are statistically significant.

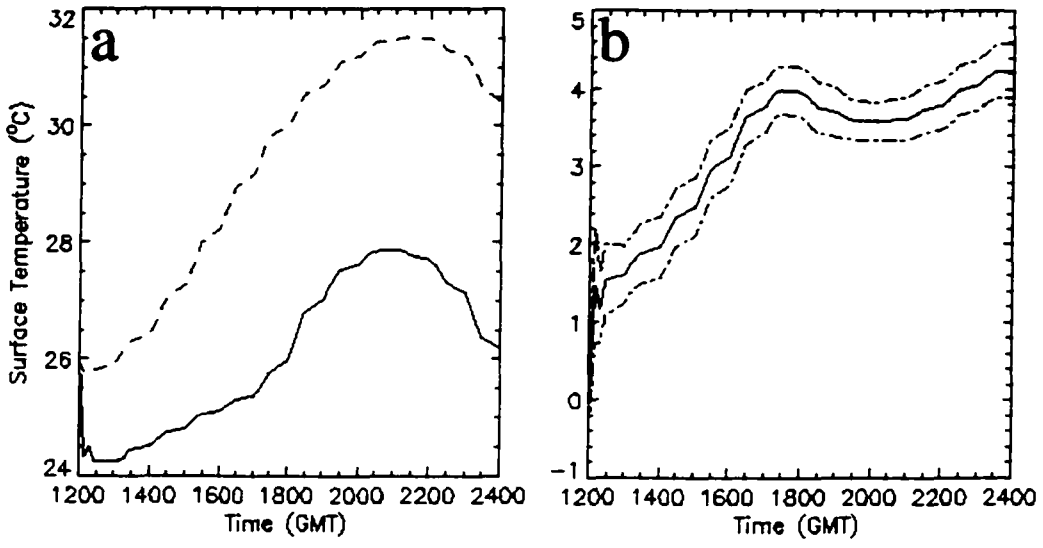

Figure 3.10: a) Mean domain-averaged surface air dewpoint temperature for six pasture and forest simulations. The mean surface air dewpoint temperature for forest simulations is shown using solid line and for pasture using dashed line. b) The mean of difference in domain-averaged surface air dewpoint temperature between six pasture and forest simulations. The dash dot lines show the 95% confidence curves and the zero difference.

3.5 Conclusions

Regional climate change with associated serious ecological implications in the Monteverde cloud forest preserve has been documented by recent studies (Still et al., 1999; Pounds et al., 1999). Since the mid-1970s there has been a reduction in the dry season direct interception of cloud water and wind blown mist, which is the major source of moisture in this region during the dry season. The reduction of dry season moisture affects the local hydrology and could be responsible for population crashes observed in this region (Pounds et al., 1999). It has been suggested that the reduction in dry season moisture input due to increased cloud base heights results from elevated sea surface temperatures (Still et al., 1999; Pounds et al., 1999). In this study we provide the

alternative hypothesis that deforestation alters surface energy budget in ways that influence the development of Costa Rican dry season cumulus cloud fields and orographic cloud fields.

The frequency of occurrence of cumulus cloud fields for the dry season months of February, March and April over the Costa Rican region was derived from 1 km resolution channel 1 GOES 8 imagery. The spatial maps of frequency of occurrence of cumulus cloudiness were compared against spatial maps of recent estimates of forest cover in the Costa Rican region. A pattern of suppression of late morning cumulus cloudiness was observed over areas of deforestation. The comparison also suggests that the degree of suppression of cumulus cloudiness vary, depending on the amount of deforestation, with the suppression being strongest for the most deforested area. Cumulus cloud formation is strongly influenced by the surface through modification of the surface energy budget. Thus the suppression of cumulus cloudiness over the deforested areas is a signal of the influence of deforestation on the regional climate. It should be noted that the current observations of suppression of cumulus clouds over deforested areas are in contradiction to prior studies showing enhanced cumulus cloudiness over deforested areas (Rabin et al., 1990; Lyons et al., 1993; Cutrim et al., 1995).

The RAMS model is used to simulate cumulus cloud fields over forested and deforested (pasture) surfaces. The simulations show consistent and statistically significant differences in cloud base height between forest and pasture simulations. The mean cloud base height for the pasture simulations are consistently higher compared to forest simulations, with a maximum mean difference of 856 m at 1830 UTC. On the other hand differences in cloud top heights between the pasture and forest simulations are not

statistically significant. There is a statistically significant difference in cloud thickness between the forest and pasture simulations, with thicker clouds in the forest simulations. On average the clouds in the forest simulations were approximately 550 m thicker than the ones in pasture simulations.

Differences in cloud cover between the pasture and forest simulations are not statistically significant and nor are differences in cloud water mixing ratio and liquid water path.

The surface sensible heat fluxes are larger for pasture simulations than for forests. On the other hand, latent heat fluxes over the forest surface are much larger. Surface air temperature is consistently higher for pasture simulations compared to forest simulations, while surface dewpoint temperature is consistently higher for forest simulations. Warmer and drier air is found over pastures compared to forests, resulting in the formation of higher and thinner cumulus clouds.

The change in lowland cumulus cloud base heights may affect the moisture input at the Monteverde cloud forest, since a large part of the moisture input is from cloud advection. Since the air masses in the lowland regions are ultimately responsible for the formation of orographic clouds, it is suggested that modification of the lowland air masses from deforestation alters the base heights of the orographic cloud banks at Monteverde. The primary difference between free convective cumulus and the stratocumulus bank is the lifting mechanism. Processes affecting the boundary layer will influence formation and development of both cloud types. The warming and drying of boundary layer air in the lowland regions could thus increase the cloud base heights of the orographic cloud banks.

The main conclusions from this study can be summarized as follows:

1. Satellite imagery shows a pattern of suppression of cumulus cloud formation over deforested regions. The degree of suppression appears to be associated with the extent of deforestation. Cloud suppression over deforested regions is strongest during the month of March, the peak of the dry season. Satellite imagery also shows that the deforested regions show development of clouds during the later hours of the day.

2. Numerical modeling experiments show statistically significant differences in cloud base height and cloud thickness between cloud fields forming over forest and pasture surfaces. On average the clouds have lower base heights and are thicker over forest surfaces. Differences in cloud top heights between forest and pasture simulations are not statistically different.

3. For the same initial atmospheric conditions, differences in cloud cover between forest and pasture simulations are only statistically significant during the later hours of the day. The pasture and forest simulations do not differ significantly in cloud water mixing ratio and cloud liquid water paths.

4. The pasture simulations show enhanced sensible heat fluxes compared to forest simulations, while the latent heat fluxes for forest simulations are higher. This results in drier and warmer air over pasture surfaces, producing elevated and thinner clouds.

5. Modification of boundary layer air over deforested lowland regions could lead to elevation of the base of orographic cloud banks.

Golaz et al. (2001) performed a large eddy simulation study of the sensitivity of cumulus clouds to soil moisture over the Atmospheric Radiation Measurement (ARM) site in Oklahoma. They found results consistent with the present study, namely increased cloud base heights and decreased cloud thickness associated with decreased soil moisture, while cloud top heights and liquid water contents remain relatively unchanged. They also found lower mean liquid water paths associated with decreased soil moisture. The current study found lower values of mean liquid water path for the six pasture simulations compared to their forest counterparts. However, even though the mean values of liquid water path are lower for decreased values of soil moisture, the current study demonstrates that the statistical significance of such differences to be low.

The elevation of cloud base height resulting from lowland deforestation could have serious implications to tropical montane cloud forest all over the world. Changes in local hydrology resulting from deforestation have already been documented (Meher-Homji, 1991), and shifts in regional climate in tropical montane settings can have serious impacts on local ecology (Pounds et al., 1999). Systematic measurements of cloud base heights and field experiments to observe the atmospheric and land-surface variables over forested and deforested areas are required to better understand the regional climate changes occurring in this region.

Chapter 4

Impact of Land Use on Costa Rican Tropical Montane Cloud Forests: Sensitivity of Orographic Cloud Formation to Lowland Deforestation

4.1 Introduction

Tropical montane cloud forests (TMCFs), which are characterized by persistent, frequent or seasonal cloud cover at vegetation level, are biologically rich and diverse as well as one of the most threatened ecosystems in the world (Hamilton et al., 1993; Doumenge et al., 1993). Although cloud forests provide habitats for many of the endangered species most TMCFs are in regions (Myers et al., 2000) where large stocks of diverse endemic species are rapidly losing their habitats. These biodiversity hotspots, occupying approximately 0.4% of Earth's land surface, support about 20% and 16% of Earth's plants and vertebrates, respectively. Of particular concern is that most of these hotspots retain less than 25% of their original primary vegetation covers (Myers et al., 2000).

In addition to the ecologically important function of supporting biodiversity, cloud forests also play important hydrological roles. Tropical montane cloud forests collect a significant amount of moisture by direct interception of liquid water from orographic clouds, advected clouds and wind blown mist. This process is usually termed as horizontal, or occult, precipitation in the literature. Horizontal precipitation can account

for a significant portion of the total precipitation in cloud forests. Data collected from various cloud forest locations around the world show that horizontal precipitation can account for up to 14 – 18 % and 15 - 100% of total precipitation during the wet and dry seasons, respectively (Bruijnzeel and Proctor, 1993). Therefore, destruction of cloud forests could result in decreased stream flows and ground water fluxes (Meher-Homji, 1991). For example, measurements from areas in Sri Lanka, where cloud forests have been converted to tea estates, show decreases in stream flow without accompanied decline in precipitation (Doumenge et al., 1993). Epiphytes such as moss and ferns act like sponges soaking up precipitation during the rainy season and slowly releasing it during the dry season (Still et al., 1999), providing protection against flooding and soil erosion.

One of the TMCF regions that has been a subject of extensive research is the Monteverde cloud forest in Costa Rica (Wheelwright, 2000). This area is host to a very diverse flora and fauna, and sits on the crest of Cordillera de Tilarán, which rises sharply from the lowlands of northwestern Costa Rica. The Cordillera is located at about 125 km from the Caribbean coast. Forest preserve extends from the crest of the Cordillera at 1500 -1800 m down to 700 m on Caribbean and to 1300-1500 m on the Pacific slope. The lower Pacific slope is now deforested. Similar to other cloud forests, horizontal precipitation accounts for a significant amount of the total precipitation in the Monteverde region. On average, horizontal precipitation contributes about 22% of the total annual precipitation in a leeward cloud forest at 1550 m (Clark et al., 2000), but this is significantly higher during the dry season, which extends from February through April. During the dry season, input of moisture from the horizontal precipitation process is

critical, since the ecosystem is under greater physiological water stress than on wet season.

Recent studies have attributed anuran population crashes and longer dry season mist free periods at the lee edge of Monteverde TMCF to an increase in the base height of the orographic cloud bank, resulting from changes in sea surface temperature (Pounds et al., 1999). In global climate model (GCM) simulations of doubled atmospheric carbon dioxide (2 x CO_2), Still et al. (1999) suggest that increased sea surface temperature also intensifies the tropical hydrological cycle. The enhanced latent heat release from intensification of the hydrological cycle warms the atmosphere. Still et al. (1999) and Pounds et al. (1999) suggest that the lifting condensation level rises, and with it the height of orographic cloud banks. However, GCM studies with coarse grid spacing are unable to resolve small-scale terrain features and land-use information. Still et al. (1999) suggest using mesoscale regional models that better resolve the topography and local land-use changes to further explore the impact of climate change on TMCFs.

The trade winds from the Caribbean traverse a distance of approximately 100 km over the Costa Rican lowlands before the slopes of Cordillera de Tilarán lift the air, resulting in the formation of orographic cloud banks. Originally tropical moist and wet forests covered most of the Costa Rican lowlands. However, by 1992, rapid deforestation rates had reduced the forest cover in the Costa Rican lowlands to about 1200 km^2 (18% of the area of original forest cover; Veldkamp et al., 1992).

Nair et al. (2002a) used satellite data to show that cumulus cloud formation is suppressed over deforested areas in the Costa Rican lowlands. Using numerical modeling experiments, it was also shown that conversion of surface vegetation from forest to

pasture resulted in substantial differences in lowland cumulus cloud formation. In addition to differences in cloud field organization, the average cloud base height, cloud thickness, cloud top height, cloud liquid water content and cloud water path all differed when the surface vegetation was changed from forest to pasture. The average cloud base height increased substantially (maximum difference of ~750 m) when the surface characteristics were changed from that consistent with forest to that of a pasture. Nair et al. (2002b) concluded that land-use changes in the Caribbean lowlands can alter the nature of the air masses responsible for the formation of cumulus clouds. They suggested that the formation of orographic cloud could also be affected by deforestation in the Caribbean lowlands.

The main objective for the present study is to use the Colorado State University Regional Atmospheric Modeling System (CSU RAMS), a mesoscale numerical model, to investigate the effects of Costa Rican lowland deforestation on orographic cloud formation along the Caribbean slopes of Cordillera de Tilarán. A brief description of the study area is given in Section 4.2. The data used in this study are described in Section 4.3, while Section 4.4 discusses the methodology. Section 4.5 presents analysis of RAMS simulations, and Section 4.6 concludes.

4.2 Study Area

The area of interest in this study is the northern part of Costa Rica, where the Monteverde cloud forest is situated at the crest of Cordillera de Tilarán (Figure 4.1a,

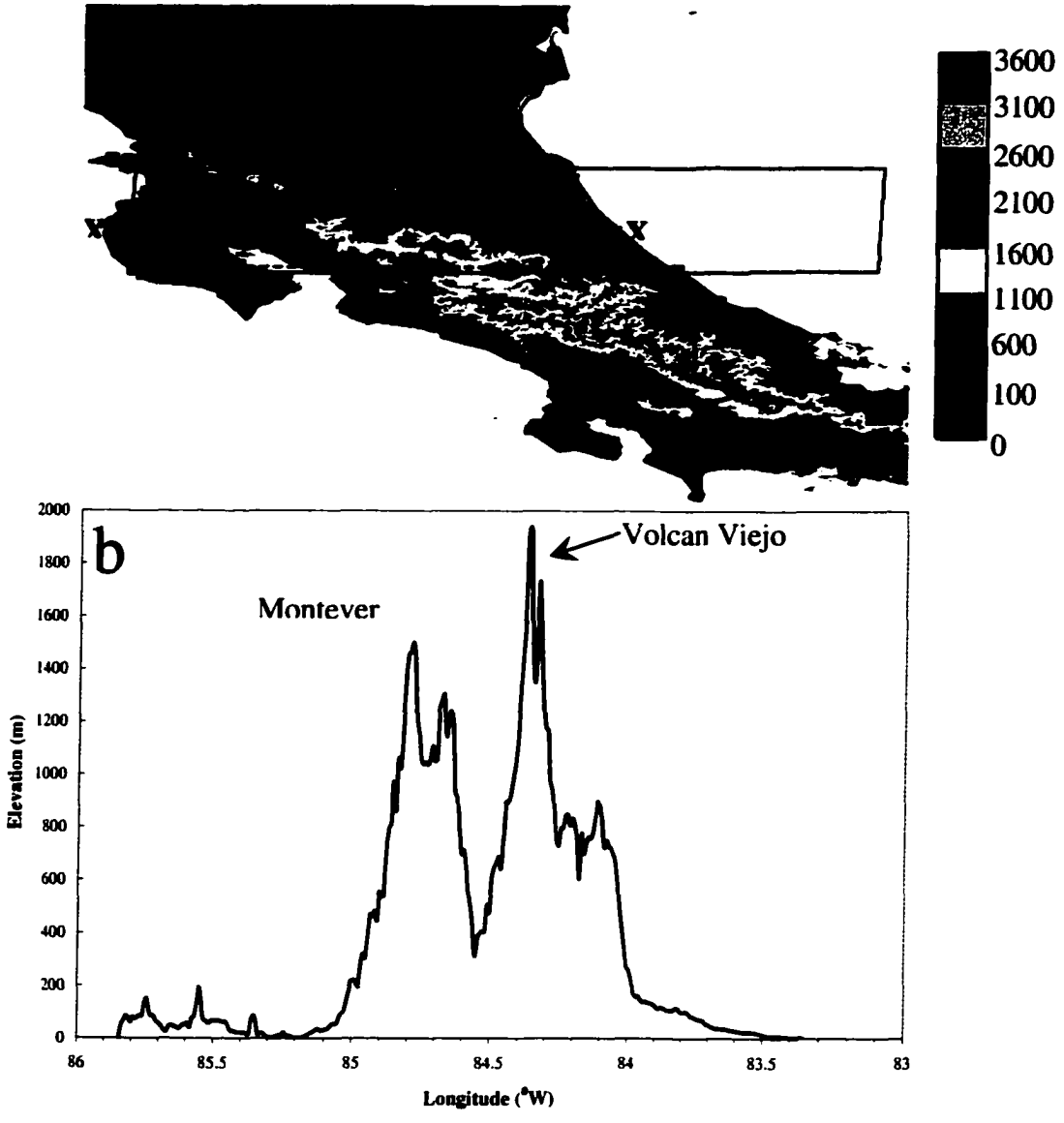

Figure 4.1: a) Topography map of the study area. Marked on the map are locations of San Carlos plains (SC), Tortuguero plains (T) and Cordillera Volcanica Central (CC). The blue rectangle shows the location of the RAMS grid used in this study. The horizontal cross sections of RAMS simulated cloud liquid water content presented in later sections are for the area highlighted in black dashed rectangle. The vertical cross sections of RAMS simulated liquid water content to be discussed in later sections are to be along the portion of the dash-dot line contained within the dashed rectangle; b) Surface elevation in the east-west direction along the dash-dot line XX shown in panel (a).

4.1b). In the Monteverde region, the mountain range rises up to elevations greater than 1800 m (Figure 4.1a). The Cordillera Central to the southeast consists of volcanoes, ranging between 2100 - 3400 m in elevations (Figure 4.1a, 4.1b). The flow of trade winds over these mountains results in the formation of orographic cloud banks along the upper windward slopes. Immersion of forests in clouds along these slopes is responsible for the sustenance of one of the richest cloud forest ecosystems in the world.

The forest cover in the Costa Rican region has been reduced considerably during the past century. The most recent estimate of the forest cover for the Costa Rican region (Wheelright, 2000) is shown in Figure 4.2. Notice that the majority of the lowland areas are deforested, with the exception of some remnant forests south of the Costa Rica-Nicaragua border. The San Carlos and Tortuguero plains to the east of the Monteverde region have a long history of deforestation. However across the border in Nicaragua, the forest cover remains relatively intact.

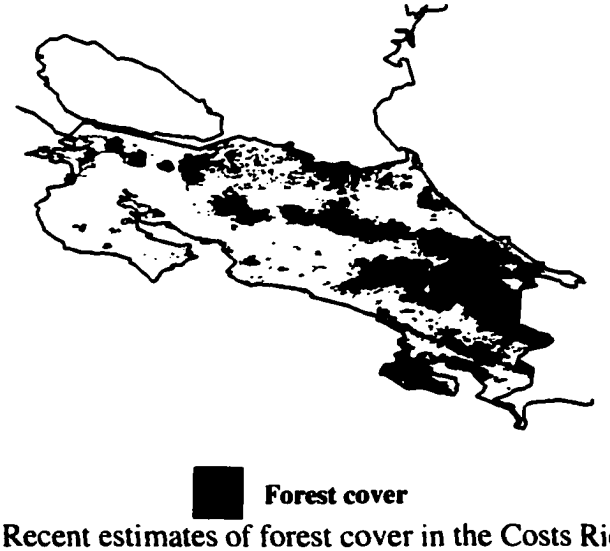

Figure 4.2: Recent estimates of forest cover in the Costs Rican region.

4.3 Data

In the present study, the National Center for Environmental Prediction (NCEP) reanalysis data (Kalnay et al., 1996) for the dry season month of March 1999 is used for initializing and specifying lateral boundary conditions for the RAMS simulations. The NCEP reanalysis data is chosen for days with relatively calm synoptic conditions in northern Costa Rica which also have orographic cloud formation.

The Geostationary Environmental Operational Satellite-8 (GOES-8) imagery is used to determine days of relative calm and good orographic cloud formation and also for comparing the RAMS simulated orographic cloud banks to observations. GOES-8 imagery has five spectral channels, with one in the visible (0.52 – 0.72 μm) and four in the infrared region (3.78-4.03 μm, 6.47-7.02 μm, 10.2-11.2 μm, 11.5-12.5 μm). Spatial resolution at nadir for channel 1 is 1 km, 4 km for channels 2, 4, and 5, and channel 3 has nadir resolution of 8 km. The visible channel is used in the present study. The GOES-8 visible channel imagery over the Costa Rican region at 1615 UTC (10:15 AM local time), for the six days considered in this study are shown in Figure 4.3a - 4.3f. Notice the correlation between the cloud cover in Figure 4.3 and the topography for the region shown in Figure 4.1. Orographic clouds are present over the most significant topographical features, especially the Monteverde region and the chain of volcanoes to the southeast. The convective activity in the Costa Rican lowland, northeast of Monteverde region, is stronger for the last three days (Figure 4.3d, 4.3e, 4.3f) compared to the other days (Figure 4.3a, 4.3b, 4.3c). The extent of orographic cloud cover both over the Monteverde region and the mountain ranges to the south also varies, with higher cloud cover for the last three days.

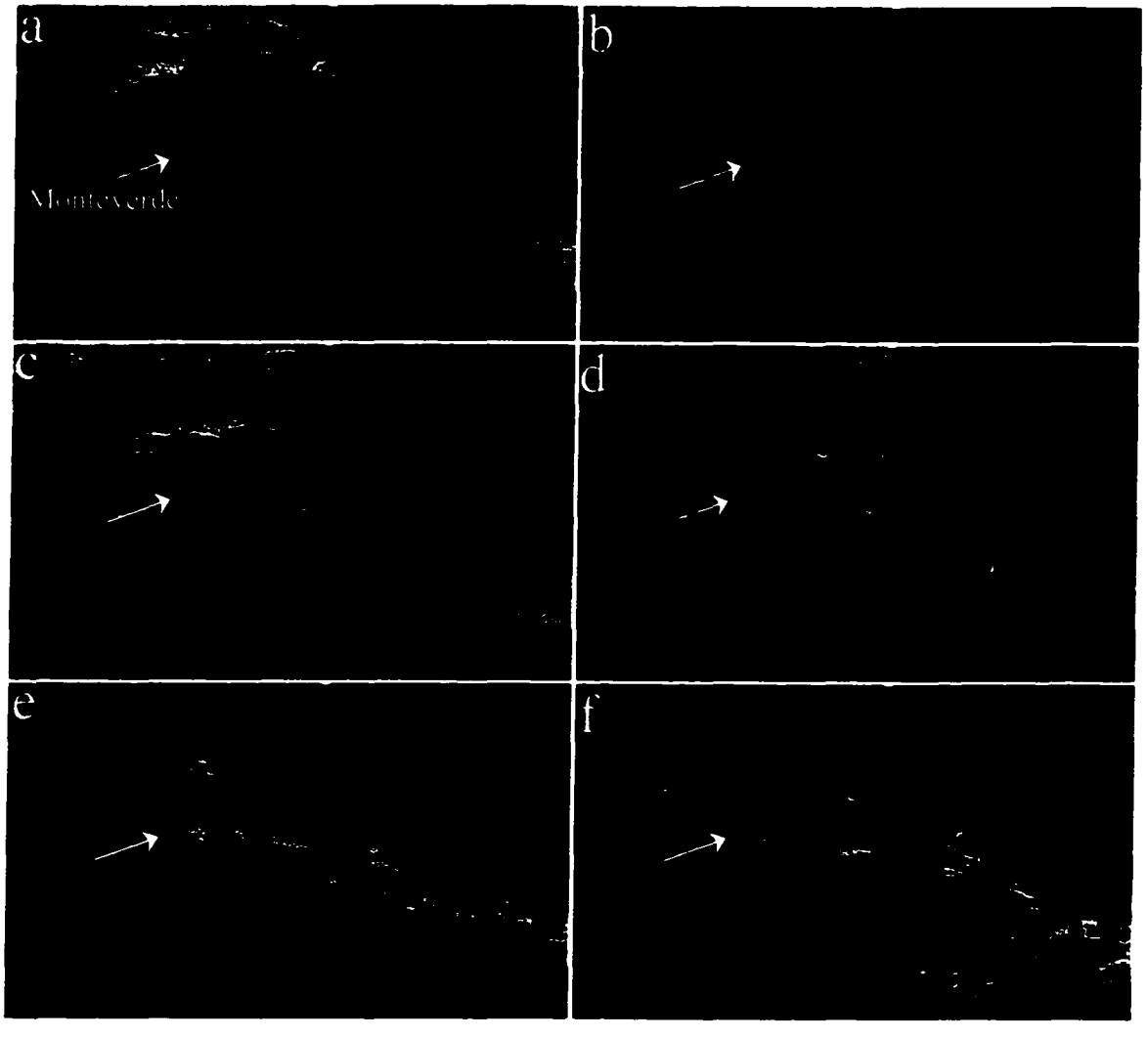

Figure 4.3: The GOES 8 imagery at 1615 UTC for: a) 9 March 1999; b) 19 March 1999; c) 23 March 1999; d) 24 March 1999; e) 27 March 1999; and f) 29 March 1999.

As shown in Chapter 3, Landsat images revealed that cumulus cloud formation was suppressed over the deforested regions of the Costa Rican Caribbean lowlands. This behavior is also evident in Figure 4.3. In each case note that cloud cover is much more prevalent over the northern border. Neighboring Nicaragua remains primarily forested with much higher cloud cover. Other than deforestation (Figure 4.2), there are no

dramatic topographical variations or other discontinuities across this border region to account for abrupt decrease in cloud cover.

Table 4.1 shows the sets of NCEP reanalysis data (N1-N6) used in this study. Also shown in Table 4.1 is the Convective Available Potential Energy (CAPE) and the Lifting Condensation Level (LCL) calculated for atmospheric profile over the eastern coast of the Costa Rican region, interpolated from the NCEP dataset. The CAPE values, an indicator of atmospheric stability, varied from 22 to 798 J kg^{-1}, values consistent with weak to moderate convection. The LCL values, indicative of cloud base height, varied from 210m to maximum of 375 m. However, the CAPE and LCL values obtained from the NCEP reanalysis profiles are slightly lower compared to corresponding values obtained from radiosonde observations for San Andres island (300 km northeast of Costa Rica). The NCEP reanalysis data thus has a more stable atmosphere and higher boundary layer humidity compared to the spatially closest radiosonde observation.

NCEP Data	Date	12 UTC CAPE (J kg^{-1})	12 UTC LFC (m)
*N*1	09 March 1999	22	360
*N*2	19 March 1999	148	351
*N*3	23 March 1999	358	257
*N*4	24 March 1999	594	292
*N*5	27 March 1999	598	375
*N*6	29 March 1999	798	210

Table 4.1: The dates for sets of NCEP reanalysis data used in this study. Analysis at 1200, 1800 UTC for the same day and 0000 UTC of the next day are used in this study.

4.4 Methodology

The CSU RAMS (Pielke et al., 1992), a nonhydrostatic numerical modeling system used for simulating a wide range of atmospheric phenomenon, is used in this study to examine the influence of Costa Rican lowland deforestation on orographic cloud

formation downstream. The RAMS utilizes finite difference approximations to solve conservation equations of mass, momentum, heat, solid and liquid phases of water. The finite difference equations are solved within a grid structure that uses a polar stereographic projection in the horizontal, and a terrain-following Sigma coordinate system in the vertical (Mahrer and Pielke, 1974). The bulk water parameterization accounts for the various cloud processes, while a multi layer soil model (Tremback and Kessler, 1985) and a vegetation model (Avissar and Pielke, 1989) represent the various land-surface processes. The RAMS provides a wide range of ways for representing atmospheric radiative transfer, subgrid-scale turbulence, top and lateral boundary conditions.

As in the sensitivity study discussed in Chapter 3 (Nair et al., 2002b), a coupled design is used to investigate the effect of varied surface conditions on orographic cloud formation. For a similar set of atmospheric conditions initialized using NCEP reanalysis data (*N*1 - *N*6), the orographic cloud formation is simulated using RAMS for the following scenarios. The surface is assumed to be: a) completely forested, b) completely deforested, or c) partially deforested, where the forest cover is specified by the recent estimates given by Wheelright (2000). The vegetation characteristics for the forested and deforested areas are consistent with that of evergreen broadleaf and short grass, respectively. The initial volumetric soil moisture for the forested region is set to 0.4, consistent with dry season evergreen forest values for the region (Dietrich et al., 1982). The deforested regions are assigned volumetric soil moisture value of 0.25, consistent with empirical micrometeorological studies over Amazonian pasture (Bastable et al., 1993).

A grid of 400 x 100 km, centered approximately on the plains east of the Monteverde region (10.39N, 83.9W), was used for the cloud simulations. The simulations utilized a grid spacing of 2 km in the horizontal; and in the vertical a stretched grid was used, with a grid stretch ratio of 1.2 and whose grid spacing varied from 30 m near the surface to 750 m higher up the atmosphere. The heights of first 10 levels are 14, 47, 86, 133, 190, 258, 340, 438, 556, and 697 m, respectively. Surface topography was specified using the United States Geological Survey 1 km dataset. Figure 4.1 shows a contour map of topography for the Costa Rican region, with the outline of the model grid overlaid. Notice that the grid is approximately centered on the western edge of Costa Rican lowlands and extending into the Caribbean, covering the lowland areas to the east of Monteverde and also a considerable fetch of the ocean. The model grid almost extends to coastline in the west Costa Rican region.

The initial atmospheric conditions for RAMS are obtained by interpolation from the NCEP reanalysis data at 1200 UTC. The nudging option is used along the lateral boundaries, where the analysis time series data from the large-scale model are used for specifying the dynamic (velocity) and state variables (temperature, moisture etc.) along the lateral boundary grid points. The time series from NCEP reanalysis, at intervals of 6 hours starting from 1200 UTC, is used in this study (analysis at 1200 UTC, 1800 UTC of the same day and 0000 UTC of the next day). For a particular time step between 1200 and 1800 UTC, the values of dynamic and state variables along the lateral boundary grid points are relaxed towards the values observed at those locations in the analysis available for next time period (1800 UTC NCEP reanalysis data). This is achieved by nudging the current value of a variable at a grid point by an amount proportional to difference

between the current and future values, where the future value is prescribed by the NCEP reanalysis data. Similarly between 1800 and 0000 UTC, the values along the lateral grid points are relaxed towards that observed in 0000 UTC NCEP reanalysis.

The atmospheric radiative transfer scheme of Chen and Cotton (1983) that accounts for the effects of clouds is used in this study. Cloud and precipitation ice processes are not activated since the simulated orographic clouds are generally below the freezing level, which is above approximately 4.5 km for the days considered in this study. The only precipitation forming process activated is that for formation of warm rain. A time step of 6 seconds is used to advance the solutions of the various conservation equations. However the tendencies from the radiative transfer calculations are updated only once every 120 seconds. Details of the CSU RAMS model can be found in Pielke et al. (1992).

4.5 Results

RAMS is initialized using the six sets of 1200 UTC NCEP reanalysis data (*N*1 - *N*6; Table 4.1). The model simulations for various land-use scenarios are then used to examine the characteristics associated with orographic cloud formation for the next 12 hours. Differences in orographic cloud base height, cloud cover, liquid water content are explored. The surface energy fluxes, surface air temperatures and dewpoints for the lowland region also are examined.

4.5.1 Comparison Between Model-Simulated and Satellite-Observed Clouds

In general, the simulations are successful in generating orographic cloud patterns similar in nature to satellite observations. Figure 4a shows the GOES images for 9 March 1999 at 1615 UTC, with the study area superimposed by the rectangular box defined in Figure 4.1. Monteverde, Cordillera Central and the Miravalles regions are indicated.

Figures 4.4 b, c, and d show the results for the completely forested, completely deforested, and partially deforested studies, respectively. Note that orographic cloud forms approximately over the same Monteverde, Cordillera Central, and Miravalles regions as seen in the satellite imagery. However, in all the simulations, the orographic cloud bank over the Cordillera Central region extends further west compared to the satellite observations. Also for all simulations the cloud cover over the Miravalles region is lower than the observations.

Figure 4.4 also shows that the various land-use scenarios lead to different cloud cover distributions. The partial deforestation case (Figure 4.4d) has higher cloud cover (6.3%) than the forest (6%) (Fig 4.4b) and complete deforestation simulations (4.8%) (Figure

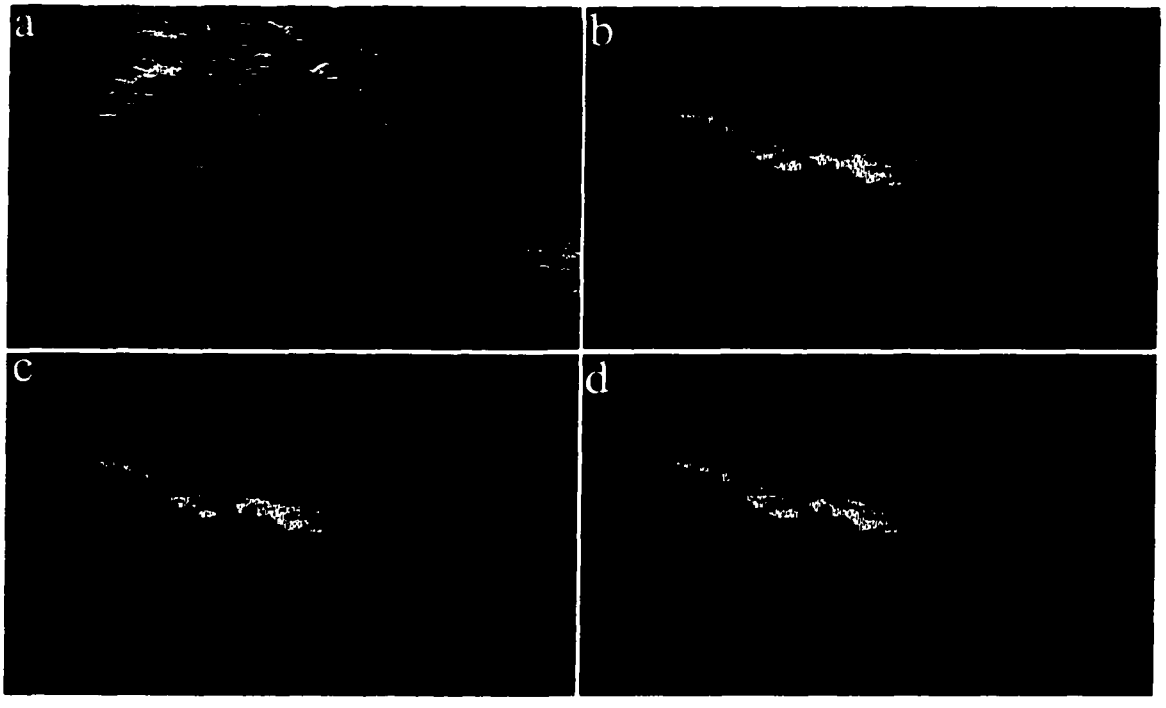

Figure 4.4: Cloud patterns at 1615 UTC for 9 March 1999 for the study area from: a) GOES 8 1 km visible imagery; b) forest simulation; c) deforested simulation; and d) partial deforestation simulation.

4.4c). The slightly higher cloud cover for the partial deforestation simulation mainly derives from the orographic clouds at upper levels extending further out along the Caribbean slopes of the Monteverde, Cordillera Central, and Miravalles regions. However, compared to the other simulations, the forest simulation shows enhanced convection in the Tortuguero plains (Figure 4.1) and also along the Costa Rica - Nicaraguan border region to the north.

4.5.2 Effect of Deforestation on Orographic Cloud Base Height

In this section, the effect of deforestation on the average height at which the orographic cloud bank intersects the mountain ranges is examined (in the region highlighted by the dashed line in Figure 4.1), by inspecting the cloud liquid water in the lowest vertical model level. This level follows the terrain at approximately 14 m above the surface. If cloud liquid water is present at a grid point in the lowest model level, then the orographic cloud is present at the surface. The surface elevation of the grid point is taken to be the orographic cloud base height at that location. For every 15 minutes, the orographic cloud base height thus obtained is averaged for the region highlighted by the dashed rectangle in Figure 4.1. The domain-averaged cloud base heights for this region then are compared for simulations with same initial atmospheric conditions, but varying land use. Also, the differences of domain-averaged cloud base heights for this region are examined between forested and deforested, and between forested and partially deforested (observed forest cover) simulations are examined. The differences in cloud base heights between the simulation pairs are averaged for the six days considered in this study, and the statistical significance of these differences, are examined.

The RAMS simulations show significant differences in the orographic cloud base heights between forested and deforested, forested and partially deforested simulations. Out of the six sets of simulations, all except one show consistent differences in the domain-averaged orographic cloud base height (averaged over the area highlighted by dashed lines in Figure 4.1) throughout most of the day. A representative example for 29 March 1999 is shown in Figure 4.5a. The cloud base height is highest for the complete deforestation case, followed by the partial deforestation case, and is lowest for the forested simulation. Four other simulations show similar patterns, in which the orographic cloud base height is consistently higher for the complete and partial deforestation compared to the forest simulations. A second partial deforestation scenario also has been examined, not shown. In this case the lowland regions below 600 m are completely deforested, while higher regions are completely forested. The results are very similar to those of complete deforestation case shown in Figure 4.5a. The significance of this result is that the increase in orographic cloud base height is due primarily to deforestation in the lowlands rather than by deforestation along the mountain slopes.

The variation of cloud base height for 23 March 1999 is shown in Figure 4.5b. For this anomalous case, the differences in cloud base heights between forested and partially deforested cases are not as consistent as for the other days. Figure 4.3d and Table 4.1 offer no clues why the results are different in this case. Also after about 2000 UTC the differences in cloud base heights between all the scenarios become relatively small. However, the reason for this is behavior not understood at this point and requires further study.

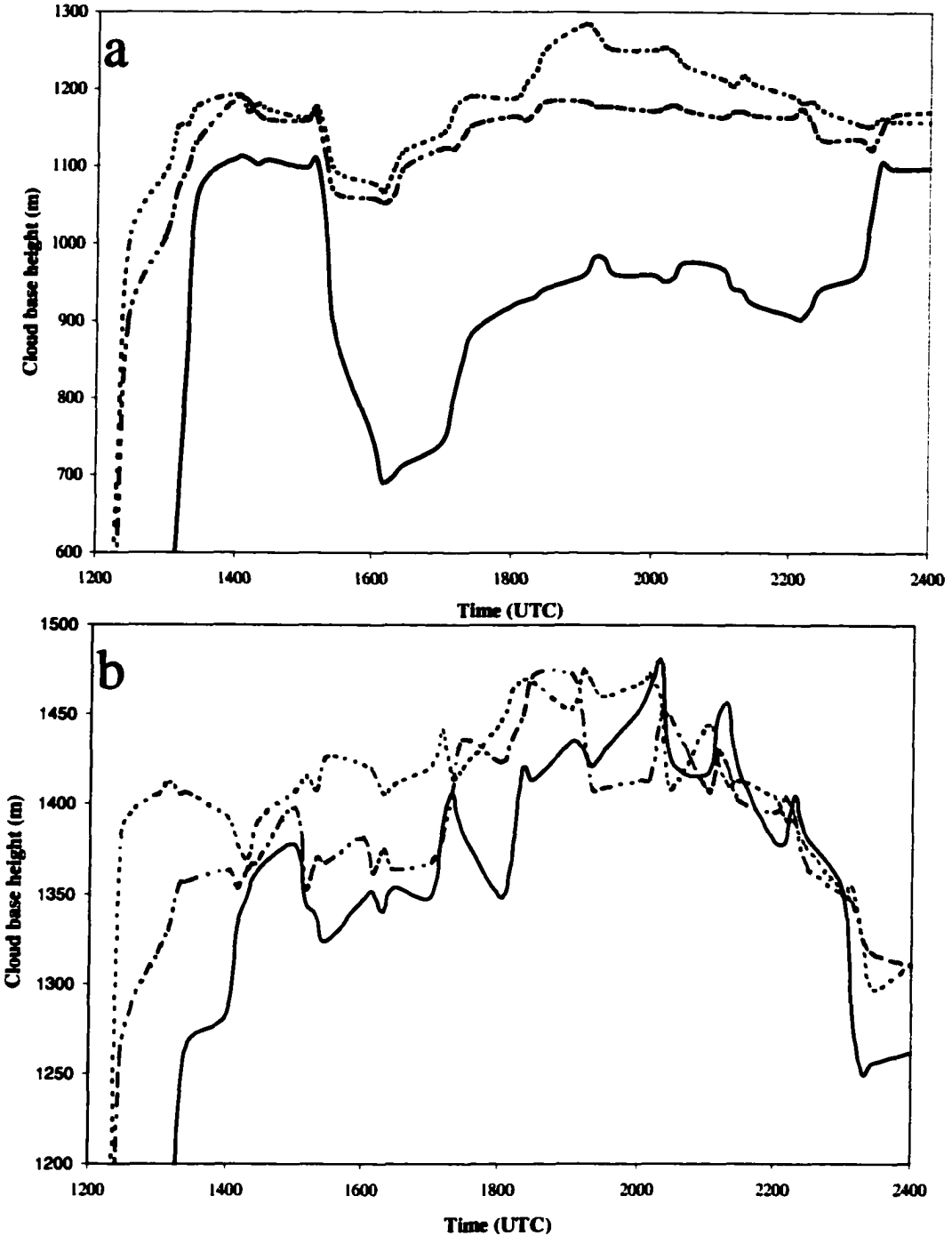

Figure 4.5: The diurnal variation of orographic cloud base height from model simulations for days: a) 29 March 1999; and b) 23 March 1999. The solid, dotted and dash-dot lines are for forested, deforested, and partial deforestation scenarios.

Differences in domain-averaged cloud base heights between forested and deforested simulations, and between forested and partially deforested, are averaged for the six days. The results are shown in Figure 4.6a and Figure 4.6b. On average, the complete deforestation case leads to a cloud base height which is up to 750 m higher at 1230 UTC, but at later times decreasing to values of 200 m and 100 m. Notice that the large differences of up to 750 m in the beginning of the simulation are solely due to the fact that orographic clouds form earlier in the forested case. However, when the clouds are well developed in both of the simulations, the differences reduce to values of about 200 m.

The average difference in cloud base heights between forested and partially deforested simulations shows a pattern very similar to that between forested and completely deforested simulations, where the orographic cloud base is higher for the partially deforested case. During the early hours of the day, the average orographic cloud base for partial deforestation is higher by about 630 m, which decreases to approximately 100 m by 1400 UTC and remains relatively constant until 1900 UTC. Between 1900 UTC and 2300 UTC, the cloud base is still higher for the partial deforestation case, but the difference is smaller. Again notice that the large anomalous differences during the early hours of the simulations are from orographic clouds forming earlier in the forested simulations. Through most of the day, the effect of current forest cover is to increase the elevation of orographic cloud base by about 100 m. The difference in cloud base height between forest and partial deforestation is statistically significant through most of the simulation, except during the time period of approximately 2000 UTC - 2300 UTC.

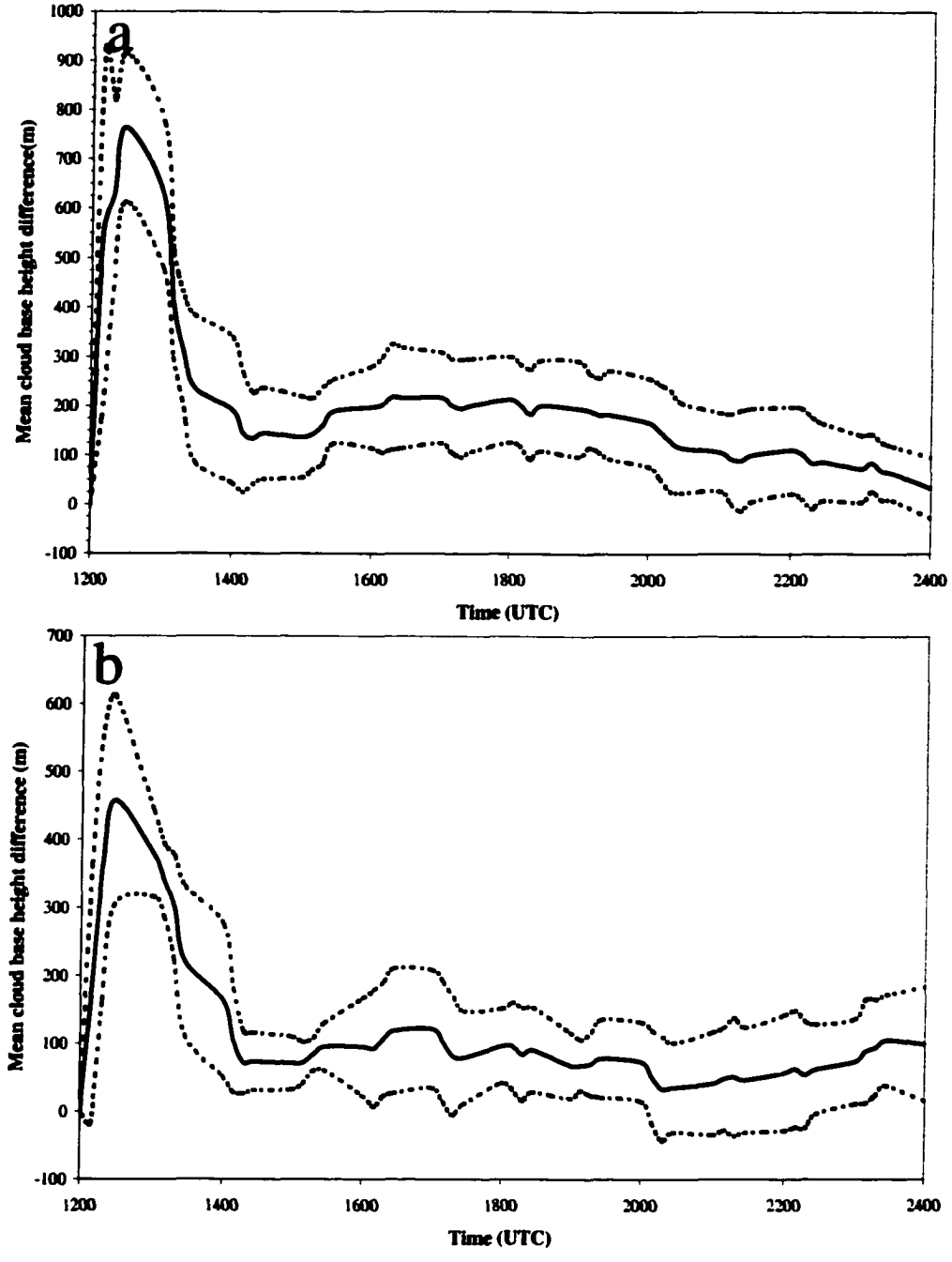

Figure 4.6: The diurnal variation of mean difference in orographic cloud base height between a) deforested and forested; and b) partially deforested and forested simulations. The solid and dotted lines are the mean of difference in cloud base height and 95% confidence envelopes.

The simulated orographic cloud bases depend on the atmospheric conditions with which the model was initialized and the constraining NCEP data used for specifying the lateral boundary. As noted earlier these may result in cooler, more stable and moister conditions than actually occur in the boundary layer. While this might result in simulated cloud bases lower than actual ones, it should not influence the relative relations between forested, partially forested and deforested scenarios.

For the Monteverde region an increase in cloud base height of the magnitude seen in the complete and partial deforestation simulations might have significant impacts on the cloud forest. The increased elevation in cloud base heights in this region would imply 1) reduced area with cloud forest conditions, 2) increased fragmentation of cloud forests, and 3) changes to regional hydrological budgets. For cloud forest organisms these changes might force reductions in population size and/or changes in range. This poses serious risks to these areas of high biodiversity. Thus lowland deforestation may have significant impact on cloud forests located down wind.

4.5.3 Influence of Deforestation on Cloud Cover

For the various land-use scenarios, the diurnal variation of cloud cover over the land areas in the model domain is examined in Figure 4.7. The general pattern of diurnal variation of averaged cloud cover is similar for forested, completely deforested and partially deforested simulations. In each case cloud cover initially increases, reaches a maximum at about 1600 UTC for forested, at 1445 UTC for deforested and at 1500 UTC for the partially deforested cases, and then decreases slightly to a relatively constant value between 1700 and 2100 UTC. For the partially deforested case, there is a small increase in cloud cover after 2100 UTC. However, notice that the magnitude of cloud cover is

different for the various deforestation scenarios. Cloud cover over the region for the forested case is consistently higher than for the deforestation scenario. The average difference in cloud cover between forested and completely deforested simulations is approximately 3.4%, and analysis shows that the differences are statistically significant through most of the simulations. As expected, the cloud cover for the partially deforested case is greater than that for the completely deforested case, but it is lower than the forested case. The difference in cloud cover between the forested and partially deforested

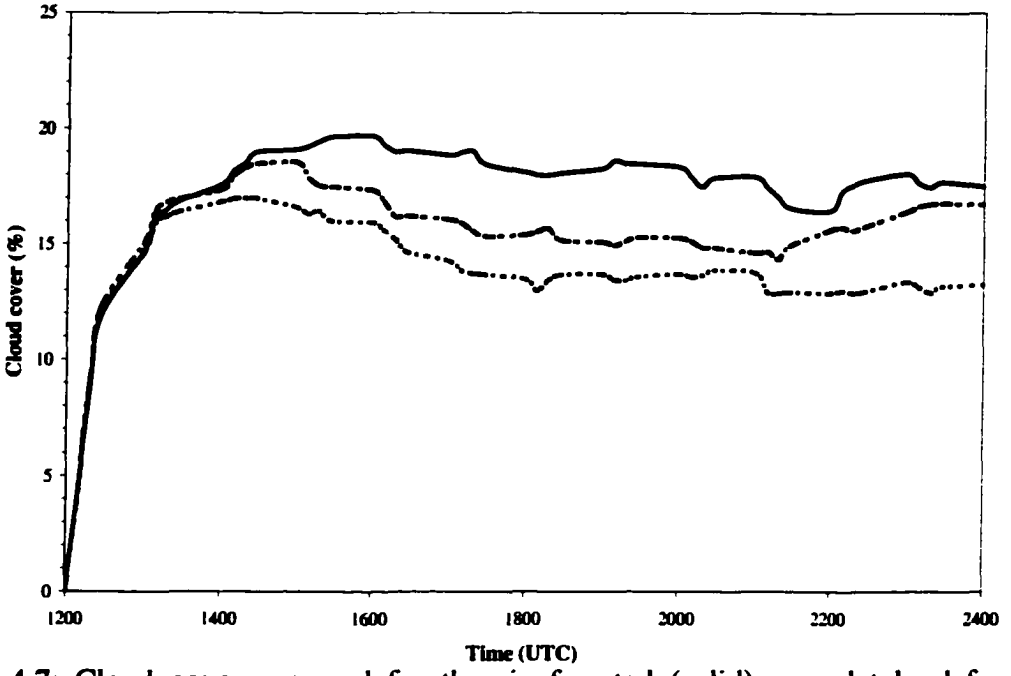

Figure 4.7: Cloud cover averaged for the six forested (solid), completely deforested (dotted) and partially deforested (dash-dot) simulations.

case averages about 1.7%. The differences, however, are statistically significant only between 1500 and 2100 UTC.

4.5.4 Distribution of Orographic Clouds at the Surface

Figure 4.8 shows the contour plots of liquid water at the lowest model level (following the terrain at 14 m) in the region highlighted by the dashed rectangle on

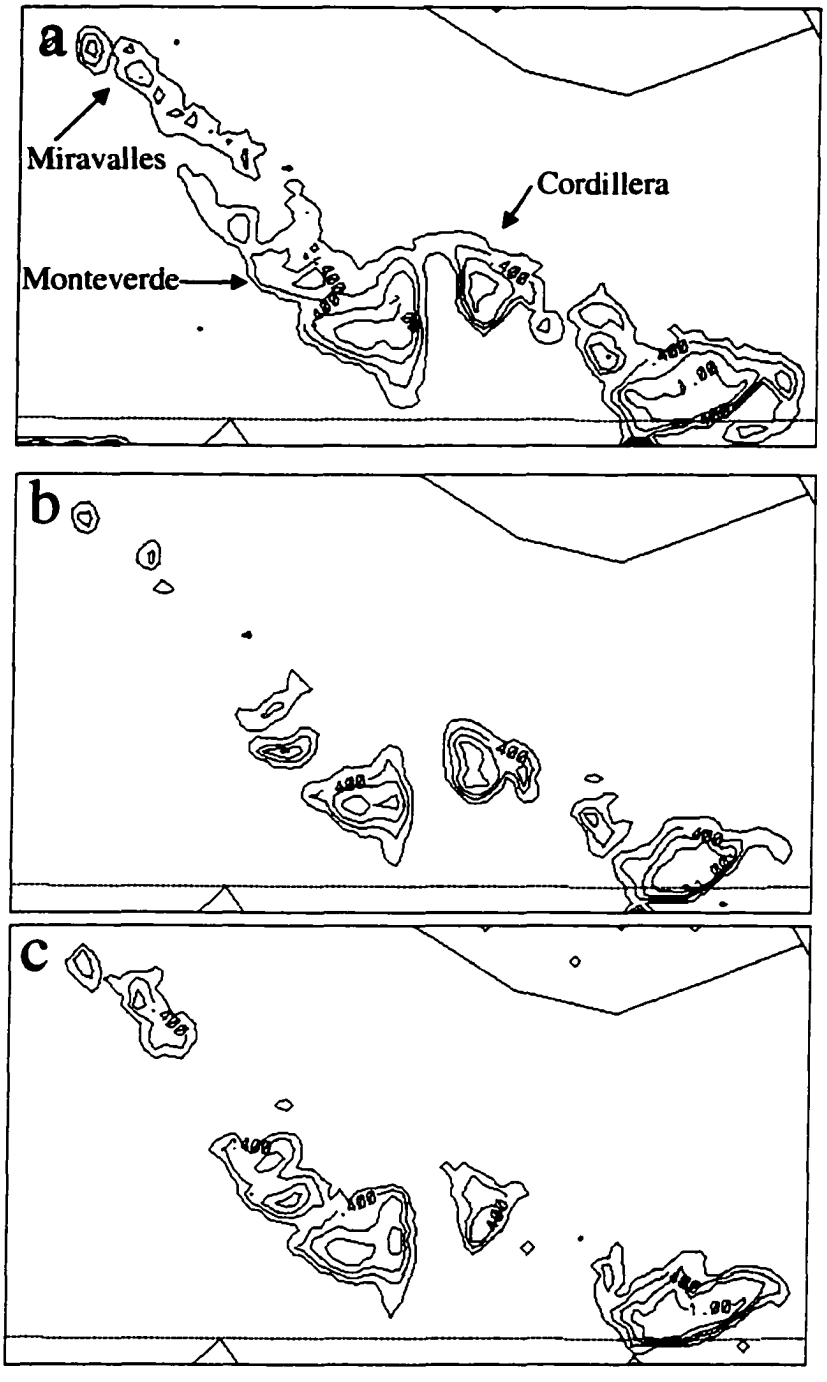

Figure 4.8: The distribution of cloud liquid water for 19 March 1999 at 1600 UTC for a) forested; b) deforested; and c) partially deforested simulations. Contour intervals are 0.3 g kg^{-1}, and the lowest contour level is 0.1g kg^{-1}.

Figure 4.1 for the various deforestation scenarios. The plots are for 19 March 1999, at 1600 UTC. Comparison with Figure 4.1 shows that the contours of liquid water content roughly follow the patterns of the local topography, with liquid water content increasing with increasing elevation. Notice that for the forested case (Figure 4.8a), ground level clouds cover a larger area and reach lower elevations in the Monteverde, Mirvalles and Cordillera Central regions than in the complete (Figure 4.8b) and partial deforestation simulations (Figure 4.8c). In the forested case, the surface orographic cloud cover is almost continuous along the mountain ranges in the region, whereas in the complete deforestation scenario, areas with orographic clouds at the surface are fragmented. Thus, it can be seen that an effect of deforestation is to shrink the areal coverage of the orographic clouds at the surface, as the edges of the cloud banks move further up the slopes of the mountains.

The vertical cross sections of liquid water content are contoured in Figure 4.9 in the east-west direction along the portion of the line XX contained within the dashed rectangle shown in Figure 4.1. At 1415 UTC, orographic clouds are present along Caribbean slopes of the Monteverde and Volcan Viejo regions for all the simulations (Figures 4.9a,d,g). The orographic clouds extend to the uppermost Pacific slopes of the Monteverde region for both forested and partial deforestation simulations (Figure 4.9a,g). However for the complete deforestation simulation, the cloud bank does not cross the crest of the range (Fig 4.9d). Orographic clouds are present on the lower western slopes of Volcan Viejo for the forested case, while for the other simulations clouds do not touch the surface at this location. For the forest simulations, the orographic clouds form at progressively lower elevations at 1515 and 1615 UTC (Figure 4.9b,c). At 1615 UTC the

cloud banks along the western slopes of the Volcan Viejo and eastern slopes of Monteverde almost touch each other (Figure 4.9c). Along the eastern slopes the orographic clouds are restricted to higher altitudes for both of the deforestation scenarios. However, for the partial deforestation scenario, the clouds touch the eastern slopes at a lower altitude than in the completely deforested scenario.

4.5.5 Modification of Air Masses from Lowland Deforestation

Lowland air masses are modified by deforestation. Surface energy fluxes, average temperatures and dewpoint temperatures of the surface air in the lowland regions (below an altitude of 600 m) are presented in Figures 4.10 and 4.11. In the partial deforestation scenario, land areas below 600 m are mostly deforested (Figure 4.2), all deforested for the complete deforestation scenario.

Notice that the average latent heat flux is largest for the forest simulation through most of the simulation time (Figure 4.10a). Further the average latent heat fluxes for the forest simulations peak earlier in the day, with a maximum of 225 W m^{-2} at 1700 UTC. In the deforestation simulations the maximum latent heat flux is approximately 190 W m^{-2} and occurs at about 1800 UTC. Consistent differences of about 30-40 W m^{-2} occur between the forested and deforested simulations.

The average latent heat fluxes for the partial deforestation scenario are only slightly larger (5 to 7 W m^{-2}) than that for the completely deforested simulations. This is expected since the forest cover for the lowland region is largely deforested.

The sensible heat fluxes (Figure 4.10b) generally are higher for the deforestation simulations, except between 1800 and 2000 UTC when they are higher for the forest

simulations, a reflection of midday water stress causing stomatal closure and a reduction in latent heat fluxes. The sensible heat fluxes for the deforestation simulations peak at approximately 1730 UTC, with a maximum value of about 38 W m^{-2}. The differences in sensible heat fluxes between the forested and deforested simulations are statistically significant through most of the simulation period, and average about 15 W m^{-2}. The partial and complete deforestation simulations show differences in sensible heat fluxes of about 5 W m^{-2}, with complete deforestation simulations showing higher values of sensible heat fluxes, especially during mid morning hours.

The diurnal variations of average surface temperature and dewpoint are examined in Figures 4.11a and 4.11b respectively. The deforested simulations have higher surface temperatures through most of the simulations except between 1930 and 2130 UTC, at which times the temperatures for all the simulations are very close to each other. Differences in surface air temperatures are statistically significant through most of the duration of the simulation, with differences averaging about 0.8^0C. There are insignificant differences in surface temperatures between the complete and partial deforestation scenarios.

Both the simulated surface temperatures and sensible heat fluxes are probably lower than those that actually occur. For example the daily maximum of surface temperature (averaged for areas of elevation under 600 m) should be about 28^0C, although the simulations yield a daily maximum of about 25.5^0C. This is due to the same limitations in the NCEP data used in initialization and for driving the lateral boundary conditions that were noted in the discussion of cloud base heights. This should not however influence the relative differences between the forested, deforested, and partially deforested scenarios.

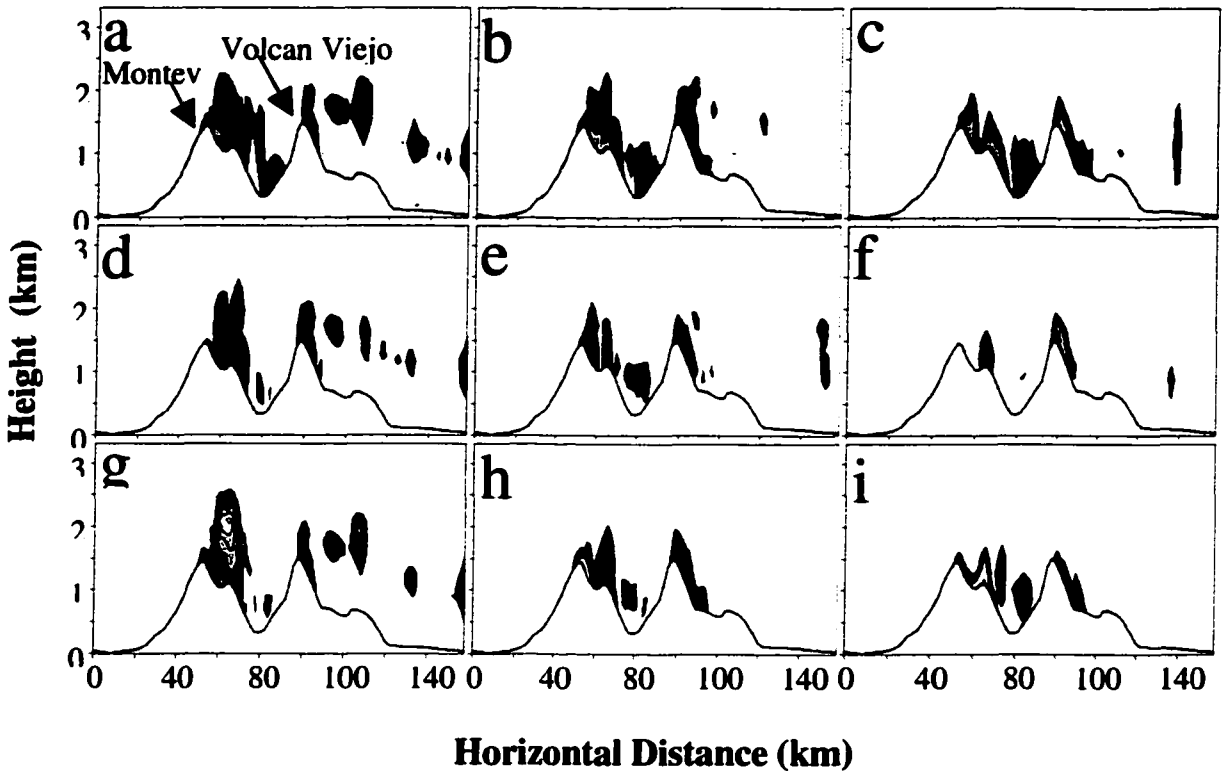

Figure 4.9: The vertical cross sections of cloud liquid water content for various scenarios on 19 March 1999. The cross sections at 1415 UTC, 1515 UTC, and 1615 UTC are shown in panels (a), (b), and (c) for forested; (d), (e), and (f) for deforested, and (g), (h), and (i) for partially deforested cases respectively.

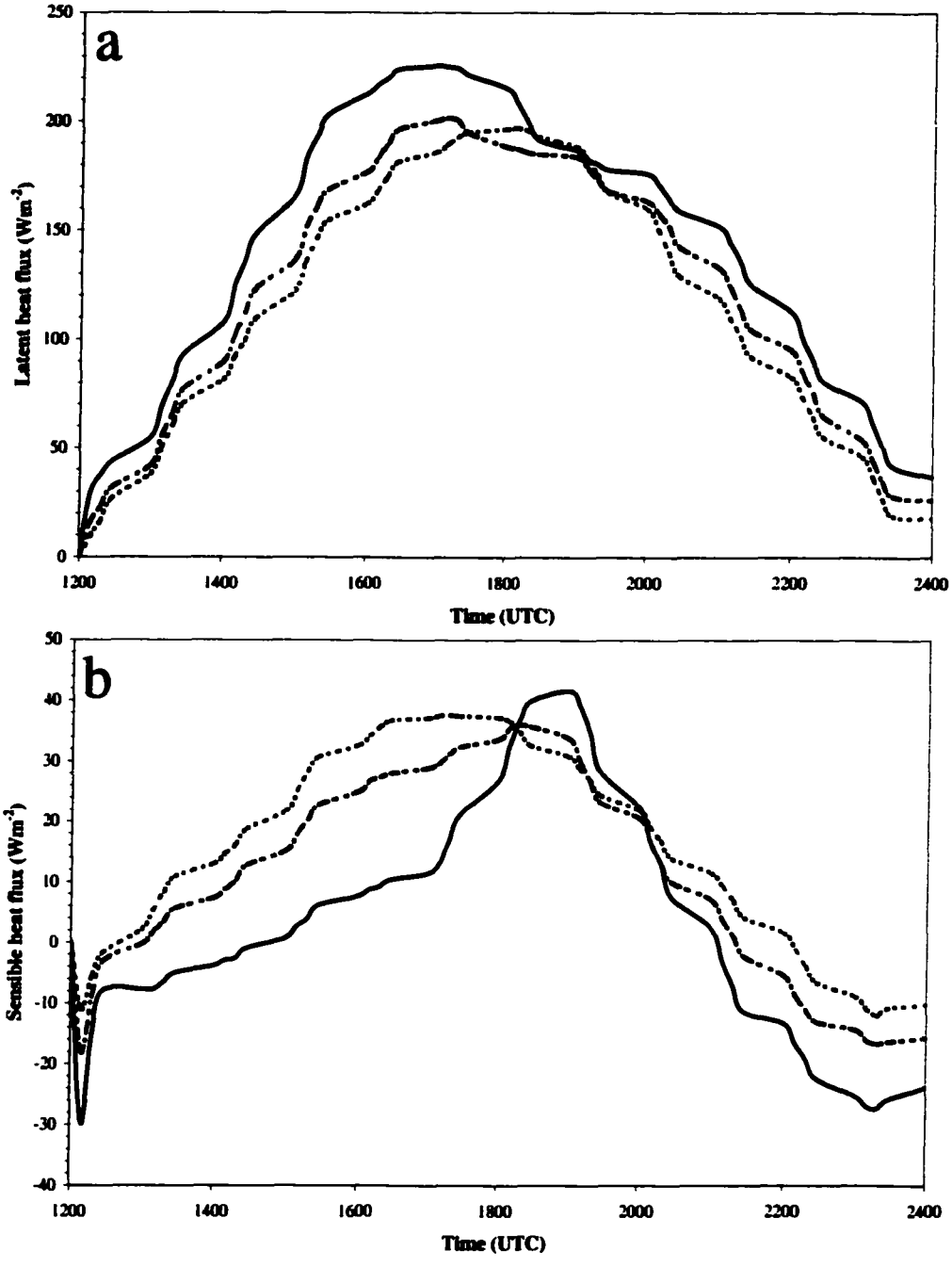

Figure 4.10: The average a) latent heat; b) sensible heat flux in the lowland regions for the forested (solid), complete deforestation (dotted) and partial deforestation (dot-dash) simulations.

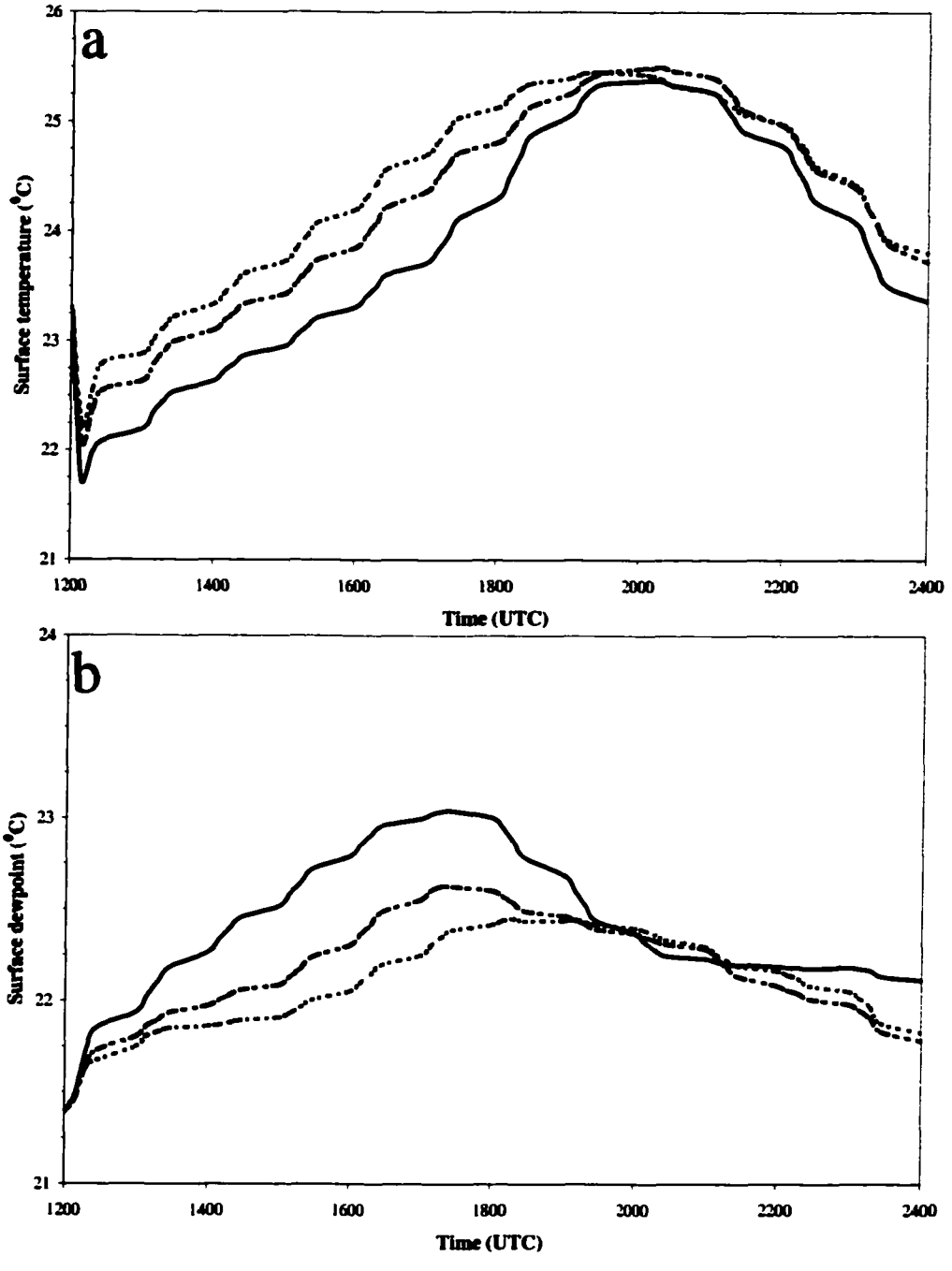

Figure 4.11: The average a) surface temperature; and b) surface dewpoint in the lowland regions for the forested (solid), complete deforestation (dotted), and partial deforestation (dot-dash) simulations.

The average surface dewpoint is larger for forest simulations compared to the deforested simulations, except between 1930 UTC and 2130 UTC. The average difference in dewpoint between the forested and deforested simulations is about 0.4^{0}C. Again, the differences in dewpoint temperatures between the partial and complete deforestation simulations are minimal.

Enhanced latent heat fluxes and diminished sensible heat fluxes over the forested lowlands result in the air over the forested lowlands being cooler and moister compared to deforested lowlands. The model results suggest lowland deforestation warms and dries the air, resulting in elevation of the cloud base height.

4.6 Conclusions

Recent studies show the possibility of localized climate change in the Monteverde cloud forest preserve in northwestern Costa Rica (Pounds et al., 1999; Still et al., 1999). The cloud forests, characterized by frequent immersion in orographic clouds, are very sensitive to moisture input from the clouds, especially during the dry season months. Processes that influence the distribution of orographic clouds have a significant impact on the hydrology of the cloud forest areas. Pounds et al. (1999) and Still et al. (1999) suggest that warming of the tropical oceans could be responsible for the recent observed changes in Monteverde region.

Vegetation is known to influence regional climate, especially boundary layer temperature, moisture and convection. This study explores the impacts of significant deforestation in the lowlands of Costa Rica on tropical montane cloud forests of the region. It is hypothesized that the lowland deforestation can modify the air masses over

the lowland regions, which are ultimately responsible for the formation of orographic clouds.

In this study the RAMS is used to simulate orographic clouds in the northern Costa Rican region for three land-use scenarios. In the first the entire land surface is forested, in the second the land surface is deforested, and in the third the recent estimate of forest cover by Wheelwright et al. (2000) is used. Orographic cloud patterns are simulated for six days in March of 1999. The model simulations for various land-use patterns are compared for differences in orographic cloud formation. The main conclusions from this study can be summarized as follows:

1) The RAMS model simulations show orographic cloud formation patterns similar to GOES satellite observations.
2) The orographic cloud base is shifted to higher elevations when the land surface is deforested. This shift in orographic cloud base occurs not only when all land surfaces are deforested but also when the lowland regions alone are deforested.
3) The upward shift of orographic cloud base height is in the order of 200 m for complete deforestation, and about 100 m for the partial deforestation case.
4) The region covered by ground-level cloud decreases when the land surface is deforested.
5) The effect of deforestation is to modify the lowland air masses to be drier and warmer. The warmer, drier air has to be lifted to higher elevations before it condenses to form clouds. This is the cause for the upward shift of the orographic cloud base height.

The effect of lowland deforestation in Costa Rica has two main effects, one to push the lower boundaries of orographic clouds to higher altitudes, and two to shrink the areas enveloped by the orographic cloud banks. The deforestation scenario complements the effects of increased sea surface temperature suggested by Pounds et al. (1999) and Still et al. (1999). The effect of increased sea surface temperature and deforestation on cloud forests may vary depending on their location. For example, the inland cloud forests, such as those in southern Mexico, may be significantly influenced by lowland deforestation, while for coastal forests such as the Luquillo forests of Puerto Rico the effects may be minimal. The results from this study suggest that, as the lowland regions become further deforested, mist free days could become more frequent in the Monteverde region. As deforestation shrinks the orographic cloud banks, driving orographic clouds further up the slopes of the mountains, the cloud forests will become more fragmented and susceptible. The potential ecological consequences warrants further research to enhance the realism of future modeling efforts.

Chapter 5

Summary

5.1 Summary and Conclusions

Tropical montane cloud forests rely on immersion within persistent and frequent orographic cloud cover for their existence. Thus factors which influence the location and likelihood of cloud formation in the air masses moving over tropical mountains have profound consequences for landscape conservation and management. The Monteverde cloud forests, the focus of considerable conservation and research interest, lie along the crest of the Cordillera de Tilarán, which rises abruptly from the lowlands of western Costa Rica to peaks over 1800 m.

In the Cordillera, anuran population crashes, an increase in the upper elevation of bird ranges on the Pacific slope, and longer mist-free intervals in the dry season at the lee edge of the Monteverde cloud forest have been attributed to an increase in the base height of the orographic cloud bank (Pounds et al., 1999). The frequency of long (>=5 day) mist-free periods in the dry season is related to Pacific sea surface temperatures, and thus El Niño events, but a trend remains after these are considered (Pounds et al., 1999). From a global climate model under 2 x CO_2 conditions, Still et al. (1999) suggest that sea surface warming results in intensification of tropical hydrological cycling, with release of latent heat upon condensation warming the atmosphere. From this Still et al. (1999) and Pounds et al. (1999) infer an increase in the lifting condensation level and the height of orographic cloud banks. Global climate models, however, have coarse spatial resolution

(~400 km horizontally, and several hundred meters vertically in that of Still et al. (1999)) and are incapable of resolving subgrid-scale features such as clouds, or terrain and land-use features known to have important influences on cloud formation.

In this study an alternate hypothesis is explored, namely that deforestation in the Costa Rican lowlands is responsible for the observed changes in the Monteverde cloud forest preserve. Deforestation is known to modify the properties of the boundary layer air, mainly warming and drying it. The Regional Atmospheric Modeling System (RAMS) and Geostationary Enviormental Operational Satellite (GOES) data is used to examine the effect of deforestation on cloud formation in the Costa Rican region.

The GOES satellite imagery show that late morning dry season cumulus is much less abundant over the long-deforested parts of Costa Rica's Rio San Juan basin than over the nearby forested region in Nicaragua. The less thoroughly deforested areas of Costa Rica near the river show intermediate degrees of cumulus development. Landsat images of dry season days with cumulus cloud field development in the region also show that cumulus clouds are commonly absent or poorly developed over deforested areas. The prominent zone of reduced cumulus cloudiness in the San Carlos area lies directly upwind of the Monteverde TMCF.

RAMS is used to examine differences in boundary layer cumulus cloudiness over forested as opposed to deforested surfaces. The RAMS simulations show differences in organization, cloud base height and cloud thickness between cloud fields over forested and deforested surfaces. The simulations suggest maximum differences of up to 600 m in average base heights of the boundary layer cumulus cloud fields, with the cloud base being higher for deforested surface conditions. The clouds are found be thicker on

average over the forested surfaces. The model simulations show considerable differences in surface energy fluxes between forest and deforestation simulations, namely enhanced sensible heat flux and diminished latent heat flux over deforested areas, resulting in the air over such regions being much warmer and drier.

RAMS is also used to investigate the effect of lowland deforestation on orographic cloud formation. The effect of three different scenarios of deforestation is explored. The land surface is completely forested for the first; the second assumes that the land surface is completely deforested; and in the third, the land surface is partially deforested where forest cover from recent estimates by Wheelwright et al. (2000) is used. For the same initial atmospheric condition, RAMS is used to simulate orographic cloud formations for the above described deforestation scenarios, and the differences are examined.

The effect of deforestation is to push the lower boundaries of the orographic clouds to higher altitudes. This increase in cloud base height is about 200 m when the surface is completely deforested and about 100 m when the surface is partially deforested. Lower cloud cover is observed for the deforested simulation, with the cloud cover decreasing in proportion to the amount of deforestation. Deforestation also shrinks area enveloped by the orographic cloud banks. The model simulations show that the modification of air masses by deforested areas, making them warmer and drier, is the cause for shift of the orographic cloud banks to higher elevations.

The scenario presented in this study complements that of Pounds et al. (1999) and Still et al. (1999), broadening the "lifting cloud base hypothesis" for biotic changes in Central American mountains by providing an alternative mechanism – upwind deforestation of lowlands – which may increase convective and orographic cloud bases

even more than changes in sea surface temperature do. Cloud forests will vary in their sensitivity to upwind deforestation and sea surface temperature changes. Indeed, inland cloud forests such as those of southern Mexico may be profoundly influenced by regional deforestation. On the other hand, coastal forests like those of some Caribbean islands (e.g., the Luquillo forest of Puerto Rico) may have too little upwind lowland areas to experience deforestation impacts like those we discuss. Nonetheless, these results suggest that current trends in tropical land use will force cloud forests upward, and they will thus decrease in area and become increasingly fragmented – and in many low mountains may disappear altogether.

5.2 Future Work

This study examined the effect of deforestation on the formation of cumulus and orographic clouds in the Costa Rican region, using idealized models. However there is a significant lack of information about the meteorology over forested and deforested sites in this area. Also lacking is information about the soil variables at the forested and deforested areas. Measurements of surface energy budget need to be made over areas of different land use. Using remote sensing techniques like that of Gillies et al. (1992) on high spatial resolution satellite data such as ASTER, surface energy budgets of areas of varied land use may be retrieved. However, high cloud cover over forested areas is a problem when using this technique. Also in-situ measurements of the surface energy budget are needed, at least for a few sites, to verify the accuracy of such techniques.

There is also a need to better understand the hydrology of the cloud forests in this area. For these measurements of surface air properties as they are lifted up the slopes of Cordillera de Tilarán, cloud base height etc., are needed. Such information could be used

for testing and calibrating the mesoscale models which can be then used to generate a better understanding of the cloud forest hydrology and processes that may influence it. Such models could also provide information on geographical distribution of orographic clouds, especially the amount of cloud liquid water input at various altitudes. This would provide ecologists valuable insight into understating the distribution of flora and fauna within the cloud forest.

Bibliography

Anthes, R.A., 1984: Enhancement of convective precipitation by mesoscale variations in vegetative covering in semiarid regions. *J. Climate Appl. Meteor.*, **23**, 541-554.

Avissar R., and R.A. Peilke, 1989: A parameterization of heterogeneous land surfaces for atmospheric models and its impact on regional meteorology. *Mon Wea. Rev.*, **117**, 2113-2136.

Avissar R., and Y. Liu, 1996: Three-dimensional numerical study of shallow convective clouds and precipitation induced by land surface forcing. *J. Geophys. Res.*, **101**, 7499-7518.

Avissar, R., and T. Schmidt, 1998: An evaluation of scale at which ground-surface heat flux patchiness affects the convective boundary layer using large-eddy simulations. *J. Atmos. Sci.*, **55**, 2666-2689.

Bastable, H.G., W.J. Shuttleworth, R.L.G. Dallarosa, G. Fisch, and C.A. Nobre, 1993: Observations of climate, albedo and surface radiation over cleared and undisturbed Amazonian forest. *Intl. J. Climatol.*, **13**, 783-796.

Berendes, T., S.K. Sengupta, R.M. Welch, B.A. Wielicki, and M. Navar, 1992: Cumulus cloud base height estimation from high spatial resolution Landsat data: A Hough transform approach. *IEEE Trans. Geosci. and Remote Sensing*, **30, No. 3**, 430-443.

Brooks, C.E.P., 1928: The influence of forests on rainfall and run-off. *Quart. J. Roy. Meteor. Soc.*, **54**, 1-17.

Bruijnzeel, L.A., and J. Proctor, 1993: Hydrology and biogeochemistry of tropical montane cloud forests: What do we really know?. In: *Tropical montane cloud forests*, L. S. Hamilton, J.O. Juvik, and F.N. Scatena, Eds., East-West Center, Honolulu, 21-46.

Bruinjzeel, L.A., and J. Proctor, 1995: *Tropical montane cloud forests.* L. S. Hamilton, J.O. Juvik, and F.N. Scatena, Eds., Springer-Verlag, 38-78.

Bryant, N.A., L.F. Johnson, A.J. Brazel, R.C. Balling, C.F. Hutchinson, and L.R. Beck. 1990: Measuring the effect of overgrazing in the Sonoran Desert. *Climatic Change*, **17**, 243-264.

Chen F., and R. Avissar, 1994: Impact of land-surface moisture variability on local shallow convective cumulus and precipitation in large-scale models. *J. Appl. Meteor.*, **33**, 1382-1394.

Chen, C., and W.R. Cotton, 1983: A one-dimensional simulation of the stratocumulus-capped mixed layer. *Bound.-Layer Meteor.*, **25**, 289-321.

Chou, J., R. C. Weger, J. M. Ligtenberg, P. Breeden, K.-S. Kuo, and R.M. Welch, 1994: Segmentation of polar scenes using multispectral texture measures and morphological filtering. *Intl. J. Remote Sensing*, **15, No. 5**, 1019-1036.

Chu A., C. M. Sehgal, and J. F. Greenleaf, 1990: Use of gray value distribution of run lengths for texture analysis. *Pattern Recognition Letters*, **11**, 415-420.

Clark, K.L., R.O. Lawton, and P.R. Butler, 2000: *Monteverde: ecology and conservation of a tropical cloud forest.* N.M. Nadkarni and N.T. Wheelwright, Eds., Oxford University Press, New York, N.Y., 15-38.

Cutrim, E.D., W. Martin, and R. Rabin, 1995: Enhancement of cumulus clouds over deforested lands in Amazonia. *Bull. Amer. Meteor. Soc.*, **76**, 1801-1805.

Dietrich, W. E., D.M Windsor, and T. Dunne, 1982: *The Ecology of a Tropical Forest.* E.G. Leigh, A.S. Rand, and D.M. Windsor, Eds, Smithsonian Institution Press, Washington, D.C., 21-46.

Doumenge C., D. Gilmour, M.R. Perez, J. and Blockhus, 1993: Tropical montane cloud forests: Conservation status and management issues. In: *Tropical montane cloud*

forests, L.S. Hamilton, J.O. Juvik and F.N. Scatena, Eds., East-West Center, Honolulu, 21-46.

Duda, R.O., and P.E. Hart, 1973: *Pattern Classification and Scene Analysis*, Wiley-Interscience.

Emori, S., 1998: Interaction of cumulus convection with soil moisture distribution: An idealized simulation. *J. Geophys. Res.*, **103**, 8873-8884.

Galloway, M.M., 1975: Texture analysis using gray level run lengths. *Computer Graphics and Image Processing*, **4**, 172-179.

Gash, J.H.C., and C.A. Nobre, 1997: Climatic effect of Amazonian deforestation: Some results from ABRACOS. *Bull. Amer. Meteor. Soc.*, **78**, 823-830.

Gibson, H.M., and T.H. Vonder Haar, 1990: Cloud and convection frequencies over the southeast United States as related to small-scale geographic features. *Mon. Wea. Rev.*, **118**, 2215-2227.

Golaz, J.-C., H. Jiang, and W.R. Cotton, 2001: A large-eddy simulation study of cumulus clouds over land and sensitivity to soil moisture. Submitted for publication to Atmospheric Research.

Hamilton, L.S., J.O. Juvik, and F. N. Scatena, 1993: The Puerto Rico tropical cloud forest symposium: Introduction and workshop synthesis. In: *Tropical montane cloud forests*, L. S. Hamilton, J.O. Juvik, and F.N. Scatena, Eds., East-West Center, Honolulu,1-16.

Hinke, T.H., J. Rushing, H. Ranganath, and S.J. Graves, 2001: Using Association Rules as texture features. *IEEE Transactions on Pattern Analysis and Machine Intelligence*, **23**, 845-858.

Kalnay, E., M. Kanamitsu, R. Kistler, W. Collins, D. Deaven, L. Handin, M. Iredell, S. Saha, G. White, J. Woollen,Y. Zhu, M. Chelliah, W. Ebisuzaki, W. Higgins, J. Janowiak, K. C. Mo, C. Ropelewski, J. Wang, A. Leetmaa, R. Reynolds, R. Jenne, and D. Joseph, 1996: The NCEP / NCAR 40-year Reanalysis Project. *Bull. Amer. Meteor. Soc.*, **77**, 437-471.

Kuo, K.S., R.M. Welch, and R.C. Weger, 1993: The three-dimensional structure of cumulus clouds over the ocean.1. Structural analysis. *J. Geophys. Res.*, **98**, 20685-20711.

Lawton R.O, U.S. Nair, R.A. Pielke, and R.M. Welch, 2001: Climatic impact of tropical lowland deforestation on nearby montane cloud forests. *Science*, **294**, 584-587.

Long, Adrian J., 1994: The importance of tropical montane cloud forests for endemic and threatened birds. In: *Tropical montane cloud forests*, L.S. Hamilton, J.O. Juvik, and F.N. Scatena, Eds., East-West Center, Honolulu.

Levine, M.D., and S.I. Shaheen, 1978: A modular computer vision system for picture segmentation and interpretation. *I.E.E E. Transactions On Pattern Analysis and Machine Intelligence*, PAMI-3, 540-556.

Lyons, T.J., P. Schwerdtfeger, J.M. Hacker, I.J. Foster, R.C.G. Smith, and H. Xinmei, 1993: Land-atmosphere interaction in a semiarid region: The bunny fence experiment. *Bull. Amer. Meteor. Soc.*, **74**, 1327-1334.

Mahrer, Y., and R.A. Pielke, 1975: A numerical study of air flow over mountains using the two-dimensional version of the University of Virginia mesoscale model. *J. Atmos. Sci.*, **32**, 2144-2155.

Meher-Homji, V.M., 1991: Probable impact of deforestation on hydrological processes. *Climate Change*, **19**, 163-173.

Myers, N., R.A. Mittermier, C.G. Mittermier, G.A.B. da Fonesca, and J. Kent, 2000: Biodiversity hotspots for conservation priorities. *Nature*, **403**, 85-858.

Nair U.S., J.A. Rushing, R. Ramachandran, K.S. Kuo, R.M. Welch and S.J. Graves, 1999: Detection of cumulus cloud fields in satellite imagery. In: *Earth Observing Systems IV*, William L. Barnes, Ed., Proceedings of SPIE, **3750**, 345-355.

Nair, U.S., R.M. Welch, R.O. Lawton and R.A. Pielke Sr., 2000: Impact of land use on Costa Rican regional climate. *Proc. IEEE IGARSS 2000*, V, 1993-1995.

Nair, U.S., J.A. Rushing, R. Ramachandran, K.S. Kuo, R.M. Welch, and S.J. Graves, 2002a: Detection of cumulus cloud fields in GOES satellite imagery. Submitted for publication.

Nair, U.S., R.O. Lawton, R.M. Welch, and R.A. Pielke Sr., 2002b: Impact of land use on tropical montane cloud forests: 1. Sensitivity of cumulus cloud field characteristics to lowland deforestation. Submitted for publication.

Ookouchi, Y., M. Segal, R.C. Kessler, and R.A. Pielke, 1984: Evaluation of soil moisture effects on generation and modification of mesoscale circulations. *Mon. Wea. Rev.*, **112**, 2281-2292.

Otterman, J., 1974: Baring high-albedo soils by overgrazing: A hypothesized desertification mechanism. *Science*, **86**, 531-533.

Otterman, J., 1981: Satellite and field studies of man's impact on the surface in arid regions. *Tellus*, **33**, 68-77.

Otterman, J., A. Manes, S. Rubin, P. Alpert, and D. O'C. Starr, 1990: An increase of early rains in southern Israel following land-use change?. *Bound.-Layer Meteor.*, **53**, 333-351.

Pankiewicz, G.S., 1995: Pattern recognition techniques for the identification of cloud and cloud systems. *Meteor. Appl.*, **2**, 257-271.

Pounds, A.J., M.P.L. Fogden, and J.H. Campbell, 1999: Biological response to climate change on tropical mountain. *Nature*, **389**, 611-614.

Pielke, R.A., 1974: A three-dimensional numerical model of the sea breezes over south Florida. *Mon. Wea. Rev.*, **102**, 115-139.

Pielke, R.A., and X. Zeng, 1989: Influence of severe storm development of irrigated land. *Natl. Wea. Dig.*, **14**, 16-17.

Pielke, R.A, W.R. Cotton, R.L. Walko, C.J. Tremback, W.A. Lyons, L.D. Grasso, M.E. Nicholls, M.D. Moran, D.A. Wesley, T.J. Lee, and J.H. Copeland, 1992: A comprehensive meteorological modeling system - RAMS. *Meteor. Atmos. Phys.*, **49**, 69-91.

Pielke, R.A. Sr., R.L. Walko, L.T. Steyaert, P.L. Vidale, G.E. Liston, W.A. Lyons and T.N. Chase, 1998: The influence of anthropogenic landscape changes on weather in south Florida. *Mon. Wea. Rev.*, **127**, 1663-1673.

Pielke, R.A. Sr., 2001: Influence of the spatial distribution of vegetation and soils on the prediction of cumulus convective rainfall. *Rev. Geophys.*, 39, 151-178.

Rabin, R.M., S. Stadler, P.J. Wetzel, D.J. Stensrud, and M. Gregory, 1990: Observed effect of landscape variability on convective clouds. *Bull. Amer. Meteor. Soc.*, **71**, 272-280.

Rabin, R.M., and D.W. Martin, 1996: Satellite observations of shallow cumulus coverage over the central United States: An exploration of landuse impact on cloud cover. *J. Geophys. Res.*, **101**, 7149-7155.

Ray, D.K., U.S. Nair, R.M. Welch, Q. Han, J. Zeng, and W. Su., 2002: Effects of land use in southwest Australia: Part 1. Observations of cumulus cloudiness and energy fluxes. Submitted for publication.

Sader, S.A., and A.T. Joyce, 1988: Deforestation rates and trends in Costa Rica, 1940 to 1983. *Biotropica*, **20**,11-19.

Sagan, C., O.B. Toon, and J.B. Pollack, 1979: Anthropogenic albedo changes on the Earth's climate. *Science*, **206**, 1363-1368.

Segal, M., R. Avissar, M.C. McCumber, and R.A. Pielke, 1988: Evaluation of vegetation effects on the generation and modification of mesoscale circulations. *J. Atmos. Sci.*, **45**, 2268-2292.

Segal, M., W. Schreiber, G. Kallos. R.A. Pielke, J.R. Garratt, J. Weaver, A. Rodi and J. Wilson, 1989: The impact of crop areas in northeast Colorado on midsummer mesoscale thermal circulations. *Mon. Wea. Rev.*, **117**, 809-825.

Segal, M., R.W. Arritt, J. Shen, C. Anderson, and M. Leuthold, 1997: On the clearing of cumulus clouds downwind from the lakes. *Mon. Wea Rev.*, **125**, 639-646.

Schickedanz, P.T., 1976: The effect of irrigation on precipitation in the Great Plains. NSF-RANN, Grant GI-43871, Final Rep., Atmospheric Science Section, Illinois State Water Survey, Urbana, 105 pp.

Shukla, J., and Y. Mintz, 1982: Influence of land-surface evapotranspiration on the Earth's climate. *Science*, **215**, 1498-1501.

Schwartz, M.D., and T. R. Karl, 1990: Spring phenology: Nature's experiment to detect the effect of "green-up" on surface maximum temperatures. *Mon. Wea. Rev.*, **114**, 883-890.

Still, C.J., P.N. Foster, and S.H. Schneider, 1999: Simulating the effects of climate change on tropical montane cloud forests. *Nature*, **389**, 608-610.

Sud, Y.C., W.C. Chao, and G.K. Walker, 1993: Dependence of rainfall on vegetation: Theoretical considerations, simulation experiments, observations, and inferences from simulated atmospheric soundings. *J. Arid Environments*, **25**, 5-18.

Sykes, R.I., and D.S. Henn, 1989: Large-eddy simulation of turbulent sheared convection. *J. Atmos. Sci.*, **35**, 25-39.

Tremback, C.J., and R. Kessler, 1985: A surface temperature and moisture parameterization for use in mesoscale numerical models, *Proc., 7th AMS Conference on Numerical Weather Prediction*. June 17-20. Montreal, Quebec, Canada, *Amer. Meteor. Soc.*, Boston. 355-358.

Vaughan, C., 1983: A report on dense forest habitat for endangered species in Costa Rica., Universidad Nacional, Heredia, Costa Rica, 1983.

Veldkamp, E., A.M. Weitz, I.G. Staritsky, and E.J. Huising, 1992: Deforestation trends in Atlantic zone of Costa Rica: A case study. *Land Degrad. Rehab.*, **3**, 71-84.

Weckweth, T.M., J.W. Wilson, R.M. Wakimoto, and N.A. Crook, 1997: Horizontal convective rolls: Determining the environmental conditions supporting their existence and characteristics. *Mon. Wea. Rev.*, **125**, 505-526.

Wetzel, P.J., S. Argentini, and A. Boone, 1996: Role of land surface in controlling daytime cloud amount: Two case studies in GCIP-SW area. *J. Geophys. Res.*, **101**, 7359-7370.

Wheelwright, N.T., 2000: Conservation biology. Chapter 12 in *Monteverde: Ecology and conservation of a tropical cloud forest*, N.M. Nadkarni and N.T. Wheelwright, Eds., Oxford University Press, New York, N.Y., 419-456.

Wielicki, B.A., and R.M. Welch, 1986: Cumulus cloud properties derived using Landsat satellite data. *J. Climate Appl. Meteor.*, **25**, 261-276.